

This volume is the property of the University of Oklahoma, but the literary rights of the author are a separate property and must be respected. Passages must not be copied or closely paraphrased without the previous written consent of the author. If the reader obtains any assistance from this volume, he or she must give proper credit in his own work.

I grant the University of Oklahoma Libraries permission to make a copy of my thesis/dissertation upon the request of individuals or libraries. This permission is granted with the understanding that a copy will be provided for research purposes only, and that requestors will be informed of these restrictions.

NAME _____

DATE May 5th, 2014

A library which borrows this thesis/dissertation for use by its patrons is expected to secure the signature of each user.

This thesis/dissertation by LILY SPRINGMAN PFEIFER has been used by the following persons, whose signatures attest their acceptance of the above restrictions.

NAME AND ADDRESS _____ DATE _____

UNIVERSITY OF OKLAHOMA

GRADUATE COLLEGE

RAPID PERMIAN EXHUMATION OF THE MONTAGNE NOIRE DOME
RECORDED IN PROVENANCE OF UPPER PALEOZOIC CLASTICS IN THE
GRAISSESSAC-LODÈVE BASIN, FRANCE

A THESIS

SUBMITTED TO THE GRADUATE FACULTY

in partial fulfillment of the requirements for the

Degree of

MASTER OF SCIENCE

By

LILY SPRINGMAN PFEIFER

Norman, Oklahoma

2014

SIS
E
P.3

RAPID PERMIAN EXHUMATION OF THE MONTAGNE NOIRE DOME
RECORDED IN PROVENANCE OF UPPER PALEOZOIC CLASTICS IN THE
GRAISSESSAC-LODÈVE BASIN, FRANCE

A THESIS APPROVED FOR THE
CONOCOPHILLIPS SCHOOL OF GEOLOGY AND GEOPHYSICS

BY

[REDACTED]

Dr. Gerylyn S. Soreghan, Chair

[REDACTED]

Dr. Michael J. Soreghan

[REDACTED]

Dr. Stéphane Pochat

Acknowledgements

This research was supported by the National Science Foundation (grants OISE-1132797 and EAR-1053018). A special thank you goes to my adviser, Dr. Lynn Screehon, who has been a constant source of support and guidance. I have greatly enjoyed working on this project with you, and learning from you along the way! Thank you to Dr. Stéphane Pochat, Dr. Jean Van Den Driessche, and Tyler Foster for their assistance during our shared adventures in this (not too shabby) field area of southern France. Jess and Stéphane, thanks for always promptly getting back to me during the writing process with all of my questions! Thank you to Dr. George Gebrels, Mark Pecha, and the University of Arizona LaserCham Center (supported by NSF-EAR-1032156), as well as Molly Swift for help with digital vision analyses. I would also like to express my gratitude to Dr. Mike Soreghan for assistance with this research, Dr. George Morgan for microprobe and labwork assistance, Jody Foote for library help, Dr. Jesse Wilkinson for support with statistical analysis tools, and Kirsteen Sefton for help with other labwork. I would like to thank the University of Oklahoma for supporting me financially, and allowing me to participate in this research, as well as to help with travel costs associated with attending and presenting at conferences. A final acknowledgement goes to my friends (within the department, and otherwise) and to my family, who constantly support me through all of my endeavors and tedious "rock talk." Writing this thesis has truly been an invaluable experience in my growth as a geoscientist, and I very much enjoyed the preceding field work in France, to defending here at OU. Once again, I greatly appreciate the generous time, advice, patience, and support you all have dedicated to helping me out.

© Copyright by LILY S. PFEIFER 2014
All Rights Reserved.

Acknowledgements

This research was supported by the National Science Foundation (grants OISE-1132792 and EAR-1053018). A special thank you goes to my adviser, Dr. Lynn Soreghan, who has been a constant source of support and guidance. I have greatly enjoyed working on this project with you, and learning from you along the way! Thank you to Dr. Stéphane Pochat, Dr. Jean Van Den Driessche, and Tyler Foster for their assistance during our shared adventure in the (not too shabby) field area of southern France. Jean and Stéphane, thanks for always promptly getting back to me during the writing process with all of my questions! Thank you to Dr. George Gehrels, Mark Pecha, and the University of Arizona LaserChron Center (supported by NSF-EAR 1032156), as well as Molly Swift for help with detrital zircon analyses. I would also like to express my gratitude to Dr. Mike Soreghan for assistance with this research, Dr. George Morgan for microprobe and labwork assistance, Jody Foote for library help, Dr. Bruce Wilkinson for support with statistical analysis tools, and Kirellos Sefein for help with other labwork. I would like to thank the University of Oklahoma for supporting me financially, and allowing me to participate in this research, as well as to help with travel costs associated with attending and presenting at conferences. A final acknowledgement goes to my friends (within the department, and otherwise) and to my family, who constantly support me through all of my endeavors and tedious “rock talk.” Writing this thesis has truly been an invaluable experience in my growth as a geoscientist, and I very much enjoyed the process; from field work in France, to defending here at OU. Once again, I greatly appreciate the generous time, advice, patience, and support you all have dedicated to helping me out for the past two years. Merci beaucoup!

Table of Contents

Acknowledgements	iv
Table of Contents	v
List of Tables	vii
List of Figures.....	viii
Abstract.....	x
Chapter 1: Introduction.....	1
Regional Geologic Setting.....	2
Chapter 2: Graissessac-Lodève Basin Stratigraphy	5
Croix de Mounis Formation (Upper Carboniferous).....	5
Pabau and Houillère Formations (Upper Carboniferous).....	6
Usclas Formation (Lower Permian)	6
Loiras and Viala Formations (Lower Permian).....	6
Rabejac Formation (Lower to Middle Permian)	7
Salagou Formation (Middle to Upper Permian).....	8
Chapter 3: Methods	9
Sampling.....	9
Detrital Zircon Geochronology	9
Sandstone Petrography	12
Subsidence Analysis.....	13
Chapter 4: Provenance Results.....	14
Croix de Mounis Formation (XDM)	14
Pabau and Houillère Formations (PAB and HOU)	15
Usclas Formation (USCL).....	16
Loiras Formation (LRS)	16
Rabejac Formation (RAB).....	17
Salagou Formation (SAL)	17

Basin Subsidence.....	18
Chapter 5: Discussion.....	20
Vertical Trends	20
Detrital Zircon Geochronology	20
Framework Mineralogy	22
Potential Sources for Detrital Zircon Grains	23
Archean-Precambrian Ages (3000-1000 Ma)	23
Neoproterozoic Ages (1000-555 Ma).....	24
Cambro-Ordovician Ages (552-445 Ma)	25
Middle Silurian-Middle Devonian Ages (430-394 Ma).....	26
Late Devonian-Early Carboniferous Ages (378-331 Ma)	26
Middle Carboniferous-Early Permian Ages (330-285 Ma).....	27
Provenance and Tectonic Implications.....	28
Early Permian Exhumation of the Montagne Noire Dome	31
Chapter 6: Conclusions.....	36
References Cited.....	38
Appendix A: Figures	50
Appendix B: Tables.....	80
Appendix C: Detrital Zircon Ages (Raw Data).....	84
Appendix D: Point Count Totals (Raw Data).....	102
Appendix E: Supplementary Figures and Tables	105

List of Tables

Table 1: Detrital modes of Lodève Basin sandstones: QFL totals and percentages by formation	81
Table 2: Summary of detrital ages and percentages for all samples, separated into groups by age.....	82
Table 3: All results from Kolmogorov-Smirnoff, Overlap-Similarity, and Likeness statistical tests by sample pair comparisons	83
Figure 1: Geological map of the Lodève Basin	84
Figure 2: Structural map of the Lodève Basin	85
Figure 3: Sample location map (Lodève and Bédoulet regions)	86
Figure 4: BSE images of zircons in all detrital samples analyzed	87
Figure 5: U/Pb vs. Pb ²⁰⁶ /Pb ²⁰⁸ age plot for all analyzed zircons	88
Figure 6: Relative age probability plots and cumulative diagrams	89
Figure 7: Light microscope images of thin sections used for zircon analysis	90
Figure 8: Ternary plots (QFL, Qz/Fz) of framework siliciclastic for all samples	91
Figure 9: Ternary plots (QFL, Qz/Fz) of framework siliciclastic for all samples	92
Figure 10: Normalized probability distribution of all detrital zircon samples	93
Figure 11: Framework mineralogy ternary plots with inferred detrital settings	94
Figure 12: Source Map—Montagne Noire region (southern Massif Central)	95

List of Figures

Figure 1: Structural map of Massif Central in context of the European Variscides.....	51
Figure 2: Structural map of the Massif Central and Lodève Basin cross section.....	52
Figure 3: Paleogeographic reconstructions of W. Europe through Late Paleozoic.....	53
Figure 4: Geological profile of southern Massif Central (Montagne Noire).....	57
Figure 5: Stratigraphic column of the Permo-Carboniferous strata in the Graissessac- Lodève Basin	59
Figure 6: Photos of representative rock types from each formation	60
Figure 7: Sample location map (Lodève and Bédarieux regions)	62
Figure 8: BSE images of zircon in all detrital samples analyzed	63
Figure 9: U/Th vs. Pb^{206}/U^{238} age plot for all analyzed zircons	64
Figure 10: Relative age probability plots and concordia diagrams	65
Figure 11: Light microscope images of thin sections used for modal analyses	67
Figure 12: Ternary plots (QFL, QmFLt) of framework mineralogy for all samples	69
Figure 13: Tectonic subsidence plot.....	70
Figure 14: Normalized probability distribution of all detrital zircon samples	71
Figure 15: Framework mineralogy ternary plots with inferred tectonic setting.....	73
Figure 16: Source Map— Montagne Noire region (southern Massif Central)	74

Figure 17: Source Map— French Massif Central	76
Figure 18: Source Map— Variscan belt of Western Europe in the Permian	77
Figure 19: Summary of provenance through the Late Paleozoic in southern Massif Central	78

Abstract

The Graissessac-Lodève Basin (southern France) preserves a thick and exceptionally complete record of continental sedimentation spanning Late Carboniferous through Late Permian time. This section records the localized tectonic and paleogeographic evolution of southern France, in the context of the low-latitude Variscan Belt of Western Europe. This study presents new detrital zircon and framework mineralogy data that address the provenance of Upper Carboniferous-Upper Permian siliciclastic strata exposed in the Graissessac-Lodève Basin. Detrital zircons in eight samples yielded significant populations that correspond with the ages of regional tectonic events, including: 500-445 Ma (widespread granitic magmatism and volcanism caused by rifting and back-arc extension along the northern Gondwanan margin), 378-331 Ma (high pressure-low temperature metamorphism and deformation during fore-arc compression, and Variscan arc-continent collision), and 330-285 Ma (magmatism, volcanism, and migmatization, chiefly in the southern Massif Central, related to post-orogenic extension of the Variscan belt). The ages and compositions of units that constitute the Montagne Noire metamorphic core complex (proximal to the west of the Graissessac-Lodève Basin) dictate detrital zircon age populations and sandstone framework mineralogy in Permian formations. Cambrian-Archean detrital zircon populations, and metamorphic lithic-rich sandstone framework compositions are derived from recycled detritus of the Neoproterozoic-Early Cambrian metasedimentary Schistes X, which formerly covered the Montagne Noire dome. Ordovician ages and subarkosic framework modes result from erosion of orthogneiss units (deformed granitoid intrusions in the lower Schistes X) that form an “envelope” on the flanks of

the dome. In the lower-middle Permian units, the youngest zircon population 330-285 Ma, together with feldspar-rich compositions, reflect derivation from Late Carboniferous-Early Permian granite units in the axial zone of the Montagne Noire. Hence, these data record exhumation, and progressive unroofing of the Montagne Noire dome. The timing of core complex exhumation was previously assumed to have occurred in the Pliocene-Miocene. Our results include 330-285 Ma zircon populations, linked to sandstone compositions of polycrystalline quartz, feldspar, and metamorphic lithic fragments, which persist through the Permian section of the Lodève Basin (Loiras-Salagou formations). Using estimates of maximum depositional ages, this requires uplift and unroofing of the Montagne Noire core (source terrane) by ca. 295 Ma. The most recent migmatization, magmatism, and deformation occurred at 298 ± 2 Ma, at ~ 17 km depth (based on peak metamorphic conditions in the gneissic core). Accordingly, these new provenance data demonstrate that cooling and exhumation of the core was rapid (3.4-17 mm/year, within error), and early (300-295 Ma), reflecting local paleogeographic uplift in the southern Massif Central during post-orogenic extension. Subsidence analysis of the Graissessac-Lodève Basin includes rapid initial subsidence (≥ 312 m/My), characteristic of extensional rift basins during formation, followed by subsidence (70 m/My) that persists throughout the Permian, and is interpreted as the crustal response to the hypothesized progressive exhumation and unroofing of the Montagne Noire core complex during the Early Permian.

Chapter 1: Introduction

The Variscan Massif Central region of France (Fig. 1) preserves evidence of an exceptionally complex tectonic evolution involving Late Paleozoic rifting, convergence and collision, horizontal thrusting, and subsequent post collisional extension, basin formation, and magmatism (Menard and Molnar, 1988; Van Den Driessche and Brun, 1989; Malavieille, 1993; Burg et al., 1994; Becq-Giraudon and Van Den Driessche, 1994). Upper Carboniferous-Permian strata in the Graissessac-Lodève Basin (Fig. 2), southern Variscan Massif Central, provide one of the thickest and most complete records of Upper Paleozoic strata in Europe (Odin, 1986; Korner et al., 2003; Pochat and Van Den Driessche, 2011).

This work assesses provenance signatures of Upper Carboniferous- Upper Permian strata exposed in the Graissessac-Lodève Basin by integrating detrital zircon geochronology, sandstone framework mineralogy, and subsidence analysis. The main objective of this research is to better understand the local tectonic and paleogeographic evolution of the southern Massif Central in context of the western European Variscan belt by reconstructing paleogeography and paleodispersal patterns. Upper Paleozoic strata of the Graissessac- Lodève Basin provide a complete record of regional Variscan tectonism, and specifically, information about the timing and nature of migmatization, magmatism, deformation, and exhumation of the proximal Montagne Noire gneiss dome in the Permian. No provenance assessment has previously been done on Upper Paleozoic strata in the region, so this work provides a baseline dataset for future paleotectonic studies in Western Europe.

Regional Geologic Setting

Global geography in the Late Paleozoic was governed by the formation of the supercontinent Pangaea, and uplift of the low-latitude Central Pangaeian Mountains, which spanned roughly 1000 km wide and 8000 km long, from the Appalachian-Ouachita-Marathon belt of east-central North America to the Variscan Mountains of Western Europe (Fig. 3; Zeigler et al., 1979; Matte, 1986; Ziegler, 1996). The Variscan (Hercynian) Orogeny was a long-lived, polyphase, arc-continent collision event extending from Early Ordovician to Late Permian time (ca. 500-290 Ma), as Laurasia (north) and Gondwana (south) collided (Fig. 3; Matte, 1986; Stampfli, 2001; Murphy and Nance, 2008). Several microcontinents, including Avalonia, Armorica, and peri-Gondwanan arc terranes were wedged in the collision zone (Fig. 1, inset), and ocean basins (such as the Iapetus and Rheic) opened and closed during intervals between continental convergence (Matte, 2001). Post-Variscan orogenic collapse in Western and Central Europe subsequently resulted in extension and subsidence, forming about seventy Permo-Carboniferous strike-slip to extensional basins along long-lived Variscan fault systems, many of which occur in the Massif Central (Fig. 2; Menard and Molnar, 1988; Van Den Driessche and Brun, 1989; Malavieille, 1993; Burg et al., 1994; Becq-Giraudon and Van Den Driessche, 1994; McCann et al., 2006; Roscher and Schneider, 2006). Hence, the Variscan Massif Central, and the Permo-Carboniferous basins within it, records the exceptionally complex tectonic evolution of rifting, convergence and collision, horizontal thrusting and crustal thickening, crustal extension, basin formation, and magmatism related to the Late Paleozoic Variscan Orogeny.

The Graissessac-Lodève Basin (Fig. 2), on the southern border of the French Massif Central, is a small Late Paleozoic continental rift basin that formed as a result of the north-south oriented extension associated with post orogenic collapse of the Variscan Mountains ca. 300 Ma (Menard and Molnar, 1988; Van Den Driessche and Brun, 1989, 1992; Burg et al., 1990; Echtler and Malavieille, 1990; Faure et al., 1990; Malavieille, 1993; Becq-Giraudon and Van Den Driessche, 1994). The basin covers an area of ~150 km² and contains a thick (4530 m) Permo-Carboniferous siliciclastic section that dips 45°-5° southward, and onlaps Variscan (Precambrian-Cambrian) metamorphic basement (marble and schist) along the northern margin of the basin (Fig. 2; Pochat et al., 2005; Schneider et al., 2006). The only radiometric ages previously obtained from the Graissessac-Lodève Basin sedimentary fill are from thin, intercalated ash beds within the Salagou (Octon Member), Loiras-Viala, and Houillière formations, yielding U/Pb zircon ages of 280 Ma, 288 Ma, and 300 Ma, respectively (Korner et al., 1999; Bruguier et al., 2003; Korner et al., 2003; Schneider et al., 2006). Regardless, these strata are fairly well correlated to those in other European Permo-Carboniferous basins (e.g. St. Affrique) using lithostratigraphy, and microfloral/insect biostratigraphy data (Broutin et al., 1992; Korner et al., 2003). The Lodève Basin exhibits a half-graben geometry, bounded by several faults (Santouil, 1980; Van Den Driessche and Brun, 1989), and developed along the hanging wall of the north-dipping Espinouse detachment. Shearing along the Espinouse detachment is documented around 295 ± 5 Ma, controlling basin subsidence, and initiating Montagne Noire core complex exhumation along the footwall (Fig. 4; Van Den Driessche and Brun, 1989, 1992; Pitra et al., 2012). Most of the displacement along the detachment occurred rapidly in the

Late Carboniferous and Early Permian, but continued into the Late Permian (Van Den Driessche and Brun, 1989; Becq-Giraudon and Van Den Driessche, 1993; Pochat and Van Den Driessche, 2011).

The Montagne Noire core complex, adjacent to the west-southwest of the Graissessac-Lodève Basin (Fig. 4) is primarily composed of migmatized orthogneiss and micaschist, intruded by Late Variscan granodiorite, and is overlain by Late Neoproterozoic-Early Cambrian schist and marble (Gèze, 1949; Bogdanoff et al., 1984). The timing of core complex exhumation remains unclear. Analogous Late Carboniferous basins located proximal to metamorphic domes in the southern Massif Central, such as the St. Affrique basin (adjacent to Levezou Dome) and the Alès basin (adjacent to Velay Dome), contain clasts of granite and orthogneiss that indicate these domes were denuded ~300 Ma (pers. commun Van Den Driessche). Oddly, pebbles of the Montagne Noire metamorphic dome occur in Pliocene-Miocene facies south of the Montagne Noire dome, but are seemingly absent in the Carboniferous-Mesozoic units (Cagnard, unpublished). Accordingly, complete exhumation of the Montagne Noire Dome was previously assumed to have not occurred until the Pliocene.

Chapter 2: Graissessac-Lodève Basin Stratigraphy

The following descriptions of Carboniferous-Permian siliciclastic units in the Graissessac-Lodève Basin are based primarily on facies observations and paleocurrent data (reconstructed to modern coordinates) summarized by Pochat et al. (2005) and Schneider et al. (2006) (Figs. 5 and 6). Previous workers interpreted these strata to record deposition in alluvial-fluvial, deltaic, and lacustrine environments (Odin, 1986; Odin et al., 1987; Pochat et al., 2005; Schneider et al., 2006; Lopez et al., 2007; Pochat and Van Den Driessche, 2011), and the up-section transition from grey to red coloration to generally reflect increased aridity and seasonality in the Early-Middle Permian (Korner et al., 2003; Schneider et al., 2006).

Croix de Mounis Formation (Upper Carboniferous)

Exposed in the far west of the Graissessac-Lodève basin, the Croix de Mounis Formation lies unconformably above Cambrian marble basement with an irregular, S-SE steeply dipping contact. It consists exclusively of a poorly sorted, disorganized, matrix-supported pebble to boulder conglomerate, ~250 m thick, with local thin (~.25 m) sandstone layers. Clasts comprise angular to rounded (and rarely striated) Cambrian marble, quartzite, and granite. This formation is interpreted to record proximal (northwest) to distal (southeast) alluvial-fan deposition (Pochat and Van Den Driessche, 2011), or glacial origin (Becq-Giraudon et al., 1996).

Pabau and Houillère Formations (Upper Carboniferous)

The uppermost Carboniferous Pabau and Houillère formations are exposed in a reclaimed open pit coal mine. Alternating 1-1.5 m beds of medium-grained sandstone, siltstone, carbonaceous grey-black shale, and coal beds (Pabau Formation) grade up-section to a very coarse-grained, arkosic-micaceous sandstone in 0.5-2 m, structureless beds (Houillère Formation). Sedimentary structures in lower units include graded beds, cross stratification, and wave ripples, interpreted to record accumulation in a fluvial-deltaic environment (Pochat and Van Den Driessche, 2011). They may also indicate sub-lacustrine fan (and turbidite) deposits, or distal lacustrine environments in which three distinct sedimentation cycles are recognized (Odin et al., 1987).

Usclas Formation (Lower Permian)

The sample locality of the lower Permian Usclas Formation consists of internally massive, 0.20-1 m thick beds of siltstone to medium-grained sandstone. Local meter-scale crossbeds indicate east-directed paleoflow (Pochat et al., 2005). The Usclas Formation is interpreted to have accumulated on a lacustrine delta front (lower) to ephemeral lacustrine (upper) environments (Odin, 1986; Pochat et al., 2005).

Loiras and Viala Formations (Lower Permian)

An abandoned uranium mine exposes a ~150 m up-section transition from ~0.5 m thick beds of grey-green calcareous mudstone-siltstone and interbedded red and black

mudstone (Loiras Formation), to structureless red mudstone (Viala Formation). Thinly bedded sandstone and finely laminated siltstone exhibit current ripples, hummocky cross stratification, desiccation cracks, and raindrop impressions. Paleocurrent information from current ripples and large-scale cross bedding in the Viala Formation, together with eastward thinning of the unit (from 330-50 m), indicates northeast-directed flow (Pochat et al., 2005). Pochat et al. (2005) inferred a transition from shallow to very shallow lacustrine environments, whereas Odin (1986) and Schneider et al. (2006) posited an evolution from lacustrine to fluvial environments during seasonal, semiarid conditions.

Rabejac Formation (Lower to Middle Permian)

The basal Rabejac Formation exhibits an erosional contact with the Viala Formation, and consists of a 0.5-1 m thick, moderately sorted, matrix-supported, angular-subangular pebble conglomerate. Clast compositions include intraclasts of underlying red mudstone (east), and clasts of Cambrian marble (west; Pochat et al., 2005). Above the basal conglomerate, the unit fines upward to red, coarse-grained sandstone with subangular grains of quartzite and mudstone, and abundant raindrop impressions and desiccation cracks. Clast sizes within the basal conglomerate increase to the west, and together with paleocurrent data, indicate dominantly east-directed paleoflow (Pochat et al., 2005). Depositional environments were alluvial plain-floodplain environment with ephemeral ponds (Schneider et al., 2006).

Salagou Formation (Middle to Upper Permian)

The basal Salagou Formation consists of a lenticular, siltstone to medium-grained sandstone, yielding up section to hundreds of meters of thickly bedded, internally massive red siltstone and mudstone with tan calcareous siltstone and abundant desiccation cracks (Octon Member). The uppermost Salagou Formation has a 2-2.5 m-thick internally massive bed of medium-grained, well-sorted, clean red sandstone. Rare cross-bedded, coarse-grained sandstone beds indicate northeast and southeast paleoflow, indicating sediment transport generally from the west (Pochat et al., 2005; Pochat and Van Den Driessche, 2011). Pochat et al. (2005) used ripple crest orientations to calculate paleowind directions emanating from N-N20°E. Deposition of these sediments is interpreted to have occurred in a large, shallow lake (Pochat et al., 2005) or a playa lake (Odin, 1986; Schneider et al., 2006). The Octon Member (lower Salagou Formation) records ephemeral lacustrine and fluvial deposits (calcareous siltstone) during a more arid interval (Odin, 1986; Schneider et al., 2006).

Chapter 3: Methods

Sampling

We collected eight 3-4 kg samples representing six formations, from the Upper Carboniferous (Croix de Mounis Formation) through Upper Permian (Salagou Formation) section of the Graissessac-Lodève Basin for U-Pb detrital zircon analyses (Fig. 7). We relied on 1:50,000 geologic maps of the Lodève and Bédarieux regions (BRGM, 1982), and stratigraphic columns and facies descriptions from previous work (Fig. 5; Pochat et al., 2005; Schneider et al., 2006; Lopez et al., 2007; Pochat and Van Den Driessche, 2011) to guide sample collection. We logged facies descriptions several meters above and below each sample site, and collected 52 hand samples of mudstone- to coarse-grained sandstone for petrographic analyses from all detrital zircon sample collection locations and several supplementary locations (App. E-1).

Detrital Zircon Geochronology

Samples for detrital zircon geochronology were processed at the University of Arizona LaserChron Lab using traditional methods of heavy mineral separation described by Gehrels et al. (2008), involving a Wilfley table, density separation with methylene iodide, and a Frantz magnetic separator to eliminate strongly magnetic particles. All zircons in the final heavy mineral fraction were retained. Each sample yielded >200 zircon grains that were mounted into 1" diameter epoxy with standard zircon grains (R33 and SL). These mounts were ground and polished to a depth of ~20 μm , exposing grain interiors, and then cleaned and imaged. High-resolution back-

scattered electron (BSE) images for each detrital zircon mount were acquired (Fig. 8, App. E-2), allowing for differentiation of separate grains, and high-resolution CL images of zircons from each sample show the complexities within the grains. U/Th versus age plots for analyzed zircons from all detrital samples (Fig. 9) illustrate the nature of zircon crystallization: zircon with metamorphic origins commonly show U/Th > 10, whereas igneous zircons exhibit U/Th < 10 (Gehrels et al., 2008).

Eight samples were analyzed with the laser ablation multi-collector inductively coupled plasma mass spectrometer (LA-MC-ICPMS), with methods described by Gehrels et al. (2008). To avoid bias, grains were randomly selected for each analysis with the laser (spot size of 30 μm), avoiding cracks, inclusions, and potential metamorphic rims. Ages of each zircon were calculated using measured levels of ^{278}U , ^{235}U , ^{206}Pb , ^{207}Pb , and Th in its isotopic system, and $^{206}\text{Pb}/^{238}\text{U}$ and $^{207}\text{Pb}/^{235}\text{U}$ decay systems; specifically using the ratios $^{207}\text{Pb}/^{206}\text{Pb}$ for grains >1000, and $^{206}\text{Pb}/^{238}\text{U}$ for grains <1000. Data that are >20% discordant or >5% reverse discordant (by plotting $^{206}\text{Pb}/^{238}\text{U}$ and $^{207}\text{Pb}/^{235}\text{U}$ isotopic ratios on concordia plots; Fig. 10) are eliminated, as well as analyses exceeding a 25% uncertainty filter (1σ). Probability density plots (PDPs) are a robust presentation of measured zircon ages and uncertainties in each sample (Fig. 10), where heights of peaks correspond to statistical significance (Gehrels, 2010). These plots illustrate the presence of specific age populations, but with an average sample size of only 90-100 grains, they may capture a biased visual representation (Gehrels et al. 2012; Vermeesch, 2012; Satkoski et al., 2014). Kernel Density Estimate (KDE) plots are an alternative method for plotting age distributions (App. E-3) wherein the uncertainty on each age is increased, “smoothing” the

distribution curve and including a wider range of probable ages. Some suggest that KDE plots have a firmer theoretical basis (Vermeesch, 2012). Normalized probability plots were generated to display normalized age spectra (PDPs), such that the area under all curves is equal (Gehrels, 2010), enabling qualitative comparison of age distributions among samples. Cumulative age probability plots (App. E-4) also show the summed probability of finding zircon of a specific age in a given sample, but are plotted with increasing age, and allow qualitative observation of overall patterns in a set of age distributions (Gehrels, 2010).

To quantitatively gauge degrees of similarity and dissimilarity among age populations of detrital zircon in the samples analyzed, statistical comparisons were made using the Kolmogoroff-Smirnoff (K-S) statistical test, the Overlap-Similarity test, and the “Likeness” test. The K-S test quantitatively compares detrital zircon age spectra between two or more samples to evaluate the probability (P value) that age distributions originated from different populations (Press et al., 1986). The Overlap-Similarity test measures the degrees of age overlap and proportional similarity between two age probability curves based on 1σ uncertainty (Gehrels, 2000). Most recently, the Likeness metric was developed to evaluate the degree of sameness among detrital zircon age populations in stratigraphic context by quantifying the degree of overlap between pairs of PDPs (Satkoski et al., 2014). Although the K-S test is the most familiar means of statistical comparison in detrital zircon studies, differing P values do not correlate directly to degrees of dissimilarity (Guyunn and Gehrels, 2010). Here, we employ all three tests to achieve a more complete quantitative analysis of degrees of similarity or dissimilarity among samples.

Sandstone Petrography

To assess framework mineralogy, point counts were conducted on 21 thin sections stained for potassium feldspar. Two to four thin sections per formation from the Upper Carboniferous through Lower Permian section were analyzed to capture compositional variation temporally within and among all formations in the Graissessac-Lodève Basin. Both the “traditional” point-count method (Suttner, 1974; Graham et al., 1976; Ingersoll et al., 1984), and the Gazzi-Dickinson method (Dickinson, 1970; Ingersoll et al. 1984) were employed. In the traditional method, a sand-sized crystal ($>62.5 \mu\text{m}$) within a larger fragment is classified in the category of the larger fragment, rather than as the crystal itself. Alternatively, the Gazzi-Dickinson method classifies any sand-sized grain by its mineralogy, regardless of whether it occurs as a monocrystalline grain, or within a rock fragment. This combined approach serves to (1) minimize grain-size influences on framework mineralogy while retrieving maximum information about source rock terranes and tectonic origins, and (2) shed more light on the transport history of detrital grains. The reliability of point count results is shown with error ranges (Table 1), calculated based on Van Der Plas and Tobi (1965) to evaluate the accuracy of modal analyses within 2σ error. Framework mineralogy was determined by point counting 400 framework grains from each thin section. Modal compositions of several samples could not be determined owing to grain sizes below the minimum needed ($62 \mu\text{m}$) for applying the Gazzi-Dickinson point count method.

Subsidence Analysis

Subsidence analysis of the Graissessac- Lodève Basin was done using OSXBackstrip (Cardozo, 2013) to perform 1D Airy backstripping (App. E-5). To determine cumulative and tectonic subsidence, the magnitude and timing of effects from the following were included: (1) present day absolute ages and thicknesses of stratigraphic units (2) sediment compaction, and (3) variation in water depth during deposition. There is no drill core or measured section from a single locality that captures the complete thickness of the Graissessac-Lodève basin Permo-Carboniferous record, so an idealized stratigraphic column (Fig. 5), reconstructed to represent maximum present-day thickness of all units was used (4530 m total; Pochat and Van Den Driessche, 2011). Inputs, formulas, and assumptions used in this program to generate the tectonic subsidence curve are reported in Appendix E-5.

Chapter 4: Provenance Results

Table 1 and Figure 12 provide a summary of framework mineralogy from 21 sandstone thin sections (2-4 from each formation), and more detailed results of petrographic analyses (e.g. feldspar classification, quartz grain undulosity) are reported in Appendix D. In all samples, polycrystalline quartz predominates, and monocrystalline quartz is typically strained. Back-scatter electron (BSE) images show characteristic morphologies of zircon grains from each detrital sample (Fig. 8). Full analytical detrital zircon age data (eight samples, representing six formations) are reported in Appendix C. Zircon ages are summarized in Table 2, and are graphically represented on age-probability and concordia diagrams (Fig. 10). Each sample yields an average of 92 grains with concordant ages. Rare, slightly discordant ages (≥ 1800 Ma) likely indicate partial lead loss in the U-Pb isotopic system (Dickinson and Gehrels, 2008). Ninety-seven percent of all analyzed zircon grains in this study have U/Th ratios less than 10 (Fig. 9), consistent with an igneous origin. All statistical tests (Table 3) show relatively consistent results.

Croix de Mounis Formation (XDM)

Framework mineralogy ($n = 3$) averages 49% quartz, 1% feldspar (81% plagioclase: 19% potassium), and 52% metamorphic lithic fragments. Zircon grains are small (most 25-50 μm ; all ≤ 100 μm), colorless, and moderately rounded, with rare euhedral grains. Cracks and inclusions are common overall, and euhedral grains exhibit concentric zoning. The majority of U-Pb zircon ages fall in a broad age peak from 864-

544 Ma, with a main age peak at 643 Ma. Auxiliary age peaks include 307 Ma, 1000 Ma, 1260 Ma and multiple peaks between 1910-2700 Ma. Statistical tests demonstrate a lack of similarity or overlap between the Croix de Mounis Formation and other analyzed units.

Pabau and Houillère Formations (PAB and HOU)

Framework mineralogy of the Houillère Formation (n = 2) averages 63% quartz, 34% feldspar (75% potassium: 25% plagioclase), and 3% metamorphic lithic fragments. Point counts of samples (n=3) from the Pabau Formation average 60% quartz, 15% feldspar (94% plagioclase: 6% potassium), and 25% metamorphic lithic fragments. Detrital zircons were not analyzed from the Pabau Formation. Zircon grains in the Houillère Formation detrital sample are colorless and small (all $\leq 100 \mu\text{m}$; most $\leq 25 \mu\text{m}$), and well to moderately rounded. Grains are broken and cracked and concentric zoning is rare. The detrital zircon age spectrum yields a narrow, primary age peak from 365-307 Ma, with a peak mode at 343 Ma, a subordinate age peak at 486 Ma, and a small, broad age peak between 651-545 Ma, followed by numerous minor peaks between 2100-2000 Ma. The Overlap-Similarity test shows an age overlap between the Houillère and Middle Salagou formations (P= 0.80), but different proportions (P= 0.64). Other tests demonstrate a lack of similarity between the Houillère Formation and other analyzed units.

Usclas Formation (USCL)

Framework mineralogy (n = 4) from the Usclas Formation averages 49% quartz, 50% feldspar (45% plagioclase: 55% potassium), and 1% metavolcanic lithic fragments. The plagioclase feldspar (counted as such) in this sample has been pervasively altered to sericite (App. E-7), a unique form not found in other samples. Zircon grains are colorless, small (mostly 50-60 μm), and moderately to poorly rounded, with some prismatic grains. Many grains have cracks and inclusions, and concentric zoning is apparent in $\sim 10\%$ of the grains, most of which are more often euhedral. The detrital zircon age spectrum for the Usclas Formation is nearly unimodal, yielding a narrow principal age peak at 460 Ma. There is also a small peak at 618 Ma, and several minimal age populations between 372-281 Ma, and 2023-755 Ma. Statistical tests demonstrate a lack of similarity or overlap between the Usclas Formation and other analyzed units.

Loiras Formation (LRS)

The Loiras Formation is too fine-grained to enable point counting for framework mineralogy. Detrital zircon grains in the Loiras Formation are small (all $\leq 100 \mu\text{m}$; most 25-30 μm), colorless, and well to moderately rounded. Cracks are common and there are core and rim zones present in very few grains. A multimodal age distribution includes main age peaks at 302 Ma and 463 Ma, and several successive peaks that gradually decrease in dominance with age, including 600, 690, 769, 859, 940, 1754 Ma. Small age groups exist between 1962-1761, 2066, and 2596 Ma. All statistical

comparisons show a strong similarity ($P > .05$, K-S) and overlap of ages and proportions ($P_{\text{avg}} > .75$) between the Loiras Formation and all three Salagou Formation samples.

Rabejac Formation (RAB)

Framework analyses of the Rabejac Formation ($n = 2$) averages 57% quartz, 28% feldspar (71% plagioclase: 29% potassium), and 15% metamorphic lithic fragments. Zircon grains are colorless and variable in size (50-120 μm ; most $\sim 80 \mu\text{m}$), moderately rounded to commonly euhedral, rarely cracked, and most exhibit distinct zoning. Concordant analyses yield a main age peak at 305 Ma, secondary population peaks at 453 and 649 Ma, and less significant populations at 716, 775, 2200-800 Ma, and 2900-2600 Ma. The K-S test suggests the Rabejac Formation has a unique provenance relative to other samples ($P < .05$), but the Overlap-Similarity test detects parallels with the Middle Salagou Formation ($P > .78$).

Salagou Formation (SAL)

Framework mineralogy of the Lower Salagou Formation ($n = 4$) shows detrital modes averaging 39% quartz, 44% feldspar (91% plagioclase: 9% potassium), and 17% metamorphic lithic fragments. Framework analyses of detrital grains from the Upper Salagou Formation ($n = 3$) average 55% quartz, 31% feldspar (90% plagioclase: 10% potassium), and 14% metamorphic lithic fragments. Multiple petrographic samples ($n = 5$) collected from the middle Salagou Formation consist exclusively of massive red

mudstone, and are too fine grained for point counting. BSE images of zircon grains from three Salagou Formation samples show colorless, well to moderately rounded zircons, with rare euhedral grains. Zircon sizes vary in each sample: In the Lower-Middle Salagou most are 50-70 μm , with much larger euhedral grains, and in the Upper Salagou sizes range from 20-100 μm , the majority $\sim 30 \mu\text{m}$. Fractures and inclusions are rare to absent in the lower to middle Salagou zircon samples, but common in the uppermost zircon samples, and concentric zoning is exclusive to euhedral grains. Concordant analyses yield a principal age peak at 460 Ma in all three samples. The middle and upper Salagou age distributions also contain equally dominant age peaks at 287 and 294 Ma, respectively, and the basal Salagou sample has a subordinate age peak at 311 Ma. The uppermost Salagou Formation has a third main peak at 630 Ma, whereas the middle Salagou Formation has a smaller, broad peak (688-573 Ma) and the basal Salagou a slightly younger, minor age peak at 550 Ma. All three samples contain additional ages between 836-711 Ma, 1060-915 Ma, 2160-1856 Ma, 2920-2498 Ma. All statistical analyses detect similar ages and proportions within the three Salagou Formation samples ($P > .05$ K-S; $P_{\text{avg}} > .75$ O-S; 60% Like) as well as with the Loiras Formation (mentioned previously).

Basin Subsidence

The tectonic subsidence [residual] plot (Fig. 13) of the backstripped Carboniferous-Permian Lodève Basin shows the tectonic subsidence curve (See Appendix E-5 for inputs and sources, and “Methods” chapter for assumptions). The

subsidence history of the Lodève Basin includes two distinct tectonic phases with varying rates of subsidence. First, there is rapid Late Carboniferous (300-295 Ma) tectonic subsidence of 1.56 km over 5 Ma (312 m/My). Using the alternative 295 Ma age of basin formation (posited by Poilvet et al., 2011; Pitra et al., 2012), this initial subsidence rate is even more rapid, subsidising by the same amount in <1 Ma (1500 m/My). Subsequent early-late Permian (295-258 Ma) subsidence of 2.55-2.61 km persisted over 37 Ma (70 m/My), and likely ceased in the Early Triassic (ca. 250 Ma).

Chapter 5: Discussion

Detrital zircon geochronological data are presented on normalized probability plots (Fig. 14) that display age spectra for all eight samples, and denote main age populations (summarized in Table 2) with colored bars. These age groups are separated by natural age breaks (App. C), and include Middle Carboniferous-Early Permian (330-285 Ma), Late Devonian-Early Carboniferous (378-331 Ma), Cambro-Ordovician (552-445 Ma), Late Neoproterozoic (615-555 Ma), Early-Middle Neoproterozoic (1000-617 Ma), and Mesoproterozoic-Archean (3000-1000 Ma). Sandstone framework modes are cast on QFL and QmFLt ternary plots (Fig. 15; Table 1; Dickinson et al., 1983), and supplement detrital zircon data in evaluating siliciclastic provenance in context of tectonic setting. Possible source terranes include plutonic (granite), volcanic (tuff), and metamorphic (orthogneiss protolith ages, “Schistes X”). Provenance terranes are considered in areas both proximal (Fig. 16) and distal (Fig. 17 and 18) relative to the Graissessac-Lodève Basin.

Vertical Trends

Detrital Zircon Geochronology

All Permo-Carboniferous formations in the stratigraphic section contain relatively similar detrital zircon age populations, except the statistically unique Croix de Mounis Formation. However, the dominant (peak) age population changes for each unit, and proportions shift through time. The oldest grain populations (3000-1000 Ma) make up 15-25% of the zircon population in younger units (Loiras and upper Salagou

formations), and are minor lower in the section (only 5-9% for Usclas-Houillère formations). When binned into three separate categories according to natural age breaks in the zircon populations (Mesoproterozoic 1300-1000 Ma, Paleoproterozoic 2200-1600 Ma, and Early Paleoproterozoic-Archean >2200 Ma), the majority of older ages in each unit are consistently Paleoproterozoic (avg. 8%) rather than Mesoproterozoic (avg. 4%) or Archean (avg. 4%). Neoproterozoic (1000-555 Ma) ages predominate in the Croix de Mounis Formation (79%), more so than in other units, and represent an especially wide range shown by a broad peak (Fig. 14). These ages compose only 21-25% of the population in the Houillère, Usclas, Rabejac, and lower Salagou formations, and are significant (39-48%) in the Loiras and middle-upper Salagou formations. Qualitatively, the normalized probability plots for all samples exhibit a biased distribution with higher population peaks between ca. 615-555 Ma; however, all samples contain more grains between 1000-617 Ma (Early-Middle Neoproterozoic grains; avg. 28%) than Late Neoproterozoic ages (avg. 9%). Cambro-Ordovician (552-445 Ma) ages are insignificant in the Upper Carboniferous (Croix de Mounis: 4%), but predominate in the Lower Permian Usclas Formation (59%). These ages occur in other Permian units, but with no distinct pattern: 11-17% (Loiras, Rabejac, upper Salagou), and 23-32% (lower-middle Salagou). Late Devonian-Early Carboniferous (378-331 Ma) grains predominate uniquely in the Houillère Formation (41%), and are absent to rare in all other units (0-9%). The youngest population of grains (330-285 Ma) appears first in the Loiras Formation (15%), predominates in the Rabejac Formation (39%), and persists through the Salagou Formation (11-18%).

Statistical comparison of all analyzed samples yield P-values and percentages that show each formation records a unique provenance signature, with the exception of the strong similarity between the Salagou and Loiras formations. This is surprising because these units are not stratigraphically contiguous, separated by the Rabejac and Viala formations (Fig. 5).

Framework Mineralogy

All sandstone samples exhibit significant feldspar and/or lithic contents, plotting as subarkosic to litharenite (Fig. 15). Plagioclase feldspar (71-94%) dominates in most of the samples (Table 1), with the exception of the Usclas and Houillière samples, wherein potassium feldspar (55-75%) predominates. Overall, polycrystalline quartz is prevalent, and monocrystalline quartz typically exhibits a strained or undulose texture (App. D-2), consistent with a metamorphic origin (Basu et al., 1974).

The lowermost samples in the section (Croix de Mounis and Pabau formations) contain abundant metamorphic lithic fragments (52-25%, respectively), and relatively little feldspar (1-15%, plagioclase). These samples plot in the “recycled orogen” field on ternary diagrams (Fig. 15), sourced from orogens that have experienced partial metamorphism or uplifting along fold and thrust belts (Dickinson and Suczek, 1979; Dickinson et al., 1983). They are not quartzose, craton-derived material, but are intermediate in composition (containing feldspar), suggesting some influence of igneous source terranes (Dickinson et al., 1983). The Rabejac and the majority of the upper Salagou formation samples are slightly more quartzose than older formations, have intermediate felsic-lithic ratios, and also plot as “recycled orogens” (Fig. 15). Elevated

feldspar content in these samples (avg. 30%) may signify onset of a plutonic contribution. The lower Salagou Formation is feldspathic (44%, mainly plagioclase), and plots in the “dissected arc” tectonic setting. Detrital modes plotting in this cluster are generally arkosic, and similar to sands derived from granitic and gneissic basement uplifts within continental blocks (Dickinson et al., 1983). None of the exposed basement terranes resemble a relict magmatic arc, so samples clustered in the “dissected arc” tectonic setting (Fig. 15) likely reflect eroding granitic or gneissic basement (within the continental block) with a localized intermixing of metamorphic lithic grains from the recycling of cover rocks (Dickinson et al., 1983). The Houillière and Usclas Formations are [potassium] feldspar-rich (34% and 50%, respectively), and lithic-poor (1-3%), and reflect derivation from transitional continental or basement uplift sources (Fig. 15).

Potential Sources for Detrital Zircon Grains

Possible source terranes in the Variscan Belt are discussed according to natural age groupings of zircon populations (Fig. 14; Table 2).

Archean-Precambrian Ages (3000-1000 Ma)

Precambrian basement terranes south of the Variscan suture comprise accreted island-arc terranes subsequently buried by thick Proterozoic-Lower Paleozoic passive margin sediments prior to the Variscan orogeny, and thus Precambrian crystalline basement is not known in the Massif Central, nor anywhere south of the Variscan suture zone (Mattauer, 2004). The only remnants of old cratonic basement in the Variscan belt

(Fig. 18) are small exposures of 2200-1800 Ma Icartian Gneiss in the northern Armorican Massif (Brittany and the Channel Islands) and the Svetlik (2100-2050 Ma) and Dobra (1380 Ma) gneisses of the Bohemian Massif (Linnemann et al., 2007); these ages also resemble Eburnean basement (2100 Ma) and intrusions (2200-1800 Ma) that occur on the West African craton (Allegre and Ben Othman, 1980). The Bohemian Massif is dominated by > 2050 Ma basement (Saxo-Thuringian Eburnian basement 2100-1700 Ma, and Moldanubian Icartian basement 2000 Ma), and may also represent a source for Precambrian zircons. Archean (3200-3000 Ma) ages are characteristic of metavolcanic sources on the West African craton (Montero et al., 2007) or other peri-Gondwanan terranes to the south (Fig. 18), and are often contained as intercalated blocks in Cadomian (650-500 Ma) basement terranes (Fig. 18; Murphy et al., 2004). In summary, Archean-Precambrian zircon populations are not local, and likely reflect derivation from reworked basement terrane (deeply buried accreted terranes) in recycled sedimentary or metasedimentary units.

Neoproterozoic Ages (1000-555 Ma)

Most samples present a natural age break between Early-Middle (1000-617 Ma) and Late (615-555 Ma) Neoproterozoic. Basement terranes ca. 1000 Ma are unknown for Western Europe south of the Variscan suture (Mattauer, 2004), and are inferred to reflect reworked Gondwanan, or peri-Gondwanan terranes, such as Avalonia (e.g., 1300-1000 Ma Britain and Brabant Massif) or Amazonia/Oaxaquia, a land mass possibly connected to western Iberia (Fernandez-Suarez et al., 2000; Murphy et al., 2004), and therefore to the west-southwest of northern Gondwana (Massif Central), in the Neoproterozoic (Fig. 18). Cadomian basement (650-500 Ma) characterizes the

Armorican and Iberian Massifs, and the Moravo-Silesia zone of Bohemia (590-550 Ma) (Fig. 18; Murphy et al., 2004). Other Late Neoproterozoic ages may reflect 700-677 Ma plutonism in Britain and Wales (Avalonia) and 616-540 Ma volcanism and plutonism in the northern Armorican Massif (Murphy et al., 2004), as well as 600-575 Ma volcanism and plutonism in northwestern Iberia associated with the Pan-African arc-continent collision where 650-700 Ma and 850-900 Ma ages represent older components of the Pan-African arc (Montero et al., 2007). In summary, Neoproterozoic-Cambrian ages (1000-555 Ma) represent recycling from Neoproterozoic metasediments that contain remnant material from distal sources; notably, the > 545 Ma metasedimentary “Schistes X” which formerly covered the Montagne Noire Dome (Fig. 19).

Cambro-Ordovician Ages (552-445 Ma)

Middle Ordovician (494-450 Ma) felsic, calc-alkaline magmatism and volcanism caused by post-Cadomian to early Variscan subduction, rifting and back-arc extension along the northern Gondwanan margin was widespread in the Variscan Belt, marked by regional evidence in the Massif Central (Montagne Noire), the southern Armorican Massif, and the Iberian Massif (Fig. 18; e.g. Bard, 1978; Pin and Marini, 1993; Soula et al. 2001; Mattauer, 2004, Roger et al., 2004; Montero et al., 2007; Balleuvre et al., 2012, Pitra et al., 2012).

The emplacement [protolith] age of migmatized granitic orthogneiss in the southern Massif Central ranges from 480-450 Ma (Fig. 17; Roger et al., 2004; Cocherie et al., 2005; Melleton et al., 2010; Diez Fernandez et al., 2012; Arenas et al., 2014). These granitoids intruded the lower metasedimentary “Schistes X” (Fig. 4c), and were

subsequently deformed into orthogneiss during Variscan compression and deformation (Debat, 1974; Bard, 1978; Lescuyer and Cocherie, 1992; Cocherie et al., 2005).

Locally, 470-450 Ma calc-alkaline augen orthogneiss (e.g. Gorges d'Heric, Pont du Larn, St. Eutrope) on the flanks of the Montagne Noire Dome (Fig. 16; Roger et al., 2004; Pitra et al., 2012) reveal the most proximal and likely sources for Ordovician zircons in the Graissessac-Lodève Basin. More distal to the north, the 469 Ma Pinet orthogneiss (Fig. 17; Melleton et al., 2010) also represents a potential source for Ordovician zircon, but is inconsistent with measured paleoflow. Cambro-Ordovician foreland basin metasedimentary rocks (schist and marble) on the north and south flanks of the dome (Fig. 4c; Bogdanoff et al. 1984), and Schistes X (> 545 Ma; Lescuyer and Cocherie, 1992) likely sourced zircons on the older end of this age group (550-500 Ma) recycled from distal Cadomian sources.

Middle Silurian- Middle Devonian Ages (430-394 Ma)

Zircon populations 430-394 Ma are essentially absent in all formations (0-6%), and may reflect a tectonic lull in the southern Massif Central.

Late Devonian- Early Carboniferous Ages (378-331 Ma)

High-pressure metamorphism persisted in the Late Devonian (380-350 Ma), and closure of the Rheic Ocean ca. 380 Ma led to collision of Laurentia, Baltica and Avalonia, with Gondwana and the Armorican microcontinent, in the Variscan orogeny (Matte, 2001; Arenas, 2014). Convergence persisted through the Carboniferous, causing extensive intracontinental metamorphism and deformation in the Variscan Belt (Arenas, 2014), chiefly in the northern and central Massif Central. Small exposures of 367-355

Ma volcanic units in the northwest Massif Central (Fig. 17) were generated during subduction of a magmatic arc and back-arc complex that formed in the Middle Devonian (Didier and Lameyre, 1971; Pin et al., 1982; Pin and Paquette, 1998; Roger et al., 2004). Zircon populations of this age are relatively insignificant in our section (solely exist in the Houillière Formation), and were difficult to explain due to the lack of Late Devonian- Early Carboniferous plutonic sources in the region (see “Provenance” section for further discussion).

Middle Carboniferous- Early Permian Ages (330-285 Ma)

The main phase of plutonism, volcanism, and migmatization, chiefly in the Massif Central, is related to post-orogenic, northeast-southwest crustal extension, and collapse of the entire Variscan belt occurred during the Middle to Late Carboniferous (Burg et al., 1994). The youngest detrital zircon age group (330-285 Ma) is prevalent in Permian formations of the Lodève Basin (Loiras, Rabejac, and Salagou). Two distinct crustal melting stages have been recognized in the Montagne Noire Axial Zone: (1) 319 ± 2 Ma migmatization and deformation of the dome, and La Salvetat-Laouzas granite emplacement, and (B) a second melting event 298-295 Ma, coeval with Montalet granite emplacement 294 ± 3 Ma (Maluski et al., 1991; Poilvet et al., 2011; Poujol et al., in review). Granite emplacement in the nearby Velay Dome is also dated at ca. 300 Ma (Didier and Lameyre, 1971; Malavieille et al., 1990; Ledru et al., 2001). Interbedded 298-295 Ma tuff horizons in the Graissessac-Lodève basin, as well as several other Permo-Carboniferous sedimentary basins in the southern Massif Central (e.g., Roujon-Neffies, Cevennes, Jaujac, Bertholene; Fig. 17), document the climax of

short-lived explosive volcanism in the southern Massif Central (Bruguier et al., 2003); the extrusive component of Late Carboniferous magmatism.

Provenance and Tectonic Implications

The Upper Carboniferous section of the Graissessac-Lodève basin directly overlies Neoproterozoic- Lower Cambrian (> 545 Ma) metasedimentary basement (Schistes X), exposed at Mont de Lacaune, just north of the Lodève Basin (Fig. 19). Schistes X is a biotite-granite-stauroilite micaschist that previously covered the Montagne Noire dome (Fig. 19; Bogdanoff et al., 1982; Van Den Driessche and Brun, 1989; Lescuyer and Cocherie, 2002). Archean through Cambrian zircon populations require derivation from distal terranes. Therefore, the presence of these ages in all analyzed formations reflects the prevalent recycling of sediment from Schistes X, which contains material originally derived from the West African craton (northern Gondwanan margin) or other distal Cadomian basement terranes (Fig. 18). The predominance of 1000-555 Ma Neoproterozoic grains (Fig. 14), and metamorphic lithic fragments (Fig. 15) in the Croix de Mounis Formation, together with east-southeast-directed paleoflow, identifies Schistes X as the principal source.

The principal 378-331 Ma peak (Fig. 14) and a potassium feldspar-dominant framework mode (Table 2) define a unique source for the Houillière Formation. In the Massif Central, these ages correspond to timing of intense metamorphism and deformation, but apparently not plutonism since there are no known igneous bodies of this age in the region (Fig. 17). Thus, the presence of Late Devonian-Early

Carboniferous zircon populations in the Houillère Formation is explained by distal, or buried plutons that were proximal to the Graissessac-Lodève basin during the Late Carboniferous. The present-day configuration of the basin does not reflect its Late Paleozoic geometry, as several tectonic events such as the Pyrenean Orogeny have occurred since then. Thus, it is plausible that there are Late Devonian-Early Carboniferous sources that were uplifted and eroding at the time, and have been subsequently buried beneath thick, Paleozoic-Mesozoic sediment. There are several, deep (4-5 km) Permo-Carboniferous sedimentary basins in the area (e.g. the St. Affrique basin, just north of the Graissessac-Lodève basin), wherein the age and composition of basement remains largely unknown. Additionally, Triassic sediment was $\geq 1-2$ km thick (pers. commun. Pochat and Van Den Driessche, 2014), and has preferentially eroded, leaving expanses of thick sediment that may conceal the presence of deeply-buried plutonic sources for zircon in the Houillère Formation. This “phantom” source was apparently only uplifted and eroding briefly, as the Late Devonian-Early Carboniferous zircon population wanes to very few grains in the Usclas formation, and then absent in the up-section Permian formations (Fig. 14).

Ordovician ages predominate in the feldspar-rich Usclas Formation (45% plagioclase; 55% potassium), and were sourced principally from the 480-450 Ma “orthogneiss envelope” that surrounds the Montagne Noire dome (Fig. 16). The protolith for these orthogneiss units are granitoids that intruded the lower Schistes X before Variscan compression and deformation (Fig. 4). East-directed paleoflow, and subarkosic framework compositions (Fig. 15), are consistent with this interpretation. Cambro-Ordovician age populations, derived from the gneissic flanks of the Montagne

Noire dome, are substantial in all later Permian units (Loiras, Rabejac, and Salagou formations), and are especially prevalent in the Loiras and Salagou formations.

Orthogneiss composition in the Montagne Noire dome is variable (Demange, 1982; Soula et al., 2001); some have potassium feldspar-depleted compositions, and are rich in plagioclase feldspar (10%: 40%), while other compositions are dominated by potassium feldspar (40%: 10%). Upper Permian units (Loiras, Rabejac, Salagou) contain abundances of plagioclase, but a relative paucity of potassium feldspar (Table 1). It is likely that Permian formations have detrital contributions from local Ordovician orthogneiss with lower potassium feldspar compositions, compared to underlying units (Houillière, Usclas) that are sourced by Ordovician augen orthogneiss.

Notably, the Loiras and Salagou formations are fine grained (siltstone and mudstone) relative to older units (Fig. 6), but zircon grain sizes recovered from these samples approximate sizes of zircons from coarser-grained units (Fig. 8), possibly reflecting their derivation from the same sources. Although they are not stratigraphically contiguous (separated by the Rabejac formation), the Loiras and Salagou formations have statistically similar age populations (Table 3). It is possible that this inconsistency in provenance spectra (both age and composition) between the Rabejac Formation and the Loiras-Salagou formation may be influenced by a grain size or depositional environment bias, rather than a difference in source; the Rabejac is coarser, conglomeratic and interpreted as a fluvial deposit, while the Loiras and Salagou are largely composed of fine-grained, lacustrine mudstone.

The youngest 330-285 Ma age peak emerges in the Loiras Formation, predominates in the Rabejac Formation, and persists through the Salagou Formation.

These ages also appear to reflect local derivation from the Montagne Noire dome (Fig. 16), where granite emplacement ages are 320-294 Ma. The location of the Montagne Noire Dome directly west of the Graissessac-Lodève basin (Fig. 16) is consistent with documented east-directed paleoflow throughout the Permian (Pochat et al., 2005), and the angular, basal conglomerate of the Rabejac Formation signals a locally derived, proximal source. Other 330-300 Ma granitic bodies occur within the Massif Central, north of the Lodève Basin (e.g. Margeride Massif, Velay Dome), but are distal, and inconsistent with measured paleoflow. Early Permian volcanism was syn-depositional, evinced by 298-295 Ma volcanic ash layers interbedded in southern Massif Central Permo-Carboniferous basins (Fig. 17). Thus, remobilized zircon from these layers initially poses the most obvious provenance choice for the youngest zircon populations. However, the lack of volcanic lithic fragments, and prevalence of metamorphic lithic fragments and strained, polycrystalline and/or undulose (metamorphic) quartz (Fig. 11, App. D-2) refute this interpretation. Furthermore, such thin ash layers could not account for the voluminous zircons represented by the 300-285 Ma detrital populations (Gehrels et al., 2012). The re-appearance of older Neoproterozoic zircon populations (41-48%) in the Loiras-Upper Salagou Formations reflects the persistent unroofing of Schistes X from the Montagne Noire dome cover in the Permian, and explains why these formations plot as a “mixed” tectonic signal (Fig. 15), incorporating zircons from 330-294 Ma granitoids and 480-450 Ma orthogneiss, with significant numbers of older, reworked zircons (> 500 Ma).

Early Permian Exhumation of the Montagne Noire Dome

The ages of units that constitute the Montagne Noire core complex govern the main detrital age populations of Permian strata in the Graissessac-Lodève Basin, and signify deep-seated erosion (Fig. 19). Units associated with the Montagne Noire provenance include Late Variscan 320-294 Ma granitoids in the axial dome, adjacent 480-430 Ma orthogneiss on the flanks, and the Late Neoproterozoic- Early Cambrian metasedimentary Schistes X, which covered the dome prior to erosion, and contains older, recycled detritus (Archean-Cambrian) with Pan-African (northern Gondwanan) and Cadomian basement origins. Early Permian exhumation and erosion of the Montagne Noire metamorphic core complex (Figs. 16, 19) is evinced by:

(A) Significant 330-285 Ma zircon populations in the Loiras Formation (15%), Rabejac Formation (39%), and Salagou Formation (11-18%) that correspond with granite emplacement ages in the Montagne Noire Axial Zone.

(B) The re-appearance of substantial Neoproterozoic zircon populations in the middle-upper Permian units (39-48% Loiras-Salagou formations), presumably from erosion of metasedimentary Schistes X (former dome cover).

(C) The considerable presence of Ordovician zircon age populations interpreted to have been derived from orthogneiss on the flanks of the dome: 53% in the Usclas Formation (earliest Permian) and 23-32% in the Lower-Middle Salagou Formation.

(D) Framework compositions reflecting gneissic-granitic sources (Fig. 11).

(E) Consistencies with previous work in the basin (Pochat et al., 2005) that report east-northeast-directed Permian paleoflow, and coarse-grained local sedimentary signatures of lower Permian formations (e.g. Usclas, Rabejac).

At present, the tectonic interpretation for the formation of the Montagne Noire gneiss dome remains controversial (Van Den Driessche and Brun, 1992; Soula et al., 2001). Several ideas have been proposed that include ductile wrenching and diapirism from regional north-south shortening (Arthaud, 1970; Nicolas et al., 1977; Beaud, 1985; Mattauer et al., 1996; Matte et al., 1998). However, evidence for late Paleozoic post-Variscan extensional tectonics, thermal relaxation, and high temperature low-pressure metamorphism (peak 700°C at 5 Kb in the gneissic core; Fig. 4b; Soula et al., 2001), favors the extensional metamorphic core complex model (Van den Driessche and Brun, 1992). This involves isostatic uprising and deformation of the lower crust in an asymmetrical extensional system that generated roll-under folding of the footwall (Southern Nappes), basin development in the hangingwall (Graissessac-Lodève, St. Affrique), and contemporaneous detachment of the Espinouse Fault, which initiated Montagne Noire core complex exhumation (Fig. 19; Pochat and Van Den Driessche, 2011; Pitra et al., 2012).

As mentioned previously, a Pliocene-Miocene exhumation timing of the Montagne Noire dome was assumed prior to this work, but our findings require uplift and unroofing of the dome in the Early Permian. Framework mineralogy of fine-grained Upper Permian sandstone (Rabejac-Salagou) verifies the abundance of metamorphic lithic fragments and feldspar, which perhaps represent the fragmented form of clasts derived from the Montagne Noire Dome. P-T-t paths show that gneiss and migmatite in

the Axial Zone were uplifted higher and faster than surrounding schist and orthogneiss, and that the core was rising continuously during 340-316 Ma metamorphism and deformation (Costa and Maluski, 1988; Maluski et al., 1991; Matte et al., 1998; Soula et al., 2001). Peak metamorphic conditions in the gneissic core, and metamorphic ages from the La Salvetat migmatite indicate a 16.5-17.5 km depth of the core during most recent 298 ± 2 Ma migmatization (Maluski et al., 1991; Poujol et al., in review), assuming a thermal gradient of $\sim 40^\circ\text{C}/\text{km}$ (Thompson and Bard, 1982). Emplacement of the Montalet granite at 294 ± 3 Ma (Brun and Van Den Driessche, 1994; Poilvet et al., 2011) coincides with shearing and deformation of the St. Eutrope granite (295 ± 5 Ma) along the Espinouse Detachment (Fig. 16, 19; Pitra et al., 2012).

The maximum depositional ages (youngest populations) of detrital zircons sourced from the dome (App. E-9) require that erosion of the Montagne Noire core complex occurred by 295 Ma. Together with documented 298 ± 2 Ma migmatization of the core complex at ≥ 17 km depth (Maluski et al., 1991; Poilvet et al., 2011; Poujol et al., in review), this implies rapid (3.4-17 mm/year, within error) exhumation of the core to the surface from ca. 300-295 Ma. Contemporaneous detachment of the Espinouse fault controlled the exhumation of the dome along the footwall, and Graissessac-Lodève basin formation along the hanging wall (Fig. 19; Van Den Driessche and Brun, 1989; Pitra et al., 2012). Detrital zircon ages (330-285 Ma) in the Permian strata of the Lodève Basin demonstrate that dome exhumation persisted through the Permian.

Backstripping analysis of the Lodève Basin (Fig. 13) sheds additional light on the tectonic evolution, including the hypothesized rapid uplift of the Montagne Noire gneiss dome. The duration and rates of subsidence of the Lodève Basin are consistent

with extensional, rift basin subsidence (Allen and Allen, 2005; Xie and Heller, 2009); specifically, the initial rapid (≥ 312 m/My) subsidence during crustal extension and associated basin development ca. 300 Ma. Long-lived subsidence (avg. 70 m/My) persists throughout the Permian, and reflects the crustal response to the progressive exhumation of the proximal Montagne Noire dome, which also likely caused the tilted, half-graben geometry of the Lodève Basin (Fig. 2). In the Triassic (ca. 250 Ma), an abrupt transition occurs from tectonically driven subsidence, to more gradual post-rift thermal subsidence.

Chapter 6: Conclusions

Detrital zircon populations from Carboniferous-Permian strata of the Graissessac-Lodève basin in the southern Massif Central reveal evidence of localized tectonic events related to the Variscan Orogeny. Neither the tectonic nature, nor exhumation timing of the Montagne Noire dome has been previously constrained, but our results show that sandstone framework modes and detrital zircon ages in Permian strata of the Graissessac-Lodève basin are governed by the ages and compositions of units that make up the Montagne Noire gneiss dome (located adjacent to the south-southwest), thus signaling its exhumation and unroofing in the Early Permian. Provenance of the Graissessac-Lodève basin includes (1) Neoproterozoic- Early Cambrian zircon ages, strained or polycrystalline quartz, and abundant metamorphic lithic fragments derived from the prevalent recycling of the metasedimentary “Schistes X” which formerly covered the dome, (2) Ordovician zircon ages and feldspathic compositions sourced from granitic orthogneiss units within, and on the flanks of the core complex, and (3) Late Carboniferous- Early Permian (330-285 Ma) detrital zircon ages in the Permian section (Loiras, Rabejac, and Salagou formations) that are sourced from deep seated erosion of abundant, Late Variscan (ca. 320-294 Ma) granitoids in the axial zone of the Montagne Noire core complex. The youngest detrital zircon populations in the Permian formations of the Lodève Basin require uplift of the Montagne Noire Core Complex by ca. 295 Ma. Together with previously documented 298-295 Ma migmatization and magmatism at ~17 km depth in the gneissic dome core, and rapid tectonic subsidence that persisted simultaneously throughout Permian deposition in the Graissessac-Lodève basin, exhumation of the dome to the surface

occurred rapidly (3.4-17 mm/year) between ca. 300-295 Ma. Our results require rapid exhumation rates, and present a new hypothesis to be further constrained in future work.

Albiro, C.J., Ben Othman, B. 1989. *Les tectoniques mésozoïques et tertiaires de la région méditerranéenne: un développement tectonique à caractère orogénique.* *Annales de Géologie* 102.

Allen, P.A. and Allen, J.R. 1998. *Basin Analysis: Principles and Case Studies*. Blackwell Scientific Publications.

Allen, P.A. and Allen, J.R. 2005. *Basin Analysis: Principles and Case Studies*. Second edition. Blackwell Scientific Publications.

Arnaud, E., Dierckx, B., Sardin, M., S. Capdevin, A., Fernandez-Alonso, J., Allard, E. 2014. Two-stage collision: Exploring the birth of Pyrene in the Variscan orogen. *Geodynamic Research* 21: 754-763.

Arnaud, F. 1978. *Étude tectonique et microtectonique comparative de deux domaines tectoniques, les nappes de la Montagne Noire (France) et l'antiforme de l'Égérie (Algérie).* Thèse d'Etat, University of Montpellier: 173.

Arnaud, F., Matte, 1975. Les décrochements fault-déformés en cas-cas de Picapeau. Géométrie et mise de reconstitution des conditions de la déformation. *Tectonophysics* 23(1-2): 145-171.

Arnaud, J., Pons, M., Maréchal, G., Chen, Y. 2009. Gravity inversion, AMS and geochronological investigation of synorogenic growth phases in the western part of the Variscan French Massif Central. *Journal of Structural Geology* 31: 433-443.

Balera, M., Ferrada, S., Capdevin, P., Pons, J., Sardin, M., Serrano, C. M. 2012. Geochronology and geotectonics of the Variscan Massif: Implications to the French Antiform Massif (Variscan belt, France). *International Journal of Geology and Geophysics*. *Geodynamic Research* 21: 1045-1056.

Bast, J.P. 1978. *À propos du style tectonique de la zone des nappes occidentales de la zone méridionale de la Montagne Noire (Nappe d'Arnaud).* *Annales de Géologie des Sciences-Paris* 307: 1121-1123.

Bird, A., Jones, C.W., Mack, G.H., Suttie, J. 2007. *Using 3-D*. 1998. *Application of the use of virtual non-spherical quartz in geochronology and geotectonics*. *Geological Society of America Annual Meeting Abstracts and Programs* 173: 1023.

Bonnet, F. 1985. *Étude structurale de la zone tectonique orientale de la Montagne noire (sud du Massif central, France). Détermination des mécanismes de déformation tectonique avec les nappes de versants.* Thèse, Université des Sciences et Techniques de Languedoc.

References Cited

Allègre, C.J., Ben Othman, D. 1980. Nd-Sr isotopic relationship in granitoid rocks and continental crust development; a chemical approach to orogenesis. *Nature* 286: 335-342.

Allen, P.A. and Allen, J.R. 1990. *Basin Analysis, Principles and Applications*. Blackwell Scientific Publications.

Allen, P.A. and Allen, J.R. 2005. *Basin Analysis, Principles and Applications*. Second edition. Blackwell Scientific Publications.

Arenas, R., Díez Fernández, R., Sánchez Martínez, S., Gerdes, A., Fernández-Suárez, J., Albert, R. 2014. Two-stage collision: Exploring the birth of Pangea in the Variscan terranes. *Gondwana Research* 25: 756-763.

Arthaud, F. 1970. Étude tectonique et microtectonique comparée de deux domaines hercyniens; les nappes de la Montagne Noire (France) et l'anticlinorium de l'Iglesiente (Sardaigne). Thèse d'État, University of Montpellier: 175.

Arthaud, F., Matte. 1975. Les décrochements tardi-hercyniens du sud-ouest de l'Europe. Geometrie et essai de reconstitution des conditions de la deformation. *Tectonophysics* 25 (1-2) 145-171.

Aurore, J., Faure, M., Martelet, G., Chen, Y. 2009. Gravity inversion, AMS and geochronological investigations of syntectonic granitic plutons in the southern part of the Variscan French Massif Central. *Journal of Structural Geology* 31: 421-443.

Ballevre, M., Fourcade, S., Capdevila, R., Peucat, J., Cocherie, A., Fanning, C.M., 2012, Geochronology and geochemistry of the Ordovician felsic volcanism in the Southern Armorican Massif (Variscan belt, France). Implications for the breakup of Gondwana. *Gondwana Research* 21: 1019-1036

Bard, J.P. 1978. À propos du style tectonique de la phase hercynienne précoce de la zone axiale de la Montagne Noire (Massif Central). *Comptes Rendus de l'Academie des Sciences Paris* 287: 1321-1323.

Basu, A., James, C.W., Mack, G.H., Suttner L.J., Young, S.W. 1974. Re-evaluation of the use of strained monocrystalline quartz in provenance interpretation (abs.): Geological Society of America Annual Meeting, Abstracts and Programs 6 (7): 1021.

Beaud, F. 1985. Étude structurale de la zone axiale orientale de la Montagne noire (Sud du Massif central, France). Détermination des mécanismes de déformation, relation avec les nappes du versant sud. Thèse, Université des Sciences et Techniques du Languedoc.

Becq-Giraudon, J., Montenat, C., Van Den Driessche, J. 1996. Hercynian high-altitude phenomena in the French Massif Central: tectonic implications. *Paleogeography, Palaeoclimatology, Palaeoecology* 122: 227-241.

Becq-Giraudon, J.F., Van Den Driessche, J. 1994. Dépôts périglaciaires dans le Stéphano-Autunien du Massif Central: témoin de l'effondrement gravitaire d'un haut plateau hercynien. *Comptes Rendus de l'Académie des Sciences Paris* 318: 675-682.

Becq-Giraudon, J.F., Van Den Driessche, J. 1993. Continuity of sedimentation between the Stephanian and Permian within the Graissessac-Lodève basin (Southern French Massif Central); tectonic implications. *Comptes Rendus de l'Académie des Sciences, Series IIA* 317 (7): 939-945.

Blakey, R.C. 2007. Carboniferous-Permian palaeogeography of the Assembly of Pangea: Proceedings of the XVth International Congress on Carboniferous and Permian Stratigraphy: 443-456.

Blés, J.L., Bonijoly, D., Castaing C., Gros, Y. 1989. Successive post-Variscan stress fields in the French Massif Central and its borders (Western European plate): comparison with geodynamic data. *Tectonophysics* 169 (1-3): 79-11.

Bogdanoff, S., Cirodde, J.L., Donnot, M. 1984. Présence de grès à faciès Marcory dans la partie orientale de la Chataigneraie (Massif Central, Français). *Réunion Annu. Sci. Terre*, 10th (Bordeaux), Soc. Géol. Fr, Paris: 69.

Boulvain, F., Pingot, J.L. 2013. Une introduction à la Géologie de la Wallonie. Presentation at Université de Liège, Département de Géologie. Fig, III.15, III.24, III.25.

BRGM (Bureau de Recherches Géologiques et Minières). 1968. Carte Géologique de la France. Scale: 1:1,000,000 km.

BRGM (Bureau de Recherches Géologiques et Minières), Alabouvette, B., Arthaud, F., Aubague, M., Bambier, A., Brousse, R., Delher, G., Feist R., Medioni, R., Paloc, H., Petit, J.P., Ball, E., Plegat, R., Seguret, M., Marocco, R., and Rivier, F. 1982. Carte géologique France (1/50,000), feuille Lodève (989).

BRGM (Bureau de Recherches Géologiques et Minières), Bogdanoff, S., Donnot, M., Ellenberger, F. 1982. Carte géologique France (1/50,000), feuille Bedarieux (988). In: Crowell, J. 1999. Pre-Mesozoic ice ages; their bearing on understanding the climate system. *Memoirs Geological Society of America*: 192.

BRGM (Bureau de Recherches Géologiques et Minières), Bogdanoff, S., Donnot, M., Ellenberger, F. 1984. Notice explicative de la feuille Bedarieux au 1/50,000: Carte Géologique de la France: 105.

BRGM (Bureau de Recherches Géologiques et Minières). 2007. *Geologie de la France symposium; Mechanics of Variscan Orogeny, a modern view on orogenic research. Field trip guide (2): 5.*

Broutin, J., Chateauneuf, J. and Mathis, V. 1992. The Lodève Basin. In: *Permian Basins in the French Massif Central. 8th International Palynological Congress, Cahiers de Micropaléontologie (7): 107–122.*

Bruguier, O., Becq-Giraudon, J.F., Champenois, M., Deloule, E., Ludden, J., Mangin, D. 2003. Application of in situ zircon geochronology and accessory phase chemistry to constraining basin development during post-collisional extension: a case study from the French Massif Central. *Chemical Geology* 201: 319–336.

Brun, J.P., Van Den Driessche, J. 1994. Extensional gneiss domes and detachment fault systems; structure and kinematics. *Bull. Soc. géol. France* 165 (6): 519–530.

Burg, J. P., Matte, P. 1978. A Cross Section through the French Massif Central and the Scope of its Variscan Geodynamic Evolution. *Zeitschrift der Deutschen Geologischen Gesellschaft Band 129: 429-460.*

Burg, J.P., Bale, P., Brun, J.P., Girardeau, J. 1987. Stretching lineation and transport direction in the Ibero-Armorican arc during the Siluro-Devonian collision. *Geodinamica Acta* 1: 71-87.

Burg, J.P., Brun, J.P., Van Den Driessche, J. 1990. Le Sillon Houiller du Massif Central français: faille de transfert pendant l'amincissement crustal de la chaîne varisque? *Comptes Rendus de l'Académie des Sciences Paris: 147-152.*

Burg J.P., Van Den Driessche J., Brun J.P. 1994. Syn-to post-thickening extension in the Variscan Belt of Western Europe; modes and structural consequences. *Comptes Rendus de l'Académie des Sciences Paris* 319: 1019-1032.

Cardozo, N. 2013. OSXBackStrip Help, OSXBackstrip Program v. 3.2 (Dept, of Petroleum Engineering, University of Stavanger, Norway) nfcd@mac.com

Cocherie, A., Baudini, T., Autran, A., Guerrot, C., Fanning, M., Laumonier, B. 2005. U-Pb zircon (ID-TIMS and SHRIMP) evidence for the early Ordovician intrusion of metagranites in the late Proterozoic Canaveilles Group of the Pyrenees and the Montagne Noire (France). *Bull. Soc. géol. Fr.* 176 (3): 269-282.

Costa, S. 1992. East-West diachronism of the collisional stage in the French Massif Central: implications for the European Variscan orogen. *Geodinamica Acta* 5: 51-68.

Costa, S., Maluski, H. 1988. ⁴⁰Ar/³⁹Ar dating for terranes boundaries definition: The example of French Massif Central. IGCP project (233), International Conference, Montpellier (France) Abstracts: 17.

Debat, P. 1974. Essai sur la deformation des gneiss de la Montagne Noire occidentale. Thesis, University of Toulouse III.

Demange, M. 1975. Style pennique de la zone axiale de la Montagne Noire entre Saint-Pons et Murat-sur-Vèbre (Massif Central). Bull. BRGM 2: 91-139.

Demange, M. 1982. Etude geologique du Massif de l'Agout, Montagne Noire, France. Thesis, University of Paris VI.

Demange, M. 1985. The eclogite facies rocks of the Montagne Noire, France. *Chemical Geol.* 50: 173-188.

Demange, M. 1994. Antevvariscan evolution of Montagne Noire (France): from a passive margin to a foreland basin. *Comptes Rendus de l'Academie des Sciences, Series 2. Sciences de la terre et des planets* 318 (7): 921-933.

Dewey, J., Burke, K.C. 1973. Tibetan, Variscan and Precambrian basement reactivation: Products of continental collision. *Journal of Geology* 81: 683-692.

Dickinson, W.R. 1970. Interpreting detrital modes of graywacke and arkose. *Journal of Sedimentary Petrology* 40: 695-707.

Dickinson, W.R., Suczek, C.A. 1979. Plate tectonics and sandstone compositions. *American Association of Petroleum Geologists Bulletin* 63: 2164-2182.

Dickinson, W.R., Beard, L.S., Brakenridge, G.R., Erjavec, J.L., Ferguson, R.C., Inman, K.F., Knepp, R., Lindberg, F.A., Ryberg, P.T. 1983. Provenance of North American Phanerozoic sandstones in relation to tectonic setting. *Geological Society of America Bulletin* 94: 222-235.

Dickinson, W.R., Gehrels, G.E. 2008. Sediment delivery to the Cordilleran foreland basin: insights from U-Pb ages of detrital zircons in Upper Jurassic and Cretaceous strata of the Colorado Plateau. *American Journal of Science* 308: 1041-1082.

Dickinson, W.R., Gehrels, G.E. 2009. Use of U-Pb ages of detrital zircons to infer maximum depositional ages of strata: A test against a Colorado Plateau Mesozoic database. *Earth and Planetary Science Letters* 288: 115-125.

Didier, J., Lameyre J. 1971. Les roches granitiques du Massif central. In: *Symposium J. Jung: Géologie, géomorphologie et structure profonde du Massif Central Français*: 17-32.

Díez Fernández, R., Castiñeiras, P., Gómez Barreiro, J. 2012. Age constraints on Lower Paleozoic convection system: magmatic events in the NW Iberian Gondwana margin. *Gondwana Research* 21: 1066-1079.

Díez Fernández, R., Martínez Catalán, J.R., Arenas, R., Abati, J. 2012. The onset of the assembly of Pangaea in NW Iberia: constraints on the kinematics of continental subduction. *Gondwana Research* 22: 20-25.

Domeier, M., Van der Voo, R., Torsvik, T.H. 2012. Paleomagnetism and Pangea: The road to reconciliation. *Tectonophysics* 514-517: 14-43.

Ducrot, J., Lancelot, J.R., Reille, J.L. 1979. Datation en Montagne noire d'un témoin d'une phase majeure d'amincissement crustal caractéristique de l'Europe prévarisque, *Bull. Soc. Géologie France* 21 (4): 501-505.

Duthou, J.L., Chenevoy, M., Gay, M. 1994. Age Rb/Sr Dévonien moyen des migmatites à cordiérite du Lyonnais (Massif central français). *Comptes Rendus de l'Academie des Sciences Paris* 319: 791-796.

Echtler, H., Malavieille, J. 1990. Extensional tectonics, basement uplift and Stephanian-Permian collapse basin in a Late Variscan metamorphic core complex (Montagne Noire, Southern Massif Central). *Tectonophysics* 177: 125-138.

Engel, W., Feist, R., Franke, W., 1980. Le Carbonifère ante-stephanien de la Montagne Noire: rapports entre mise en place des nappes et sédimentation. *Bulletin B.R.G.M.* 2 (I-4): 341-389.

Faure, M. 1995. Late orogenic Carboniferous extensions in the Variscan French Massif Central. *Tectonics* 14: 132-153.

Faure, M., Cotterau, N. 1988. Données cinématiques sur la mise en place du dôme migmatitique carbonifère moyen de la zone axiale de la Montagne Noire (Massif Central, France). *Comptes Rendus de l'Academie des Sciences Paris* 307 (II): 1787-1794.

Faure, M., Frost, A.E., Lasne, E. 1990. Deformation ductile extensive d'âge namuro-westphalien dans le plateau d'Aigurande, Massif Central française. *Bulletin soc. Geologie Fr.* 8: 187-189.

Faure, M., Leloix, C., Roig, J.Y. 1997. L'évolution polycyclique de la chaîne hercynienne. *Bull. Soc. géol. Fr.* 168: 695-705.

Faure, M., Cocherie, A., Bé Mezeme, E., Charles, N., Rossi, P. 2010. Middle Carboniferous crustal melting in the Variscan Belt: new insights from U-Th-Pb monazite and U-Pb zircon ages of the Montagne Noire Axial Zone (southern French Massif Central). *Gondwana Research* 18: 653-673.

Femenias, O., Coussaert, N., Bingen, B., Whitehouse, M., Mercier, J.C., Demaiffe, D. 2003. A Permian underplating event in late- to post-orogenic tectonic setting: evidence

from the mafic-ultramafic layered xenoliths from Beaunit (French Massif Central). *Chemical Geology* 199: 293-315.

Fernandez-Suarez, J., Gutierrez-Alonso, G., Jenner, G.A., Tubrett, M.N. 2000. New ideas on the Proterozoic-early Palaeozoic evolution of NW Iberia; insights from U-Pb detrital zircon ages. *Precambrian Research* 102: 185–206.

Floc'h, J.P. 1983. La série métamorphique du Limousin central. Thèse d'État, Univ. Limoges, France: 445.

Gehrels, G.E. 2000. Introduction to detrital zircon studies of Paleozoic and Triassic strata in western Nevada and northern California. In: Soreghan, M.J., and Gehrels, G.E., (eds.) *Paleozoic and Triassic paleogeography and tectonics of western Nevada and northern California*. Geological Society of America Special Paper 347: 1-17.

Gehrels, G.E. 2010. Analysis Tools. Tucson, University of Arizona, Arizona LaserChron Center. <https://sites.google.com/a/laserchron.org/laserchron/>

Gehrels, G.E., Valencia, V.A., and Ruiz, J. 2008. Enhanced precision, accuracy, efficiency, and spatial resolution of U-Pb ages by LA-MC-ICPMS. *Geochemistry, Geophysics, Geosystems* 9: 115-150.

Gehrels, G.E., Blakey, R., Karlstrom, K.E., Timmons, J.M., Dickinson, B., Pecha, M. 2011. Detrital zircon U-Pb geochronology of Paleozoic strata in the Grand Canyon, AZ. *Lithosphere* 3 (3): 183-200.

Gehrels, G.E., Giesler, D., Pecha, M. 2012. Detrital zircon geochronology with $n = 1,000$. *Geological Society of America, Abstracts with Programs* 44 (7): 136.

Gèze, B. 1949. Étude géologique de la Montagne Noire et des Cévennes Méridionales. *Mem. Soc. Géol. Fr.* 24: 215.

Graham, S.A., Ingersoll, R.V., Dickinson, W.R. 1976. Common provenance for lithic Grains in Carboniferous sandstones from Ouachita Mountains and Black Warrior Basin. *Journal of Sedimentary Petrology* 46 (3): 620-632.

Guynn, J., Gehrels, G.E. 2010. Comparison of detrital zircon age distributions in the K-S test: Tucson, University of Arizona, Arizona LaserChron Center: 16.

Hegarty, K.A., Weissel, J.K., and Mutter, J.C. 1988. Subsidence history of Australia's southern margin; constraints on basin models. *American Association of Petroleum Geologists Bulletin* 72: 615 - 633.

Ingersoll, R.V., Bullard, T.F., Ford, R.L., Grimm, J.P., Pickle, J.D., Sares, S.W. 1984. The effect of grain size on detrital modes: a test of the Gazzi-Dickinson point-counting method. *Journal of Sedimentary Petrology* 54: 103–116.

Korner, F., Schneider, J.W., Hoernes, S., Gand, G., Kleeberg, R. 1999. Sedimentologie und Geochemie der Perm-Klastite des Lodève Beckens (S-Frankreich) Fazies, Klima, Genese, Mitteilungen der Gesellschaft der Geologie- und Bergbaustudenten in Österreich 43: 72-74.

Korner, F., Schneider, J.W., Hoernes, S., Gand, G., Kleeburg, R. 2003. Climate and continental sedimentation in the Permian of the Lodève Basin (southern France). Italian Journal of Geosciences spec. 2: 185-191.

Lardeaux, J.M., Ledru, P., Daniel, I., Duchène, S. 2001. The Variscan French Massif central: a new addition to the ultra-high pressure metamorphic "club": exhumation processes and geodynamic consequences. Tectonophysics 323: 143-167.

Ledru, P., Lardeaux J.M., Santallier D., Autran A., Quenardel J.M., Floc'h J-P., Lerouge G., Maillot N., Marchand J., Ploquin A. 1989. Où sont les nappes dans le Massif Central français? Bull. Soc. Géol. Fr 8: 605-618.

Ledru, P., Autran A., Santallier D. 1994. Lithostratigraphy of Variscan terranes in the French Massif Central. A basis for paleogeographical reconstruction. In: Pre-Mesozoic geology in France and related areas: 276-288

Ledru, P., Courrioux G., Dallain C., Lardeaux J.M., Montel J.M., Vanderhaeghe O., Vitel G. 2001. The Velay dome (French Massif Central): meltgeneration and granite emplacement during orogenic evolution. Tectonophysics 332: 207-237.

Lescuyer, J.L., Cocherie, A. 1992. Datation sur monozircons des métadacites de Sériès: arguments pour un âge protérozoïque terminal des schistes X de la Montagne Noire (Massif central français). Comptes Rendus de l'Academie des Sciences Paris 314 (10): 1071-1077.

Linnemann, U., Gerdes, A., Drost, K., Buschmann, B. 2007. The continuum between Cadomian orogenesis and opening of the Rheic Ocean: Constraints from LA-ICP-MS U-Pb zircon dating and analysis of plate-tectonic setting (Saxo-Thuringian zone, northeastern Bohemian Massif, Germany). In: Linnemann, U., Nance, R.D., Kraft, P., and Zulauf, G. (eds.) The evolution of the Rheic Ocean: From Avalonian-Cadomian active margin to Alleghenian-Variscan collision. Geological Society of America Special Paper 423: 61-96.

Lopez, M., Grand, G., Garric, J., Korner, F., Schneider, J. 2007. The playa environments of the Lodève Permian basin (Languedoc-France). Journal of Iberian Geology 34 (1): 29-56.

Ludwig, K.R. 2003. User's manual for Isoplot 3.00- A geochronological toolkit for Microsoft Excel: Berkeley, California, Berkeley Geochronology Center, Special Publication 4: 70.

- Malavieille, J., Guihot, P., Costa, S., Lardeaux, J.M., Gardien, V. 1990. Collapse of the thickened Variscan crust in the French Massif Central: Mont Pilat extensional shear zone and Saint-Étienne upper Carboniferous basin. *Tectonophysics* 177: 139-149.
- Malavieille, J. 1993. Late orogenic extension in mountain belts: insights from the Basin and Range and the late Paleozoic Variscan belt. *Tectonics* 12: 1115-1130.
- Maluski, H., Costa, S., Echler, H. 1991. Late Variscan tectonic evolution by thinning of an earlier thickened crust; an $^{40}\text{Ar}/^{39}\text{Ar}$ study of the Montagne Noire, southern Massif Central, France. *Lithosphere* 26: 287-304.
- Mattauer, M. 2004. Orthogneisses in the deepest levels of the Variscan belt are not a Precambrian basement but Ordovician granites: tectonic consequences. *Geoscience* 336: 487-489.
- Mattauer, M., Laurent, P., Matte, P. 1996. Plissements hercyniens synschisteux post-nappe et étirement subhorizontal dans le versant Sud de la Montagne Noire. *Comptes Rendus de l'Académie des Sciences Paris* 322: 309-315.
- Matte, P. 1986. La Chaîne varisque parmi les chaînes paléozoïques péri-atlantiques, modèle d'évolution et position des grands blocs continentaux au Permo-Carbonifère, *Bull. Soc. Geol. France*, 8: 4-24.
- Matte, P. 1991. Accretionary history and crustal evolution of the Variscan belt in western Europe. *Tectonophysics* 196: 309-337.
- Matte, P. 2001. The Variscan collage and orogeny (480-290 Ma) and the tectonic definition of the Armorica microplate: a review. *Terra Nova* 13: 122-1128.
- Matte, P. 2002. Variscides between the Appalachians and the Urals: Similarities and differences between Paleozoic subduction and collision belts. In: Martinez Catalan, J. R., Hatcher, R. D., Arenas, R., and Diaz Garcia, F. (eds.) *Variscan-Appalachian dynamics: the building of the late Paleozoic basement*. Geological Society of America Special Paper 364: 239-251.
- Matte, P., Lancelot, J.R., Mattauer, M. 1998. La zone axiale hercynienne de la Montagne Noire n'est pas un metamorphic core complex extensif mais un anticlinal post-nappe à cour anatectique. *Geodinamica Acta* 11: 13-22.
- McCann, T., Pascal, C., Timmerman, M.J., Krzywiec, P. 2006. Post-Variscan (end Carboniferous-Early Permian) basin evolution in Western and Central Europe. Geological Society of London, *Memoir*: 1-34.
- Melleton, J., Cocherie, A., Faure, M., Rossi, P. 2010. Precambrian protoliths and early Paleozoic magmatism in the French Massif Central: U-Pb data and the northern

Gondwana connection in the west European Variscan belt. *Gondwana Research* 17: 13-25.

Menard, G., Molnar, P. 1988. Collapse of a Hercynian Tibetan Plateau into a late Palaeozoic European Basin and Range province. *Nature* 334: 235-237.

Montero, P., Bea, F., Gonzales-Lodeiro, F., Talavera, C.M., Whitehouse, J. 2007. Zircon ages of the metavolcanic rocks and metagranites of the Ollo de Sapo Domain in central Spain: Implications for the Neoproterozoic to Early Paleozoic evolution of Iberia. *Geological Magazine* 144: 963-976.

Mougeot, R., Respaut, J.P., Ledru, P., Marignac, C. 1997. U-Pb chronology on accessory minerals of the Velay anatectic dome (French Massif Central). *Eur. J. Mineral* 9: 141-156.

Murphy, J.B., Nance, R.D. 2008. The Pangea conundrum. *Geology* 36: 703-706.

Murphy, J.B., Pisarevsky, S.A., Nance, R.D., Keppie, J.D. 2004. Neoproterozoic- Early Paleozoic evolution of Peri-Gondwanan terranes: Implications for Laurentia- Gondwana connections. *International Journal of Earth Sciences* 93: 659-682.

Nicolas, A., Bouchez, J.L., Blaise, J., Poirier, J.P. 1977. Geological aspects of deformation in continental shear zones. *Tectonophysics* 42: 55-73.

Odin, B. 1986. Les formations permienes, Autunien supérieur à Thuringienne, du Bassin de Lodève (Hérault, France). Thèse, Université Aix-Marseille III: 392.

Odin, B., Doubinger, J., Conrad, G. 1987. Attribution des formations detritiques, rouges, du Permien du Sud de la France au Thuringien, d'après l'étude du bassin de Lodève; implications géologiques, paléontologiques et paléoclimatiques. *Comptes Rendus de l'Académie des Sciences Paris* 302 (16): 1015-1020.

Pin, C. 1990. Variscan oceans: ages, origins and geodynamic implications inferred from geochemical and radiometric data. *Tectonophysics* 177: 215-227.

Pin, C., Dupuy, C., Peterlongo, J.M. 1982. Répartition des terres rares dans les roches volcaniques basiques dévono-dinantiennes du nord-est du Massif central. *Bull. Soc. Géol. France* 7: 669-676.

Pin, C., Lancelot J. 1982. U-Pb dating of an early paleozoic bimodal magmatism in the French Massif Central and of its further metamorphic evolution. *Contrib. Mineral Petrol.* 79: 1-12.

Pin, C., Marini F. 1993. Early Ordovician continental break-up in Variscan Europe: Nd-SR isotope and trace element evidence for bimodal igneous associations of the southern Massif Central, France. *Lithosphere* 29: 177-196.

- Pin, C., Paquette J.L. 1998. A mantle-derived bimodal suite in the Hercynian Belt: Nd isotope and trace element evidence for a subduction-related rift origin of the Late Devonian Brévenne metavolcanics, Massif Central (France). *Contrib. Mineral. Petrol.* 129: 222-238.
- Pitra, P., Poujol, M., Van Den Driessche, J., Poulvet, J.C., Paquette, J.L. 2012. Early Permian extensional shearing of an Ordovician granite: The Saint-Eutrope "C/S-like" orthogneiss (Montagne Noire, French Massif Central). *Geoscience* 344: 377-384.
- Pochat, S., Van Den Driessche, J., Mouton, V., Guillocheau, F. 2005. Identification of Permian palaeowind direction from wave-dominated lacustrine sediments (Lodève Basin, France). *Sedimentology* 52: 809-825.
- Pochat, S., Van Den Driessche, J. 2011. Filling sequence in Late Paleozoic continental basins: A chimera of climate change? A new light shed given by the Graissessac-Lodève basin (SE France). *Palaeogeography, Palaeoclimatology, Palaeoecology* 302: 170-186.
- Poilvet, J.C., Poujol, M., Pitra, P., Van Den Driessche, J., Paquette, J.L. 2011. The Montalet granite, Montagne Noire, France: an Early Permian syn-extensional pluton as evidenced by new U-Th-Pb data on zircon and monazite. *C. R. Geoscience* 343: 454-461.
- Poujol, M., Pitra, P., Van Den Driessche, J., Ruffet G., Paquette J.L., Poilvet, J.C. In review. Two-stage monazite growth during the Variscan extensional tectonics (Montagne Noire, France). *International Journal of Earth Sciences*.
- Press, W.H., Flannery, B.P., Teukolsky, S.A., Vetterling, W.T. 1986. *Numerical Recipes in C, The Art of Scientific Computing*: Cambridge, UK, Cambridge University Press 186: 472-474.
- Quénardel, J.M., Rolin, P. 1984. Paleozoic evolution of the Plateau d'Aigurande (NW Massif Central, France). In: Hutton, D., Sanderson, D., *Variscan tectonics of the North Atlantic region* (eds.). Geological Society of London, Special publications 14: 63-77.
- Raymond, D., unpublished. Presentation at Maître de conférences honoraire, l'Université Pierre et Marie Curie (Paris VI). Société Amicale des Géologues Amateurs. Muséum National d'Histoire Naturelle.
- Reille, J.L. 1978. Mise en évidence des formations hypovolcaniques alcalines cambriennes parmi les orthogneiss hercyniens de la Zone Axiale de la Montagne Noire, d'après l'étude des populations de zircons. *Comptes Rendus de l'Académie des Sciences Paris*: 579-582.
- Roger, F., Respaut, J.P., Brunel, M., Matte, P., Paquette, J.L. 2004. U-Pb dating of Augén orthogneisses from the Axial Zone of the Montagne Noire (southern Massif

Central): new witness of Ordovician magmatism into the Variscan Belt. *C. R. Geoscience* 336: 19–28.

Roig, J.Y., Faure, M. 2000. La tectonique cisailante polyphasée du Sud-Limousin (Massif central français) et son interprétation dans un modèle d'évolution polycyclique de la chaîne hercynienne. *Bull. Soc. Géol. Fr.* 171: 295-307.

Roscher, M., Schneider, J. 2006. Permo-Carboniferous climate: Early Pennsylvanian to Late Permian climate development of central Europe in a regional and global context: Non-marine Permian Biostratigraphy and Biochronology. *Geology Society of London, Special Publication* 265: 95-136.

Santouil, G., 1980, Tectonique et microtectonique comparée de la distension permienne et de l'évolution post-triassique dans les bassins de Lodève, Saint-Affrique et Rodez (France SE). Mémoire Thèse, 3e Cycle Montpellier: 77.

Satkoski, A.M., Wilkinson, B.H., Hietpas, J., Samson, S.D. 2014. Likeness among detrital zircon population: An approach to the comparison of age frequency data in time and space. *GSA Bulletin* 125 (11-12): 1783-1799.

Schneider, J.W., Korner, F., Roscher, M., Kroner, U. 2006. Permian climate development in the northern peri-Tethys area- the Lodève basin, French Massif Central. *Palaeogeography, Palaeoclimatology, Palaeoecology* 40: 161-183.

Soula, J.C., Debat, P., Brusset, S., Bessière, G., Christophoul, F., Déramond, J. 2001. Thrust related, diapiric and extensional doming in a frontal orogenic wedge: example of the Montagne Noire, southern French Hercynian Belt. *Journal of Structural Geology* 23: 1677-1699.

Stampfli, G.M., Mosar, J., Favre, P., Pillecuit, A., Vannay, J.C. 2001. Permo-Mesozoic evolution of the western Tethyan realm: the Neotethys/East-Mediterranean connection. In: Ziegler, P.A., Cavazza, W., Robertson, A.H., Crasquin-Soleau, S. (eds) *PeriTethys Memoir 6: Peritethyan Rift/Wrench Basins and Passive Margins*. *Memoires du Museum National d'Histoire Naturelle*: 51–108.

Suttner, L.J. 1974. Sedimentary petrographic provinces: an evaluation. In: Ross, C.A., *Paleogeographic provinces and provinciality* (eds.) *Society of Economic Paleontologists and Mineralogists Special Publications* 21: 7544.

Thompson, P.H., Bard, J.P. 1982. Isograds and mineral assemblages in the eastern axial zone, Montagne Noire (France): implications for temperature gradients and P-T history. *Canadian Journal of Earth Sciences* 19 (1): 129-143.

Van Den Driessche J., Brun J.P. 1992. Tectonic evolution of the Montagne Noire (French Massif Central): a model of extensional gneiss dome. *Geodinamica Acta* 5: 85-99.

Van Den Driessche, J., Brun, J.P. 1989. Un modèle cinématique de l'extension paléozoïque supérieure dans le sud du Massif Central. *Comptes Rendus de l'Académie des Sciences Paris* 309: 1607–1613.

Van Der Plas, L. Tobi, A.C. 1965. A chart for judging the reliability of point counting results. *American Journal of Science* 263: 87-90.

Van Hinte, J.E. 1978. Geohistory analysis: Application of micropaleontology in exploration geology. *American Association of Petroleum Geologists Bulletin* 62: 201–222.

Vermeesch, P. 2012. On the visualization of detrital age distributions. *Chemical Geology* 312–313: 190-194.

Watts, A.B. 2001. *Isostasy and Flexure of the Lithosphere*. Cambridge University Press.

Xie, X., Heller, P. 2009. Plate tectonics and basin subsidence history. *Geological Society of America Bulletin* 121: 55–64.

Ziegler, P.A. 1982. Faulting and graben formation in western and central Europe. *Philosophical Transactions of the Royal Society of London* 305: 113–143.

Ziegler, P.A. 1988. Evolution of the Arctic-North Atlantic and the Western Tethys: *American Association of Petroleum Geologists Memoir* 43: 198.

Ziegler, P.A. 1990. *Geological Atlas of Western and Central Europe*, 2nd ed. Shell International Petroleum Maatschappij BV: 239.

Ziegler, P.A. 1996. Geodynamic processes govern development of rifted basins. In: Roure, F., Ellouz, N., Shien, V.S., Skvortsov, L. (eds) *Geodynamic Evolution of Sedimentary Basins*, Technip, Paris:19-67.

Ziegler, A.M., Scotese, C.R., McKerrow, W.S., Johnson, M.E., Bambach, R.K. 1979. Paleozoic Paleogeography *Ann. Rev. Earth Planet Sci.* 7: 473-502.

Ziegler, P.A., Dezes, P. 2006. *Crustal Evolution of Western and Central Europe*. Memoir of the Geological Society, London.

Appendix A: Figures



Figure 1. Stippled structural map of Western Europe depicting the Variscan orogenic belt. The French Massif central is the product of the Variscan Variscan orogenic belt, which is a Devonian-Carboniferous tectonic orogenic belt (see, e.g., Molnar et al., 1986). Upper panel: Present-day outline of the Variscan belt in Western Europe, including the northern Variscan foreland (pink), Variscan Massif (yellow), Bohemian Massif (blue), North Pyrenean orogenic belt (green), and the Apennine tectonic orogenic belt (Ammann Massif, AM, Central Massif, CM, and Bohemian Massif) (grey). Modified from Raymond (unpublished). Lower panel: Stippled north-south cross-section through the Variscan field (A-A') in present-day France. Proterozoic low-grade basement (grey), Paleozoic sediments (white), and Variscan (dark grey). Modified from Molnar (1982).

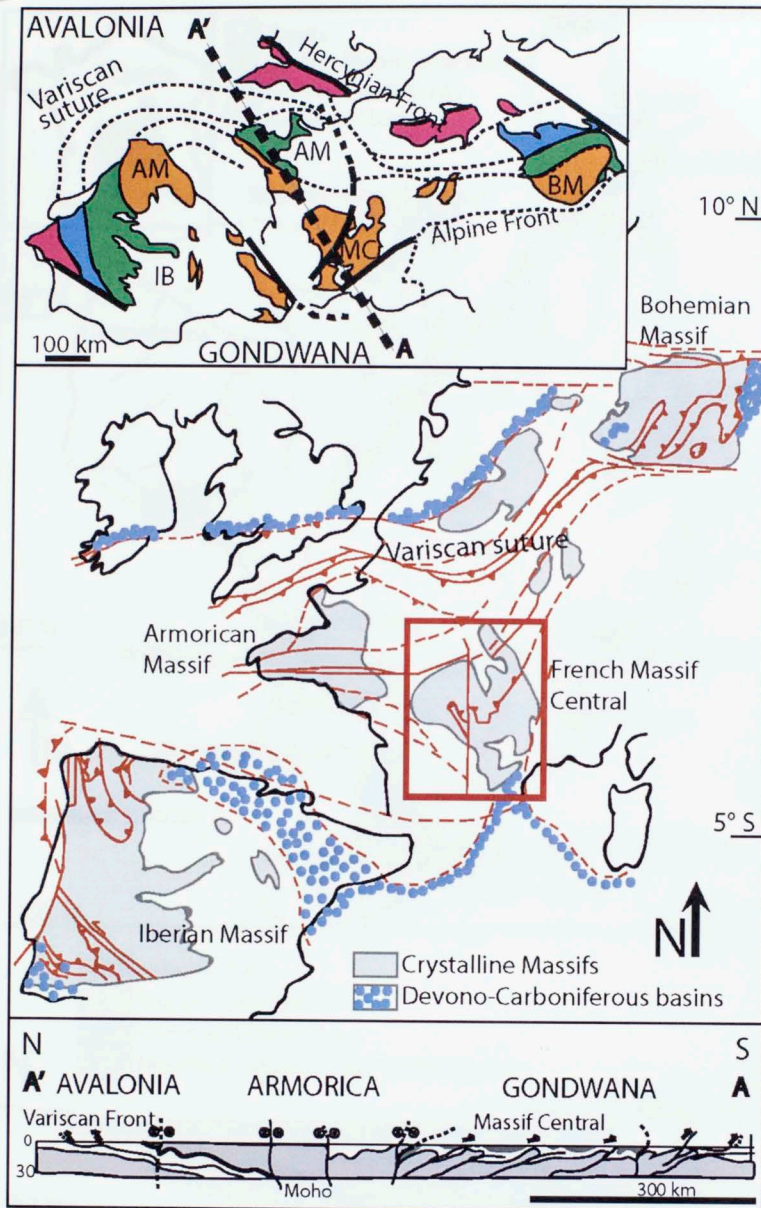


Figure 1. Simplified structural map of Western Europe displaying the location of the French Massif central in the context of the European Variscides, and distribution of Devonian-Carboniferous basins. Modified from Bruguier et al. (2003) and Matte (1986). *Upper inset:* Present-day relics of the Variscan Belt in Western Europe including the northern Variscan foreland (pink), intermediate blocks (Leon, N. Bohemia-BM, Ossa-Morena) (blue), Northern Gondwana margin (orange), and the Armorican terrane assemblage (Armorican Massif-AM, Central Iberia-IB, Central Bohemia-BM) (green). Modified from Raymond (unpublished). *Lower inset:* Schematic north-south cross section through the Variscan Belt (A-A' in inset) showing Late Proterozoic low-grade basement (gray), Paleozoic sediments (white), and ophiolites (dark gray). Modified from Matte (2002).

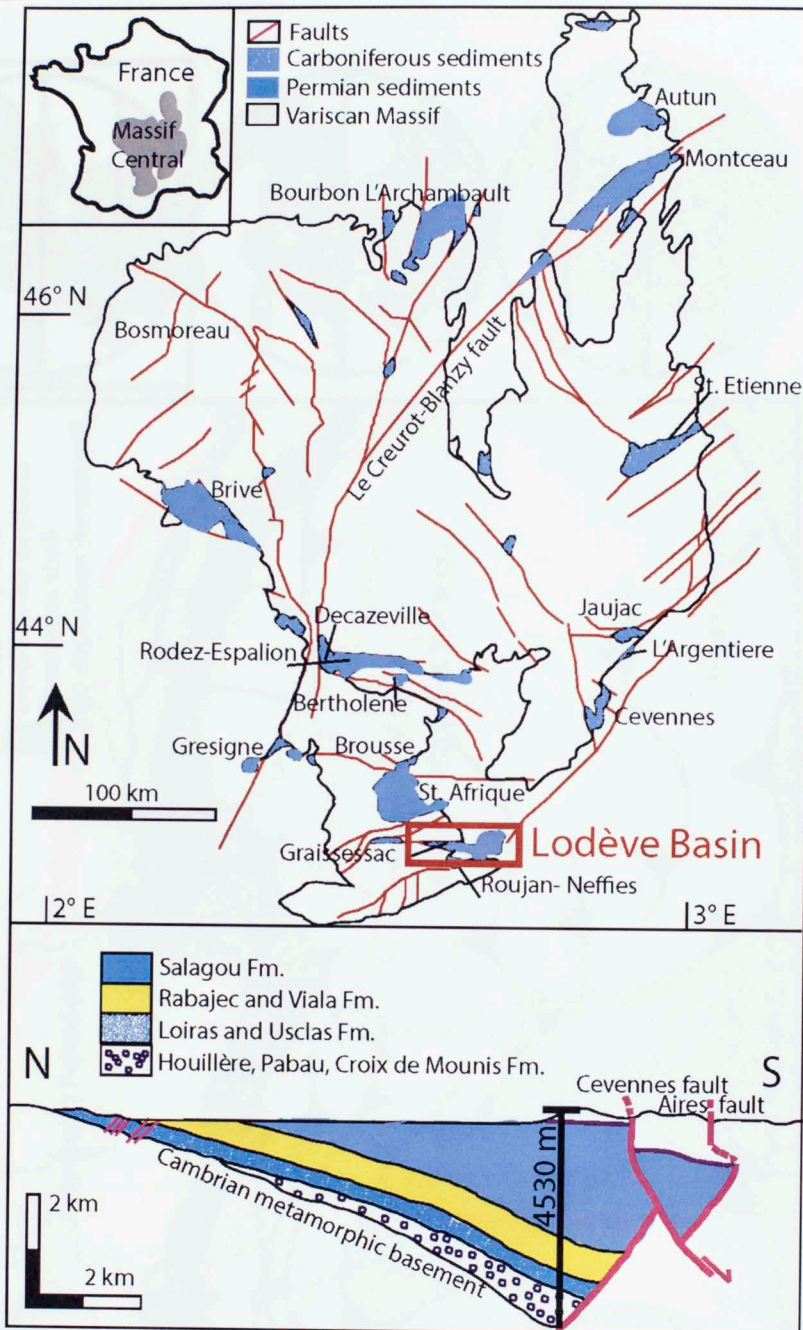


Figure 2. *Top:* Structural map of the Massif Central showing locations of Permo-Carboniferous basins (modified from Femenias et al., 2003). Red box denotes the location of the Graissessac-Lodève Basin. *Bottom:* Schematic north-south cross-section through the Lodève Basin. The Aires Fault (Espinouse Detachment) controls the half graben geometry (beds dip 5° - 20° S), and sediments onlap onto Cambrian marble-gneiss to the north. Modified from Pochat et al. (2005). Black bar represents the present-day reconstructed thicknesses (maximum thickness of the entire Permo-Carboniferous section) used for backstripping analyses; 4530 m total (from Pochat et al., 2005).

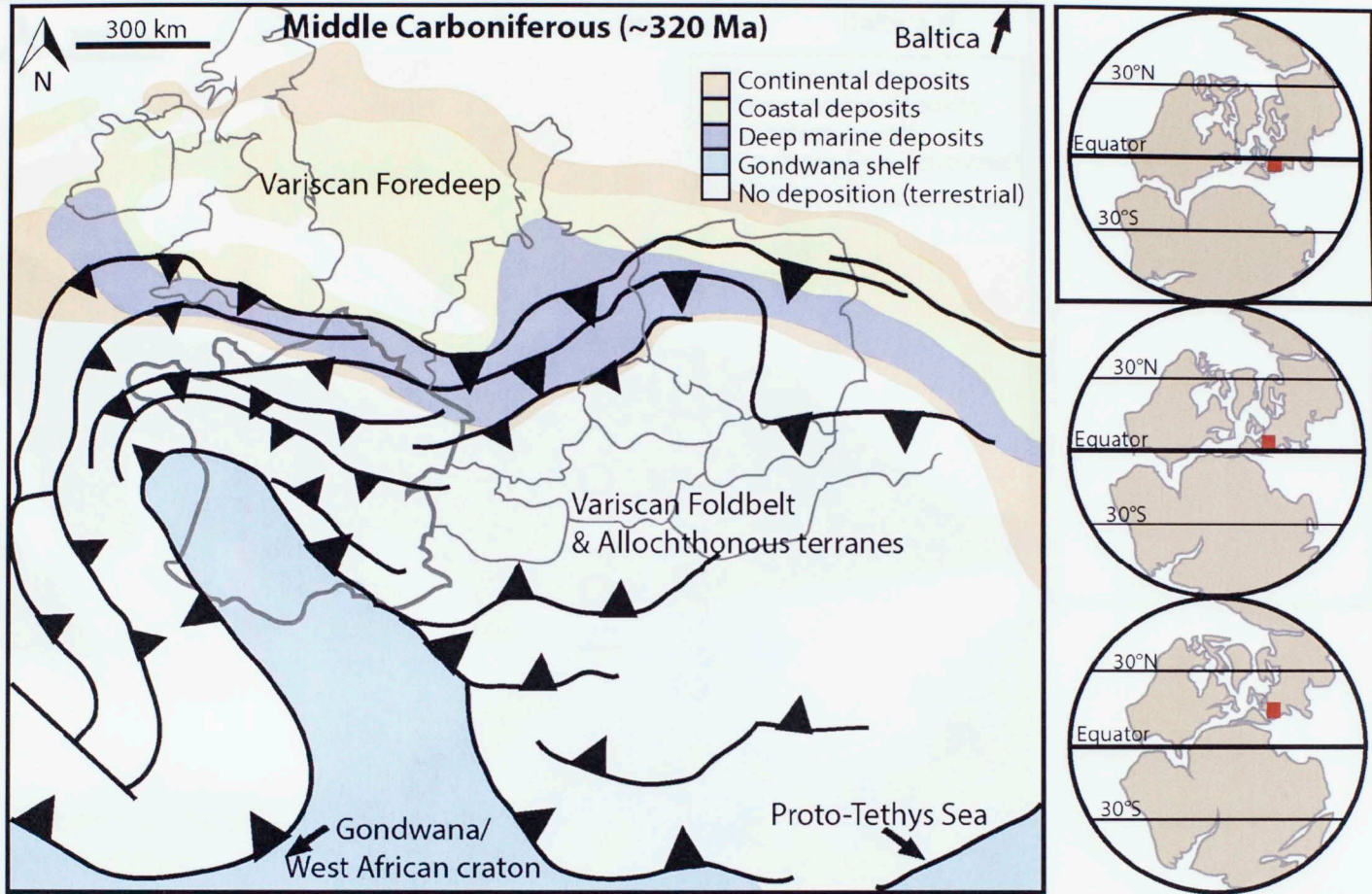


Figure 3A. Full caption on page 56.

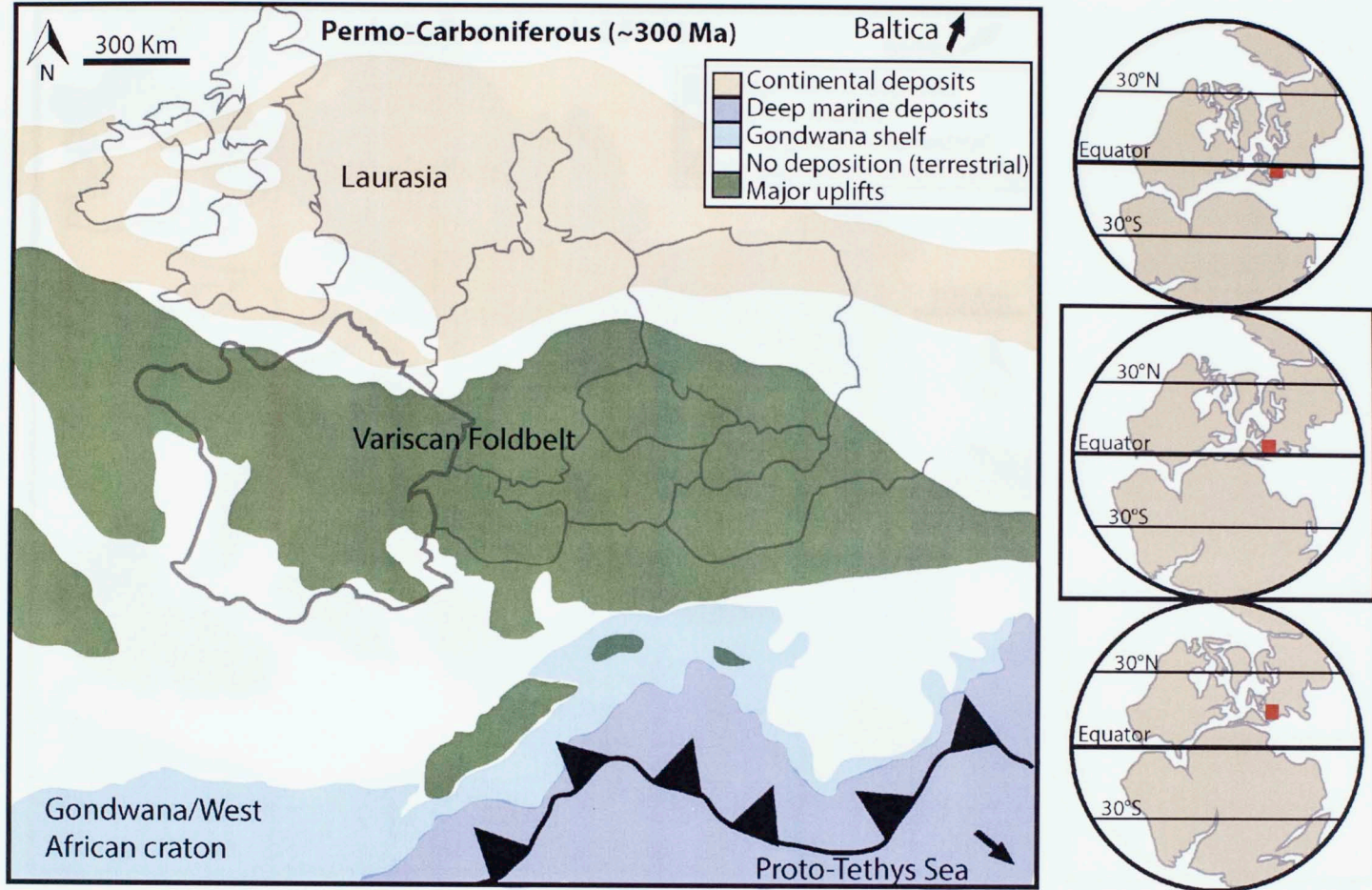


Figure 4B. Full caption on page 56.

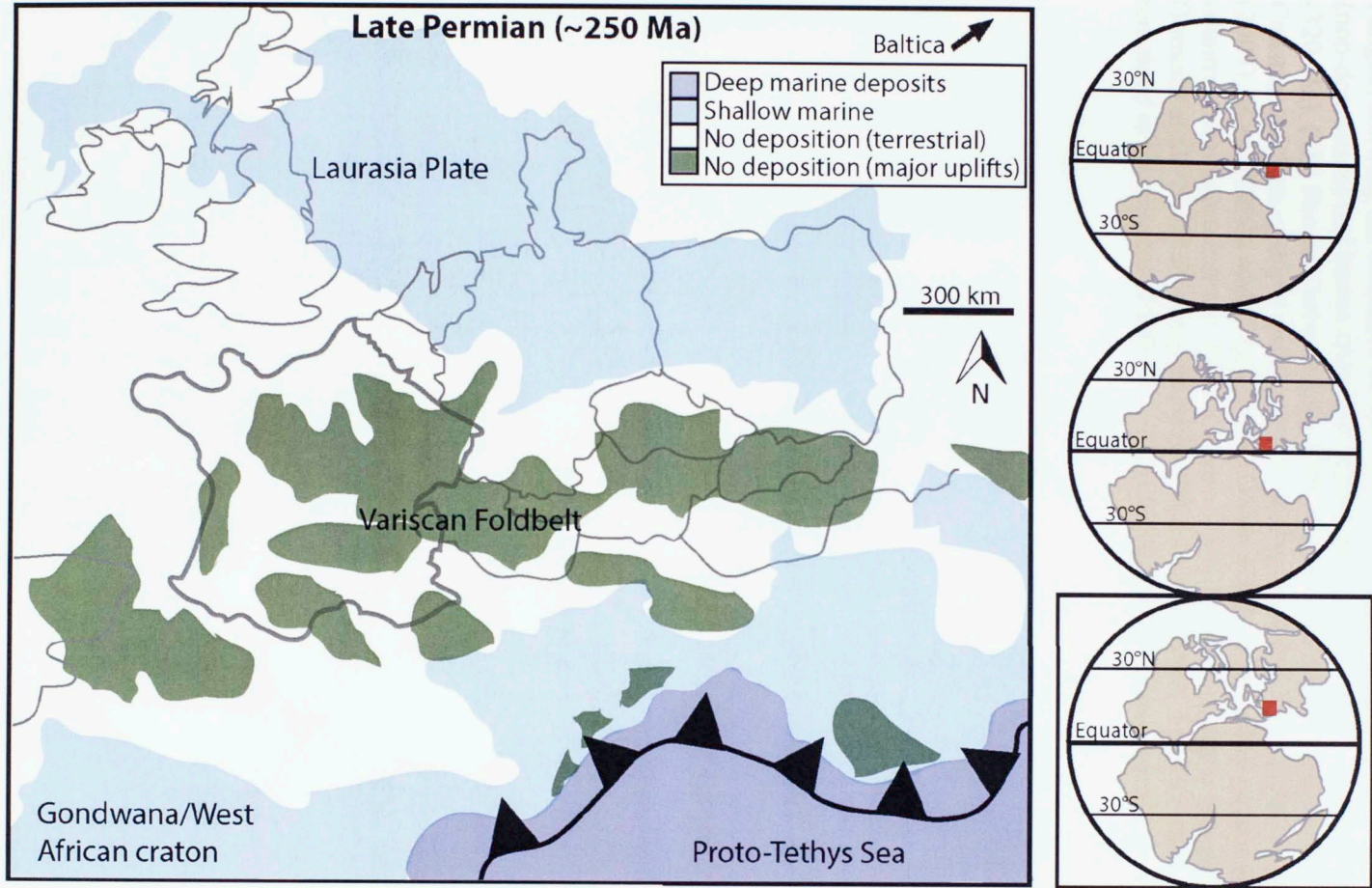


Figure 5C. Full caption on page 56.

Figure 3. Paleogeographic reconstructions of Western Europe (low-latitude eastern Pangea) showing the evolution of the Variscan Foldbelt, with generalized areas of uplift (non-deposition) and basins (possible depo-centers) in the: **(3A)** Middle Carboniferous (320 Ma), **(3B)** Permo-Carboniferous (300 Ma) and **(3C)** Late Permian (250 Ma). Constructed from multiple sources including Boulvain and Pingot (2013), Blakey (2007), Matte (2002), and Ziegler (1982, 1988, 1990, 2006). Gray outline represents countries of modern Europe. *Right column:* Global paleogeography (modified from Domeier et al., 2012) showing position of the Lodève Basin, France (red box), which remained in the equatorial belt (0° - 10° N) throughout the Late Paleozoic.



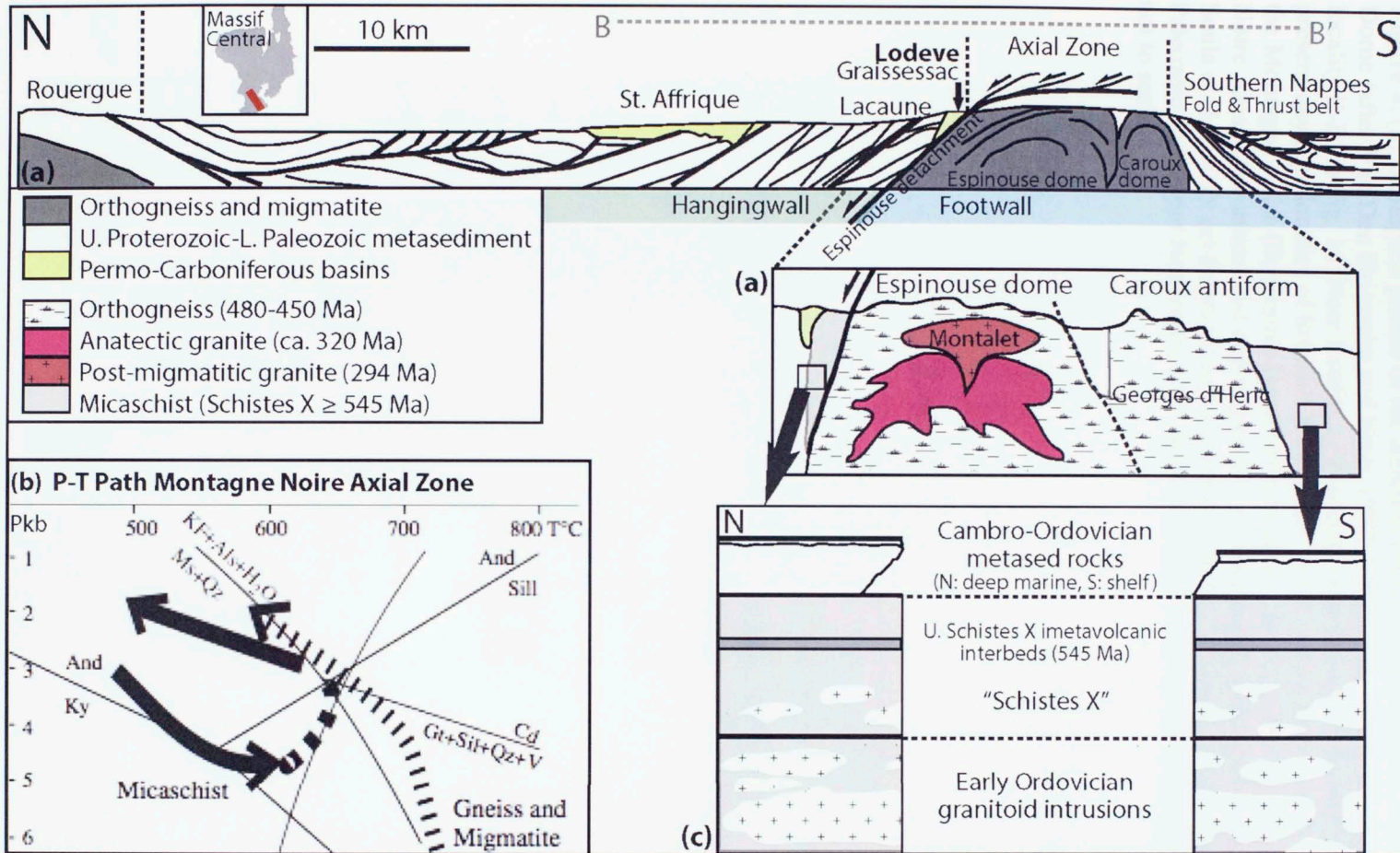


Figure 4. See caption on following page.

Figure 4. (a) Geological profile of the southern French Massif Central, Montagne Noire Dome (after Van Den Driessche and Brun, 1992; Soula et al., 2001). Cross section locality B-B' in Fig. 16. Note locality of Espinose Detachment. Mont-de-Lacaune is the present-day type locality of Schistes X exposure. *Inset:* shows more detailed profile of the Montagne Noire (Espinouse Dome) components. (b) P-T paths for the Montagne Noire Axial Zone micaschist and migmatitic gneiss (modified from Demange, 1985; Soula et al., 2001). (c) Representative lithologies of the Montagne Noire area (Lower Paleozoic and Upper Neoproterozoic) from Soula et al. (2001). Note that diagram (c) is not to scale.

Figure 4. (a) Geological profile of the southern French Massif Central, Montagne Noire Dome (after Van Den Driessche and Brun, 1992; Soula et al., 2001). Cross section locality B-B' in Fig. 16. Note locality of Espinose Detachment. Mont-de-Lacaune is the present-day type locality of Schistes X exposure. *Inset:* shows more detailed profile of the Montagne Noire (Espinouse Dome) components. (b) P-T paths for the Montagne Noire Axial Zone micaschist and migmatitic gneiss (modified from Demange, 1985; Soula et al., 2001). (c) Representative lithologies of the Montagne Noire area (Lower Paleozoic and Upper Neoproterozoic) from Soula et al. (2001). Note that diagram (c) is not to scale.

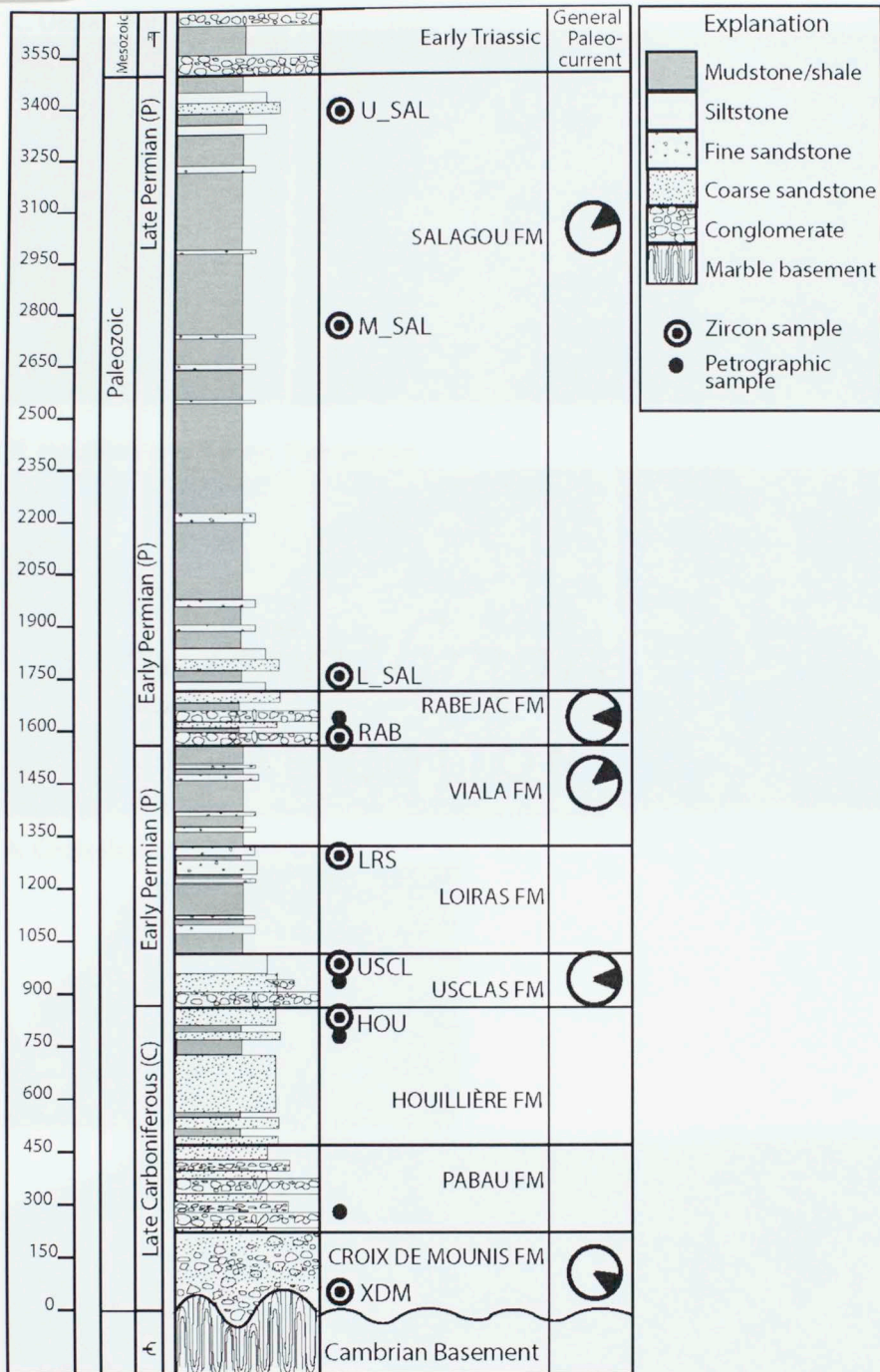


Figure 5. Simplified stratigraphic column of Permian-Carboniferous formations in the Graissessac-Lodève Basin, south central France (Adapted from Schneider et al., 2006; Pochat and Van Den Driessche, 2011) with sampled intervals. *Right column:* Rose diagrams represent paleocurrent data (based on cross-bedding and ripple measurements, lateral changes in formation thickness, and clast size reported in Pochat et al., 2005). Note that all fluvial paleoflow is directed to the E-NE (sourced from W-SW).

C. Usclas Formation



B. Houillère and Pabau Formations



A. Croix de Mounis Formation

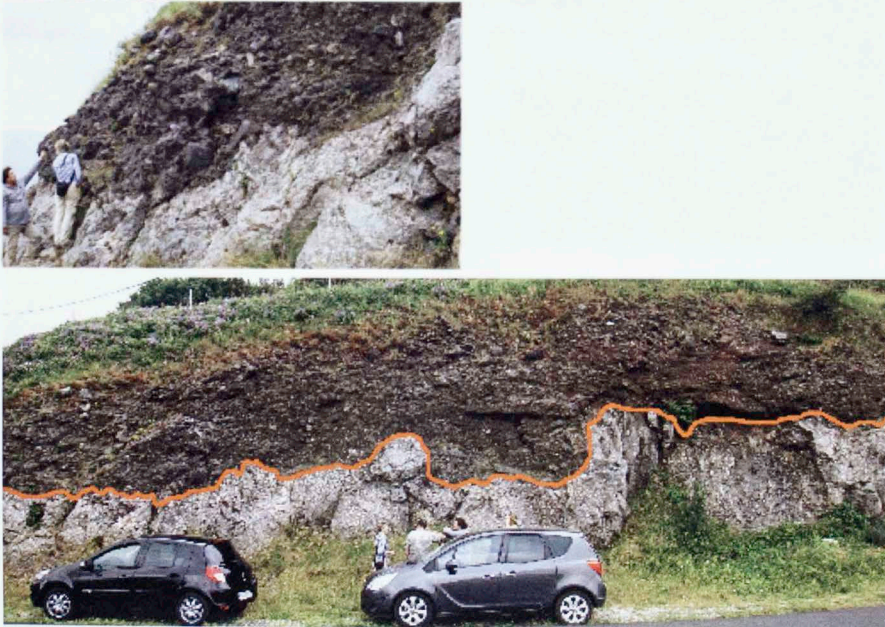


Figure 6. Representative photos of sampled and studied formations (Upper Carboniferous Croix de Mounis-Early Permian Usclas Formation). See text (Ch. 2) for detailed lithological descriptions.

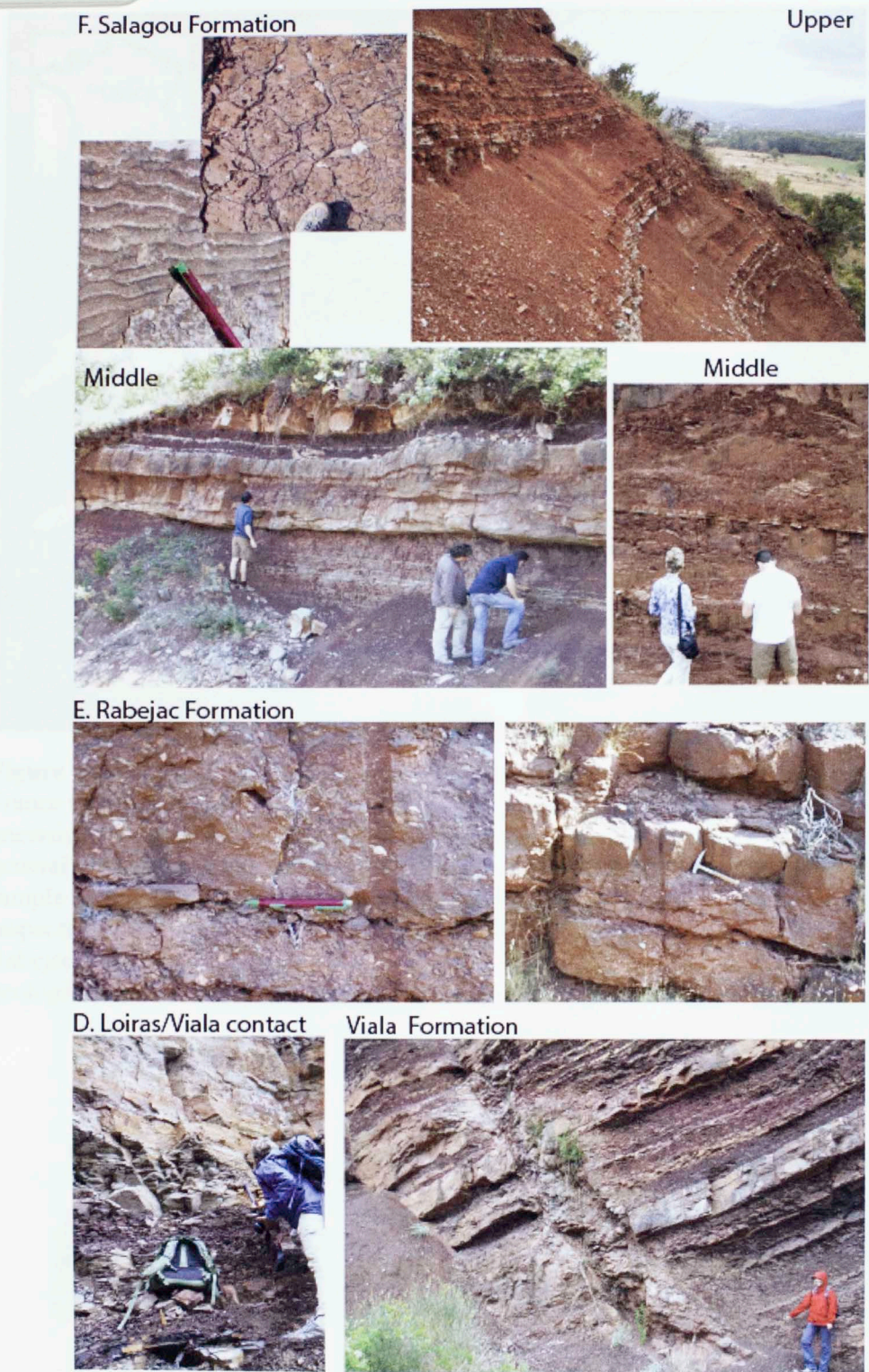


Figure 6. Representative photos of sampled and studied formations. See text (Ch. 2) for detailed lithological descriptions.

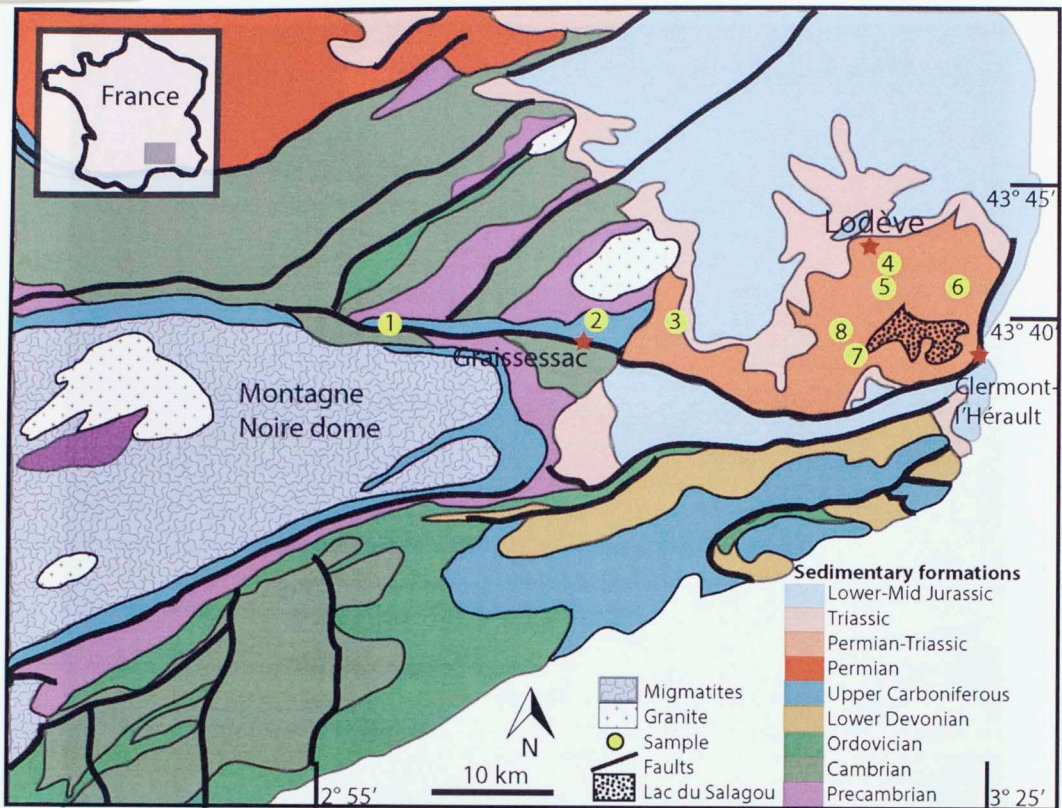


Figure 7. Simplified geologic map of the Lodève and Bédarieux regions in southern France showing the location of the Graissessac-Lodève basin, the Montagne Noire gneissic dome, and the modern Lac du Salagou. All faults (black lines) are normal, and generally dip away from the Montagne Noire core complex. Sites of detrital zircon sample collection are shown with yellow circles and numbered #1-8 (corresponding to respective formations: 1. Croix de Mounis, 2. Houillère, 3. Usclas, 4. Loiras, 5. Rabejac, 6. Lower Salagou, 7. Middle Salagou, 8. Upper Salagou). Drafted from geologic maps of southern France (BRGM, 1968) at a scale of 1:1,000,000 km.

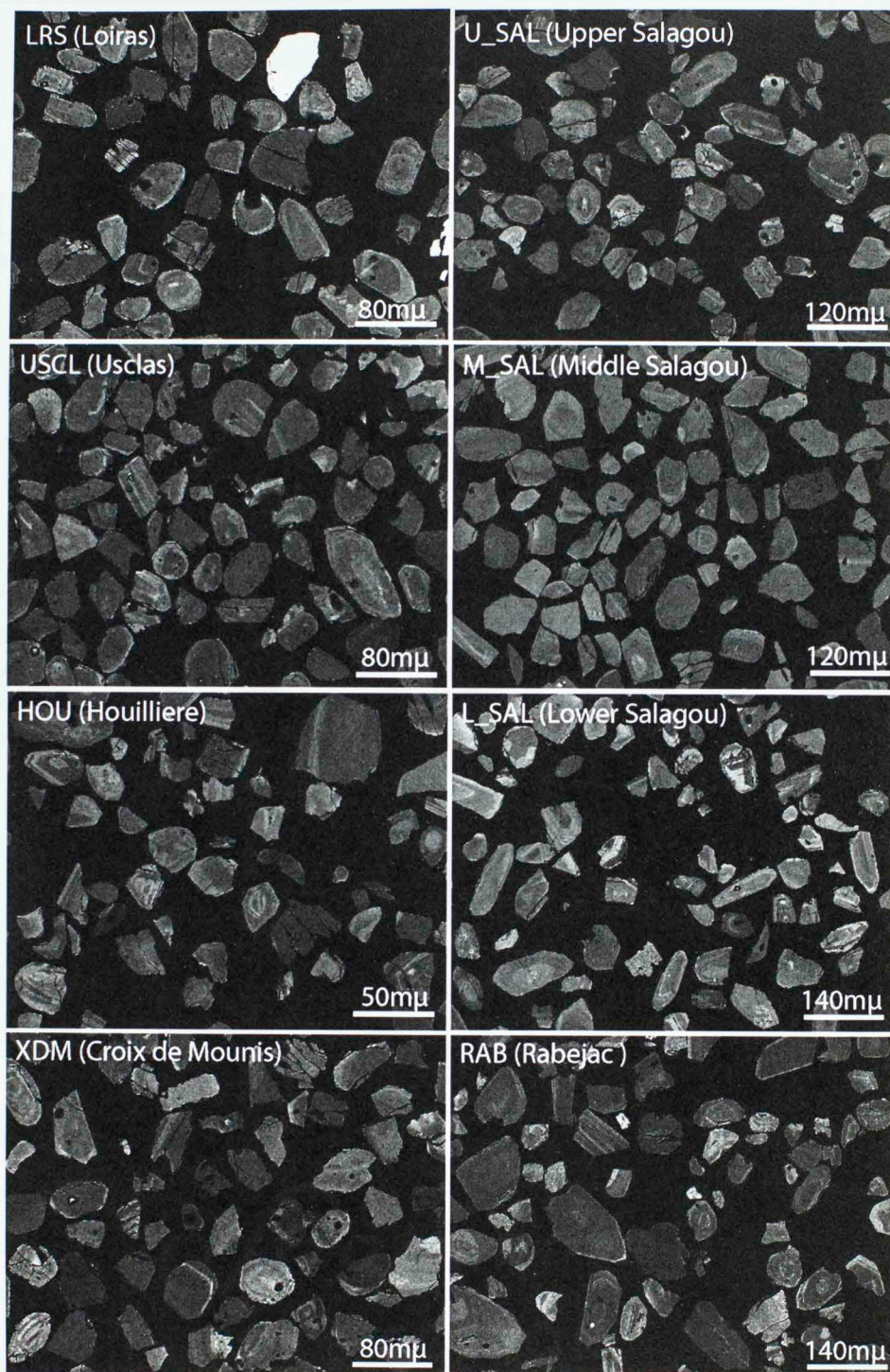


Figure 8. Backscattered electron (BSE) images of all detrital samples analyzed, showing representative zircon sizes, morphologies, and grain complexities. Zircons appear light gray-white, owing to their high atomic number (HREE). Note different scale bars in each image. See App. E-2 for a summary of zircon grain descriptions.

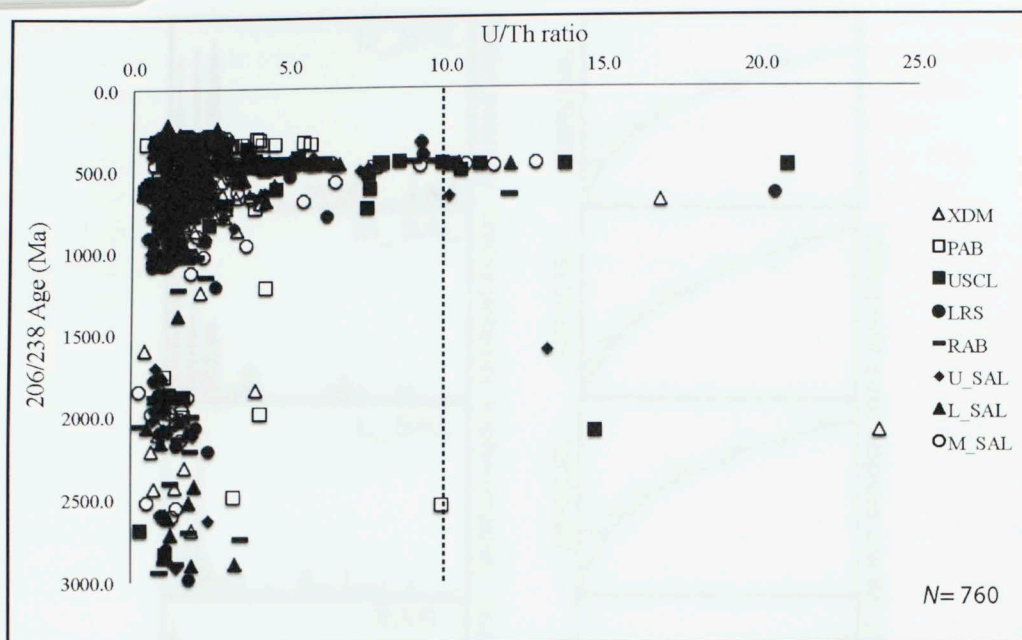


Figure 9. U/Th vs. Pb^{206}/U^{238} ages from spot analyses of 760 total detrital zircon grains from eight samples (each shape represents grains from respective sample: see legend). 97% of zircons have U/Th ratios <10, consistent with an igneous origin (Gehrels, 2011).

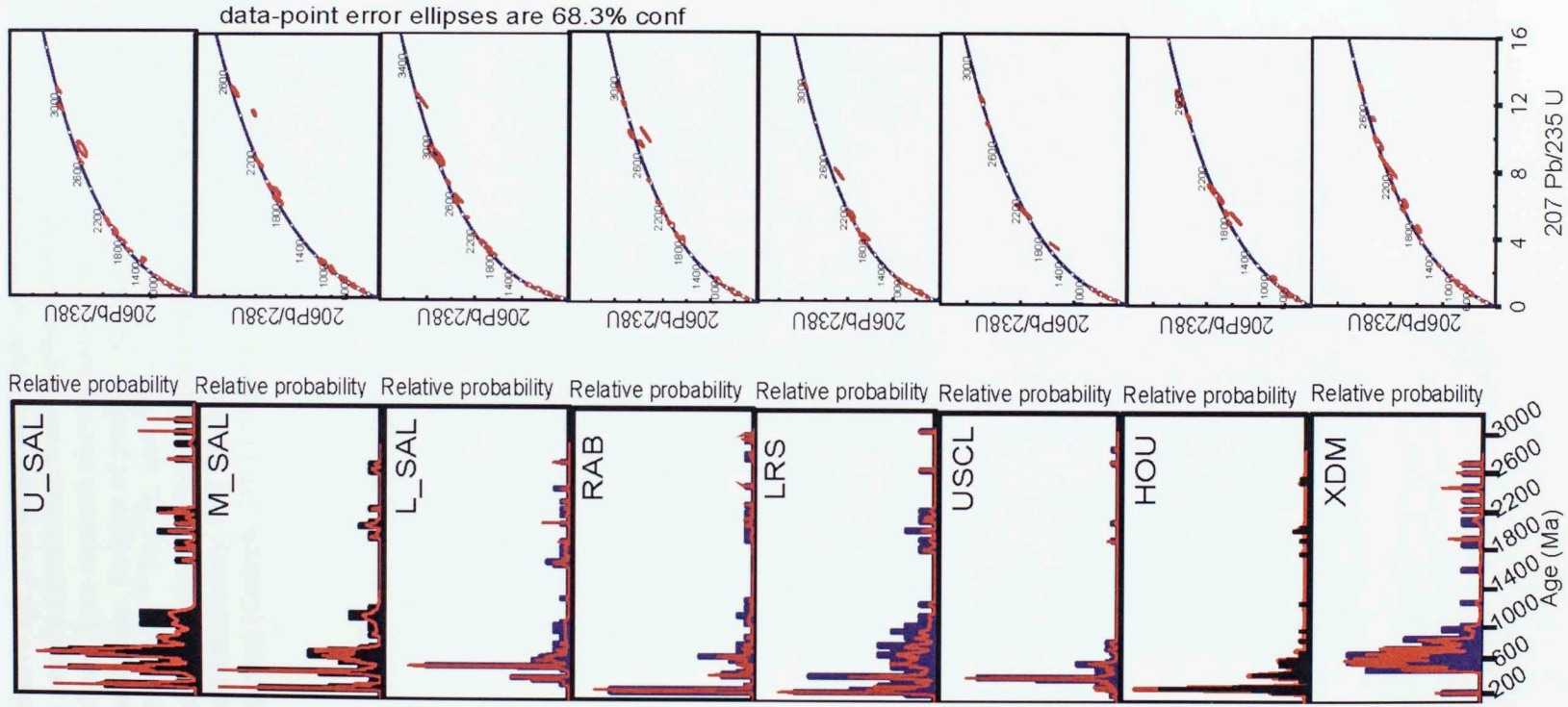


Figure 10. Relative age probability plots (*left*) and concordia diagrams (*right*) for each detrital zircon sample (determined with Isoplot; Ludwig, 2003). U-Pb ages represent individual analyses from separate zircons and are plotted as a normalized relative probability distribution. Heights of peaks correspond to statistical significance. Concordance based on $^{206}\text{Pb}/^{238}\text{U}$ and $^{206}\text{Pb}/^{207}\text{Pb}$ age (>20% discordance or >5% reverse discordance excluded). Individual data-point error ellipses represent the reported age and uncertainty, and are shown for the 68.3% confidence interval (1σ , measurement errors) (Gehrels, 2011). Note that most grains in this study are concordant.

Figure 11. Representative light micrographs of zircon grains from detrital zircon samples that were analyzed for U-Pb ages (see Table 1 for sample names and U-Pb zircon analyses). Images are in SEM, back-scattered electron (BSE) mode. Scale bars are 100 microns (petrography results).

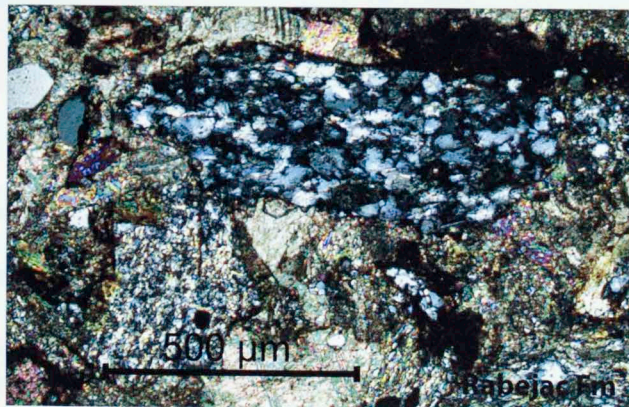
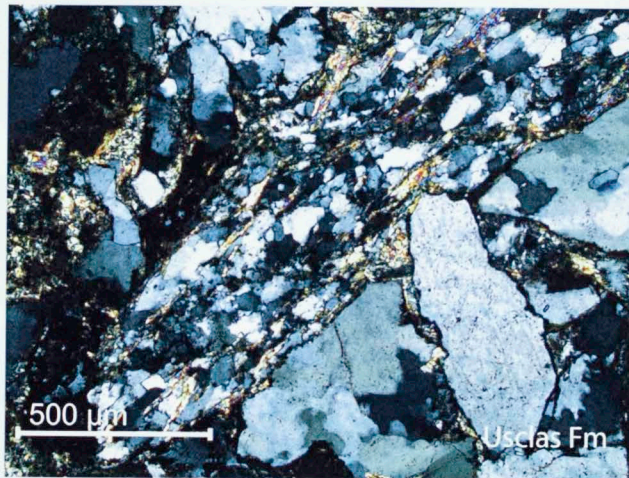
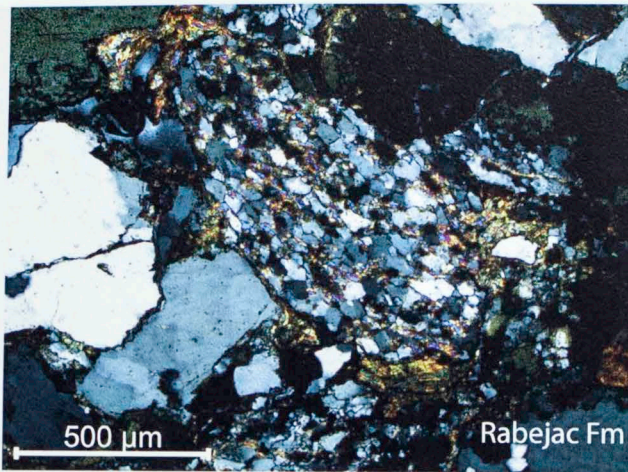


Figure 11. Representative light microscope images of lithic fragments in thin section samples that were analyzed for framework mineralogy (from same units of detrital zircon analyses). Images are in XPL. See Table 1 for modal percentages of framework grains (petrography results).

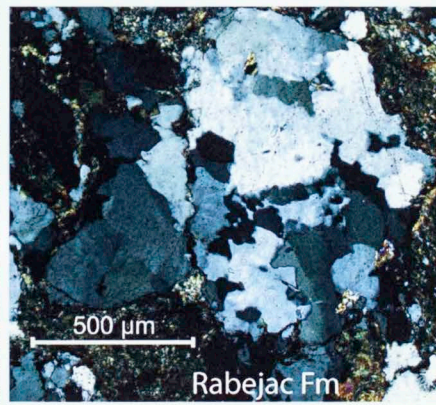
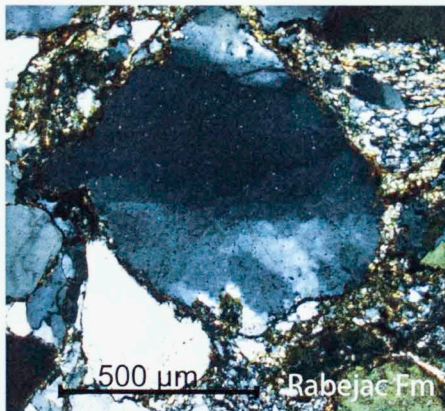
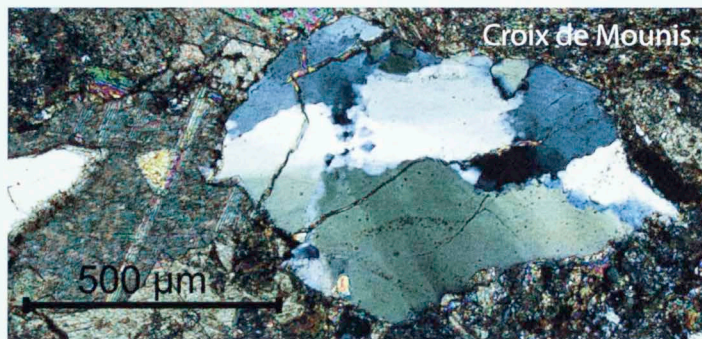
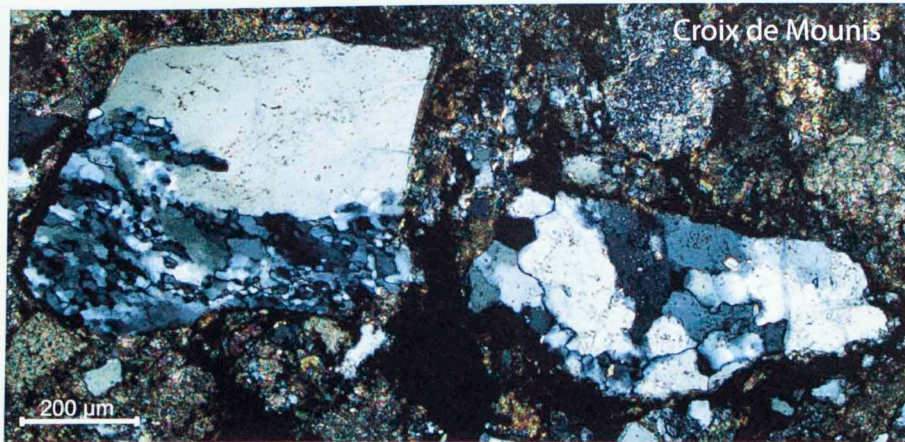


Figure 11. Representative light microscope images of polycrystalline quartz, and strained/undulose monocrystalline quartz in thin section samples that were analyzed for framework mineralogy (from same units of detrital zircon analyses). Images are in XPL. See Table 1 for modal percentages of framework grains (petrography results).

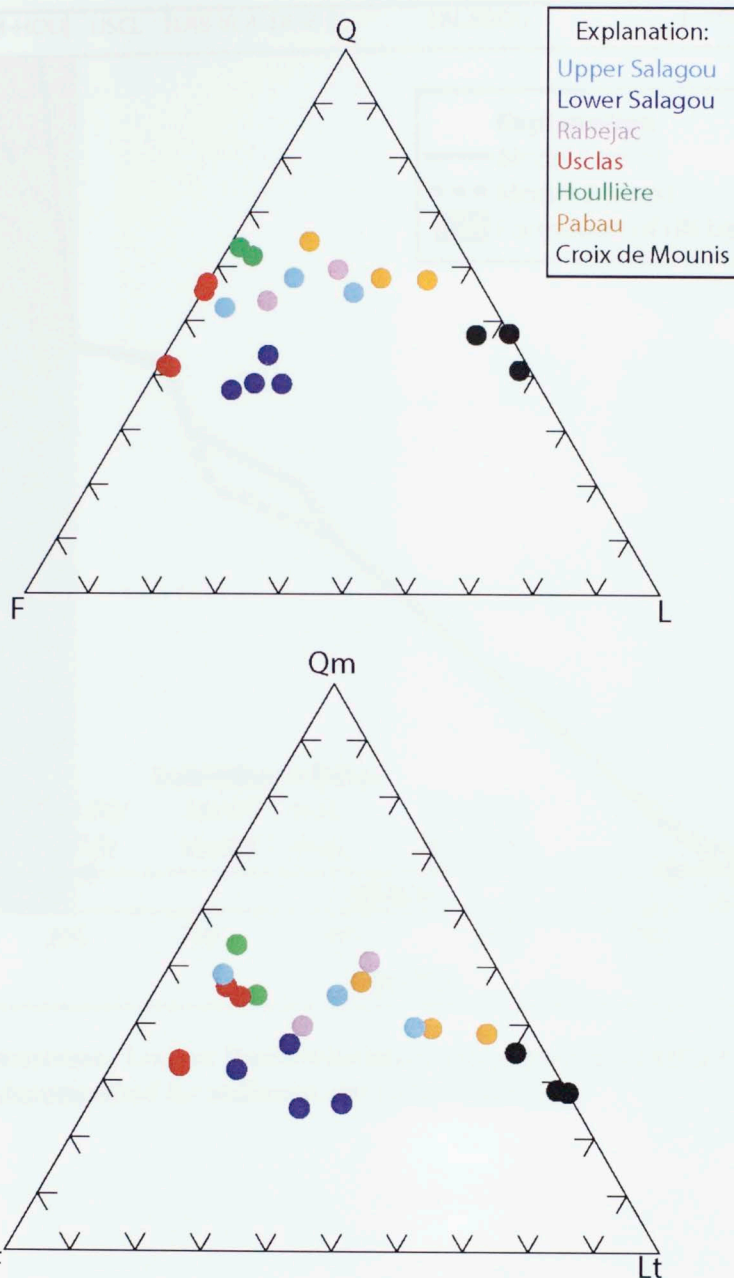


Figure 12. Ternary plots of framework mineralogy composition for Carboniferous-Permian sandstones in this study (21 thin sections total, 2-4 per unit; each data point represents one sample). Data are cast based on percentages of Q (quartz), F (feldspar; plagioclase and potassium), and L (metamorphic lithic fragments) on the top diagram, and based on percentages of Qm (monocrystalline quartz), F (feldspar; plagioclase and potassium), and Lt (total lithics; metamorphic, volcanic, and metavolcanic lithic fragments and Qp, polycrystalline quartz) on the lower diagram. A total of 400 points were counted per thin section. See App. D for further divisions of framework grain classification within QFL components.

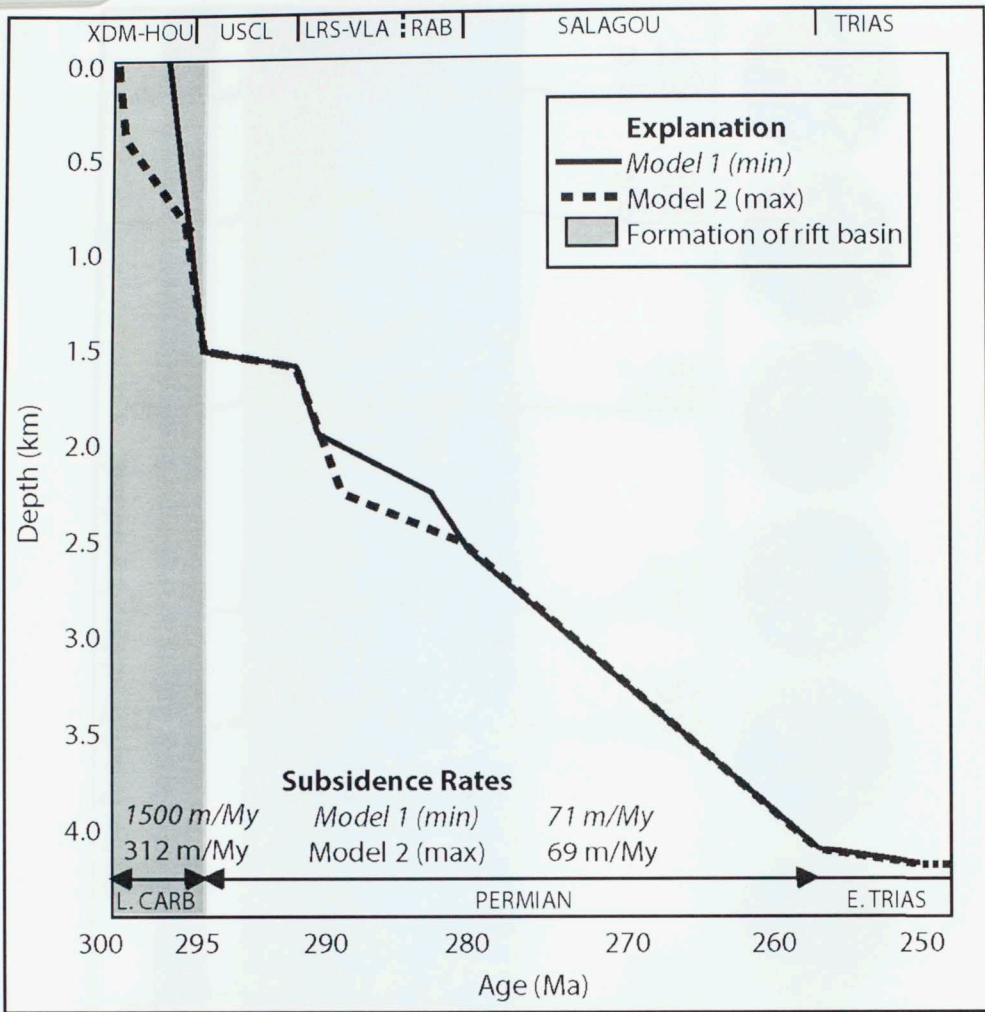
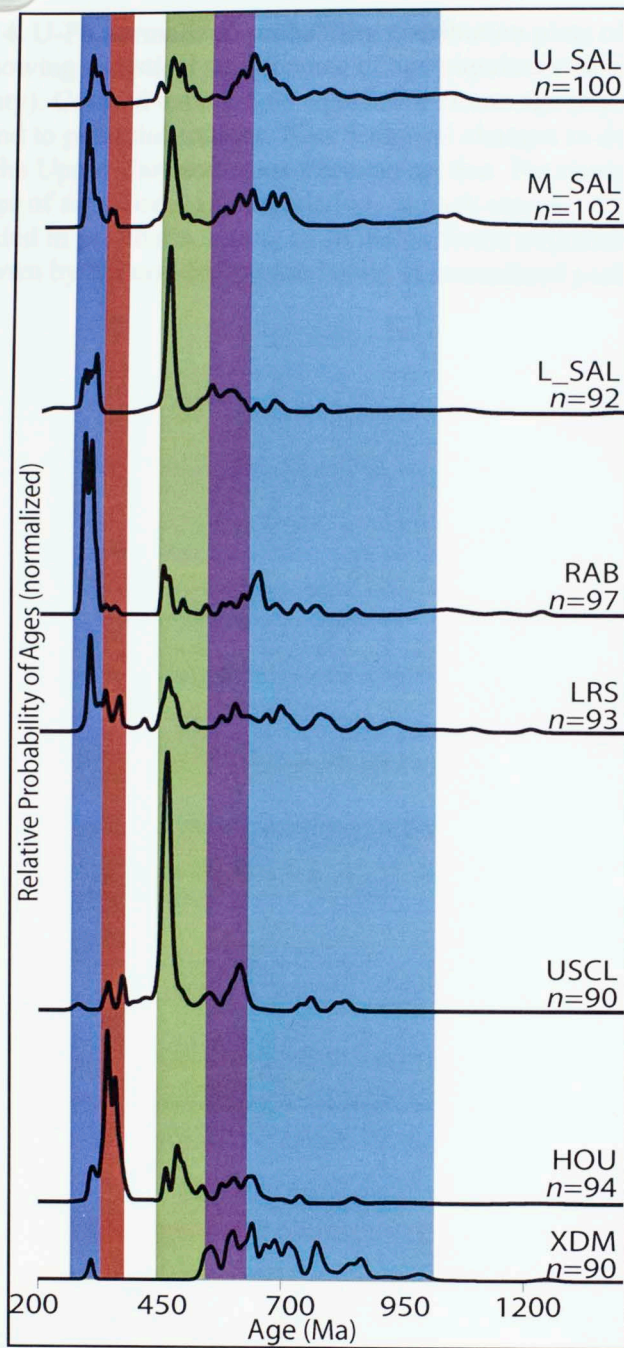


Figure 13. Graissessac- Lodève Basin subsidence plot, showing tectonic subsidence through time, decompacted for sediment and water loading.



- Mid Carboniferous- Early Permian (330-285 Ma)
- Late Devonian - Early Carboniferous (378-331 Ma)
- Cambro-Ordovician (552-445 Ma)
- Late Neoproterozoic (615-555 Ma)
- Early- Mid Neoproterozoic (1000-617 Ma)
- Archean-Precambrian (3000-1000 Ma)

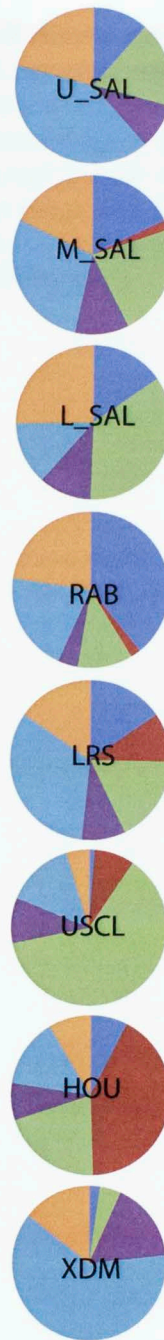


Figure 14. U-Pb normalized-probability distribution plots of all detrital zircon samples (N=8) showing statistical significance of age population peaks (reported with 1σ uncertainty). Colored bars denote significant zircon age populations (*legend*) that correspond to potential sources. Note temporal changes in dominant age populations through the Upper Carboniferous-Permian section. Pie charts (*right*) show variation by percentage of significant age populations in each sample. *Age range 445-378 Ma was not included in pie charts, owing to an insignificant population (0-2 grains avg.) in all units (shown by the non-highlighted zone in normalized probability plot).



Figure 15. QFL and QmPL1 versus $\ln(\text{Time})$ for detrital zircon grains with inferred detrital sorting of prograde metamorphism (Dickinson et al., 1993). A total of 400 grains were analyzed. The $\ln(\text{Time})$ of boundary lines are indicated.

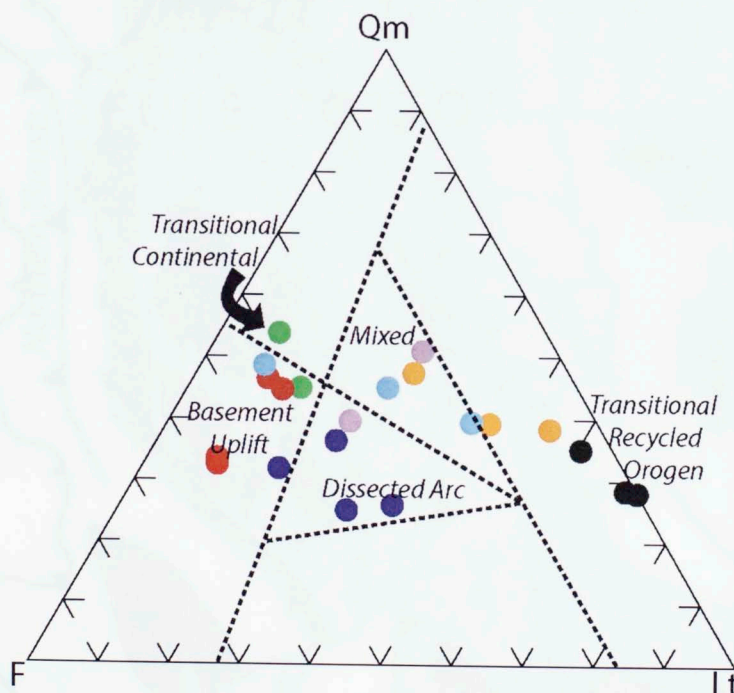
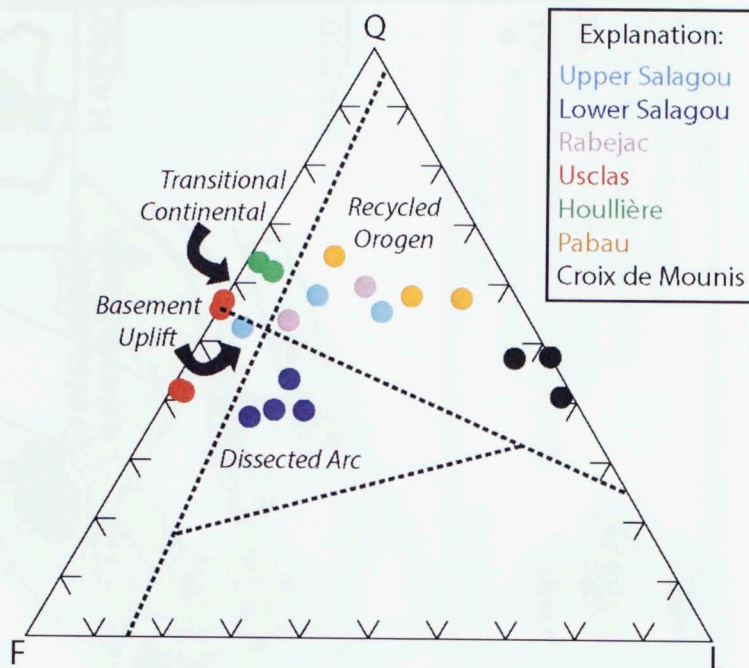


Figure 15. QFL and QmFLt ternary plots of framework results for all samples (Fig. 12) with inferred tectonic setting of provenance terranes based on framework modes (Dickinson et al., 1983). A total of 400 points were counted per thin section. Positions of boundary lines are empirical.

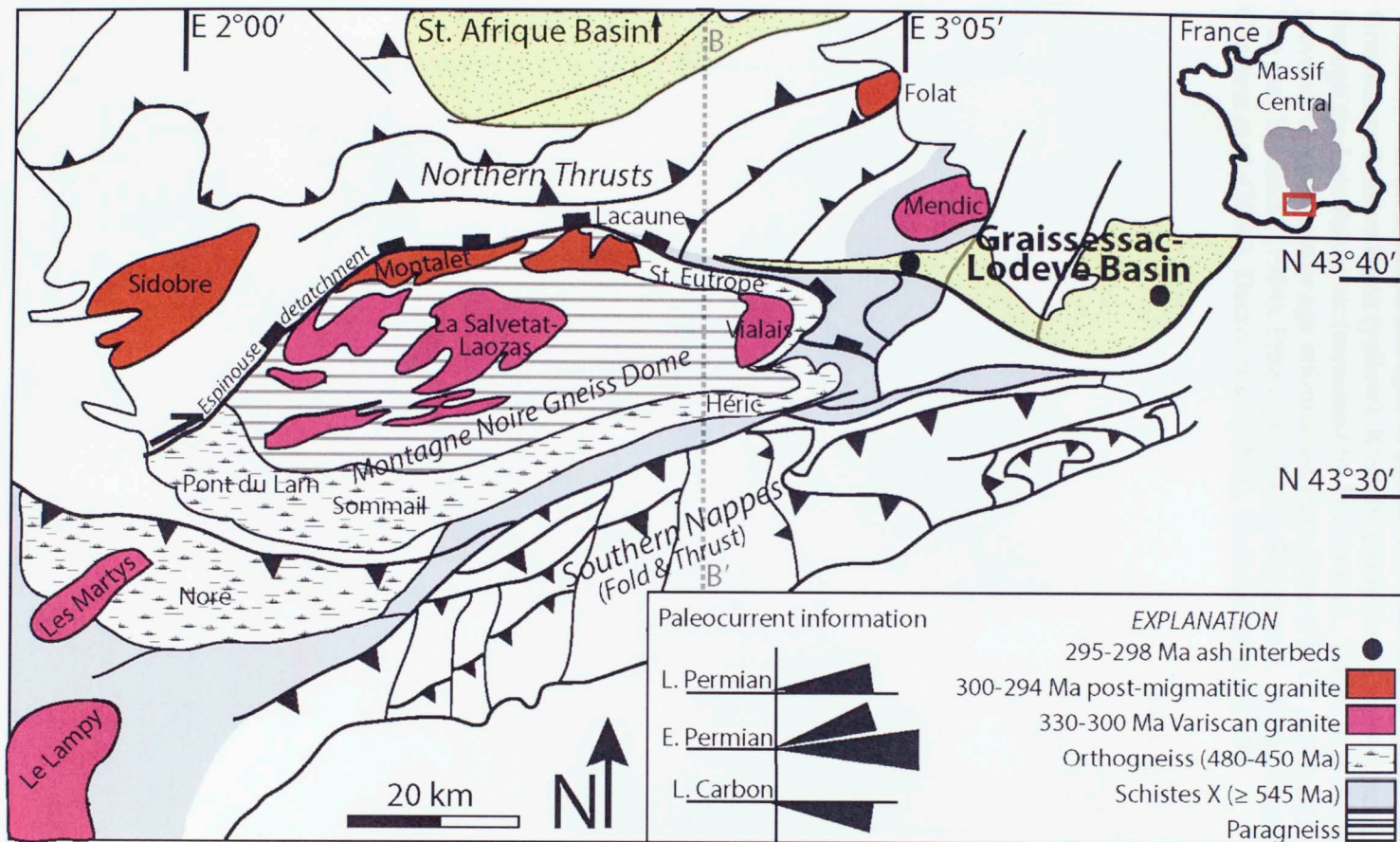


Figure 16. See caption on following page.

Figure 16. Structural map of the Montagne Noire gneiss dome (southern Massif Central), with the location and ages of possible source terranes proximal to the Graissessac-Lodève Basin (yellow). Rose diagrams (*inset*) show generalized paleoflow through the Late Paleozoic (measured by Pochat et al., 2005). Map modified from previous versions and/or age information from Gèze (1949), Arthaud (1970), Brun and Van Den Driessche (1994), Pitra et al. (2012), Roger et al. (2004), Faure et al. (2010), Cocherie et al. (2005), Ducrot et al. (1979), Melleton et al. (2010).



Figure 17. Simplified map of the Massif Central (southern France) showing the location and ages of possible source terranes for stream ages (including the Graissessac-Lodève Basin). Map is modified from Lutz et al. (1984), Faure et al. (2010), and Benoit et al. (2005), with ages are from Faure et al. (2010).

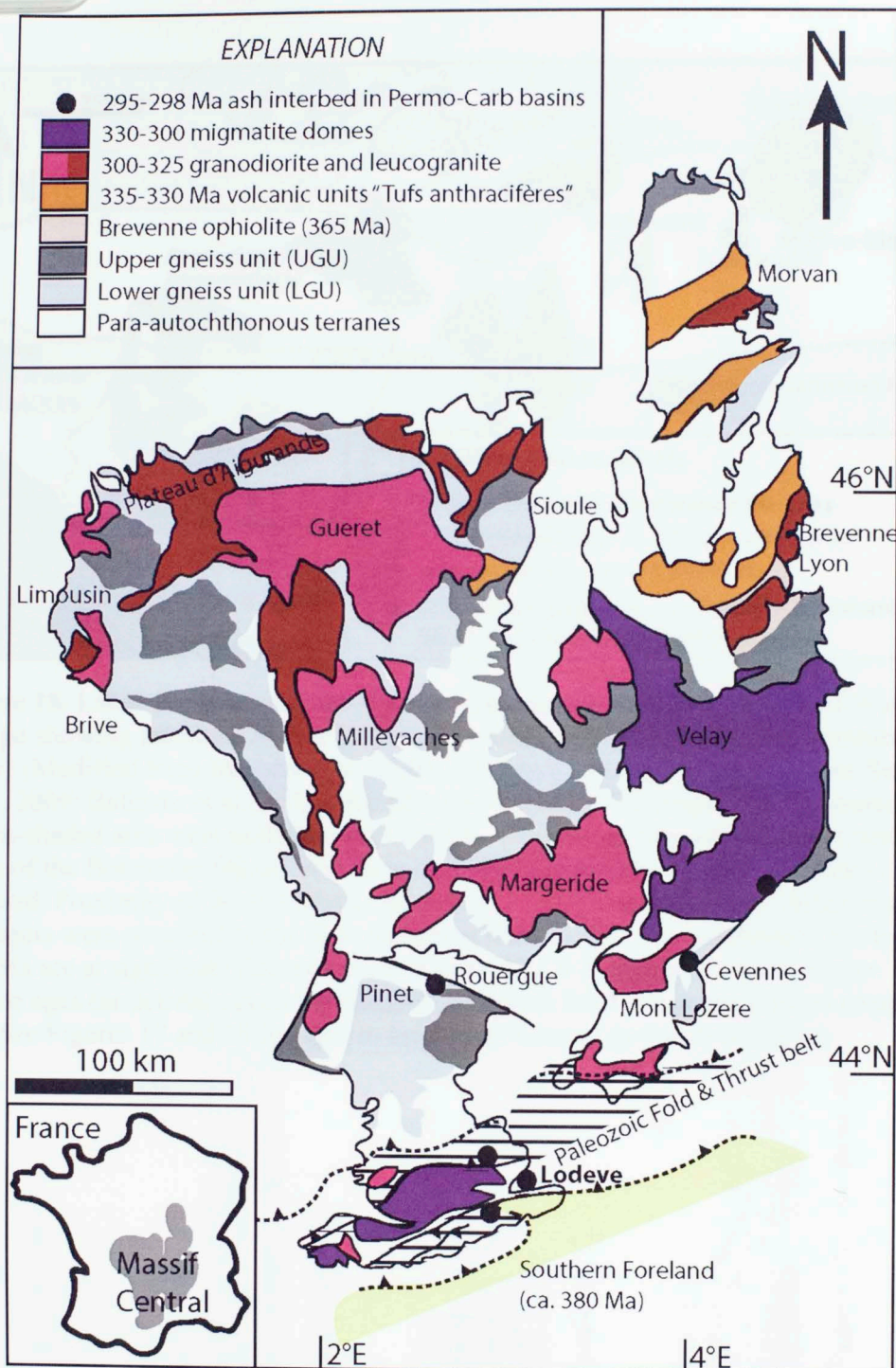


Figure 17. Simplified map of the Massif Central with locations and ages of possible source terranes for zircon ages (including volcanic ash, granitoids, and orthogneiss protoliths). Map is modified from Ledru et al. (1989) Femenias et al. (2003) and Bruguier et al. (2003), with ages are from Faure et al. (2010) and Melleton et al. (2010).

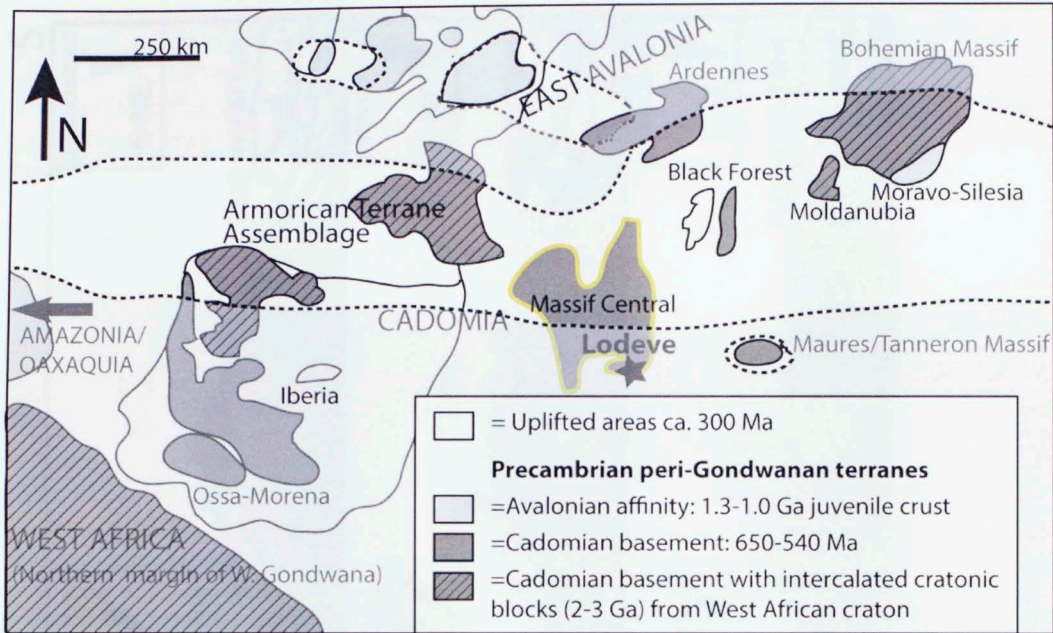


Figure 18. Latest Permian (ca. 250 Ma) reconstruction of the Variscan belt of Western Europe showing locations of Precambrian peri-Gondwanan and associated terranes (grey) (Modified from Murphy et al., 2004; Linnemann et al., 2007; Fernandez-Suarez et al., 2000; Ballevre et al., 2012). Based on paleogeographic maps (Fig. 3), massifs in the un-shaded area were uplifted ~300-250 Ma. Other areas of southern Iberia, and north of the Bohemian Massif may have also been subaerially exposed, but not as elevated. Proximity of West African craton (southwest) is approximate. Amazonia-Oaxaquia were proximal to the west margin of Iberia in the Neoproterozoic, but by ca. 250 Ma are at significant distance (near western North America). Possible source terrane ages for detrital zircon populations are drawn from numerous sources (App. E-10). See Figures 17 and 18 for ages in the Massif Central (not included here).

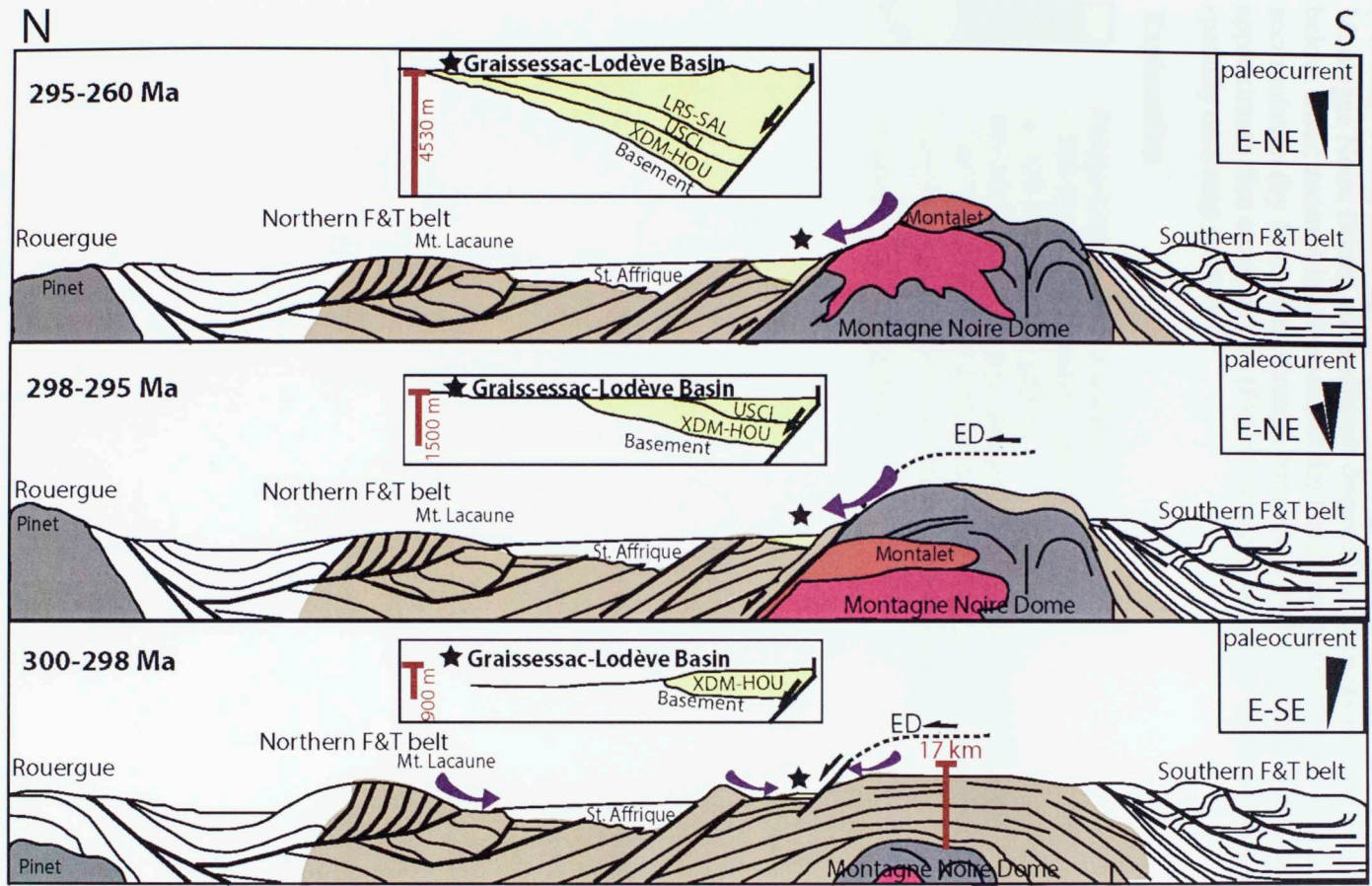




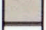




Figure 19. See caption and legend on following page.

Figure 19. Provenance through major time slices in the southern Massif Central (Montagne Noire) showing changes in paleogeography (progressive unroofing of the Montagne Noire Dome) and sediment dispersal patterns (purple arrows). *Legend:* below. *Inset:* zoomed in schematic of the Graissessac-Lodève basin showing sediment accumulation (by formation) through time. Note that the scale on this diagram is approximate. See cross section (Fig. 4) for scale, and Fig. 16 for cross section location spatially on a map from B-B'.

Explanation

	Permo-Carboniferous sediment
	< 300 Ma post-migmatitic granite
	ca. 320 Ma anatectic granite
	480-450 Ma orthogneiss-paragneiss and 319 Ma migmatite
	> 545 Ma Schistes X with Ordovician intrusions (orthogneiss)
	Upper Proterozoic-Lower Paleozoic metasediment
	Sediment dispersal pathways

Appendix B: Tables

Table 1. Summary of the data sets used in the analysis. The table shows the number of subjects, the number of trials, and the number of correct responses for each data set.

Data Set	Subjects	Trials	Correct Responses
1	10	100	70
2	10	100	70
3	10	100	70
4	10	100	70
5	10	100	70
6	10	100	70
7	10	100	70
8	10	100	70
9	10	100	70
10	10	100	70

Table 1.— *Detrital modes of Lodève Basin sandstones: QFL totals and percentages by formation.*

	Q			F			L			Total Points	Avg. Feldspar Type	
	#	%	<i>error range (2σ)</i>	#	%	<i>error range (2σ)</i>	#	%	<i>error range (2σ)</i>		% K-Spar	% Plag.
Upper Salagou (n=3)	650	55	<i>50-60</i>	364	31	<i>27-36</i>	165	14	<i>12-16</i>	1179	10	90
Lower Salagou (n=4)	608	39	<i>34-44</i>	672	44	<i>39-49</i>	262	17	<i>14-21</i>	1542	9	91
Rabejac (n=2)	434	57	<i>52-62</i>	217	28	<i>24-33</i>	117	15	<i>12-19</i>	768	29	71
Usclas (n=4)	773	49	<i>44-54</i>	794	50	<i>45-55</i>	14	1	<i>0-2</i>	1581	55	45
Houillère (n=2)	494	63	<i>59-68</i>	269	34	<i>30-39</i>	25	3	<i>2-4</i>	788	75	25
Pabau (n=3)	675	60	<i>55-65</i>	173	15	<i>12-19</i>	278	25	<i>21-30</i>	1126	6	94
Croix de Mounis (n=3)	449	46	<i>41-51</i>	24	2	<i>1-3</i>	517	52	<i>47-57</i>	990	19	81

Notes: Modes based on point counts of 400 QFL framework grains per sample. Minerals are identified following the Gazzi-Dickinson method (Ingersoll et al. 1984) with a 63 μm cutoff. Counts were conducted by the same operator on thin sections stained for potassium feldspar. Q, F, L numbers are totaled from smaller classification groups (App. D). Q= monocrystalline quartz, polycrystalline quartz, and quartz in lithic fragments (Qm + Qp2-3 + Qp>3 + Qr). F= monocrystalline potassium feldspar, monocrystalline plagioclase, and potassium feldspar and plagioclase in lithic fragments (Km + Pm + Kr + Pr). L= metamorphic lithic fragments (Lm). Columns on the right show the average ratios of potassium feldspar (K-spar) to plagioclase feldspar (Plag) in the formation (see App. D for results from discrete samples). Error ranges (*italics*) for modal analyses are calculated based on the chart for judging the reliability of point counting results (Van Der Plas and Tobi, 1965). For 400 framework grains, the average 2σ error is ~5%, but varies based on the estimated percent by volume of each mineral.

Table 2.— *Summary of detrital ages and percentages for each Lodève Basin sample, separated into groups by age.*

Period	M. Carb- E. Perm	L. Dev- E. Carb	M. Silur- M. Devon	Cambro- Ordovic	Late Neoproter	E. -Mid Neoproter	Mesoproter	Paleoproter	Archean- E. Paleoproter >2200	Total Zircon N
Age (Ma)	330-285	378-331	430-394	552-445	615-555	1000-617	1300-1000	2200-1600		
<i>Croix de Mounis Formation</i>										
# grains	2	0	0	4	15	56	2	6	5	90
%	2%	---	---	4%	17%	62%	2%	7%	6%	
<i>Houillère Formation</i>										
# grains	7	39	1	19	7	13	1	5	2	94
%	7%	41%	1%	20%	7%	14%	1%	5%	2%	
<i>Usclas Formation</i>										
# grains	1	7	5	53	8	12	0	2	2	90
%	1%	8%	6%	59%	9%	13%	0%	2%	2%	
<i>Loiras Formation</i>										
# grains	14	9	2	16	8	30	3	9	2	93
%	15%	10%	2%	17%	9%	32%	3%	10%	2%	
<i>Rabajec Formation</i>										
# grains	38	2	0	11	4	20	7	9	6	97
%	39%	2%	0%	11%	4%	21%	7%	9%	6%	
<i>Lower Salagou Formation</i>										
# grains	14	0	1	32	10	12	5	11	7	92
%	15%	---	1%	35%	11%	13%	5%	12%	8%	
<i>Middle Salagou Formation</i>										
# grains	18	2	1	23	11	29	9	7	2	102
%	18%	2%	1%	23%	11%	28%	9%	7%	2%	
<i>Upper Salagou Formation</i>										
# grains	11	0	4	17	9	39	6	10	4	100
%	11%	0%	4%	17%	9%	39%	6%	10%	4%	
<i>Summary of detrital ages from the Lodève Basin (N=8)</i>										
# grains	105	59	14	175	72	211	33	59	30	758
%	14%	8%	2%	23%	9%	28%	4%	8%	4%	

Notes: N = number of zircons analyzed per sample. See Fig. 14 (pie charts) for vertical variation in populations.

Table 3.— Summary of results from K-S, Overlap/Similarity, and Likeness statistical tests by sample pair comparisons.

TEST	XDM- HOU	XDM- USCL	XDM- RAB	XDM- L SAL	XDM- M SAL	XDM- U SAL	XDM- LRS	HOU- RAB	HOU- L SAL	HOU- M SAL
K-S Test <i>P</i>	0.000	0.000	0.000	0.000	0.000	0.001	0.000	0.000	0.000	0.000
Overlap <i>P</i>	0.600	0.379	0.740	0.637	0.696	0.661	0.708	0.738	0.672	0.803
Similarity <i>P</i>	0.427	0.369	0.555	0.535	0.596	0.690	0.655	0.581	0.531	0.637
Likeness %	27.9%	27.1%	34.0%	33.3%	43.8%	53.1%	46.5%	36.2%	35.7%	41.8%

TEST	HOU- U SAL	HOU- USCL	HOU- LRS	USCL- RAB	USCL- L SAL	USCL- M SAL	USCL- U SAL	USCL- LRS	LRS- RAB	LRS- L SAL
K-S Test <i>P</i>	0.000	0.000	0.001	0.000	0.014	0.000	0.000	0.000	0.005	0.499
Overlap <i>P</i>	0.698	0.513	0.739	0.464	0.481	0.499	0.605	0.474	0.773	0.768
Similarity <i>P</i>	0.623	0.620	0.718	0.484	0.672	0.622	0.638	0.628	0.718	0.732
Likeness %	43.2%	36.4%	49.6%	26.9%	50.1%	42.6%	43.4%	41.7%	50.2%	52.8%

TEST	LRS- U SAL	LRS- M SAL	RAB- L SAL	RAB- M SAL	LRS- U SAL	L SAL M SAL	RAB- USCL	L SAL U SAL	M SAL U SAL
K-S Test <i>P</i>	0.265	0.817	0.007	0.016	0.265	0.552	0.000	0.005	0.255
Overlap <i>P</i>	0.721	0.770	0.741	0.782	0.721	0.758	0.728	0.710	0.734
Similarity <i>P</i>	0.817	0.779	0.725	0.776	0.817	0.793	0.722	0.747	0.812
Likeness %	65.1%	61.4%	49.3%	55.7%	65.1%	61.6%	51.1%	52.7%	65.6%

Notes: The K-S test compares detrital zircon age distributions between two or more samples (Press et al., 1986). If $P < .05$, zircon from the two samples are likely derived from different populations. If $P > .05$ (gray), it is unlikely that two samples are derived from different populations. P-values are based on a 95% confidence level and are calculated using error in the CDF (App. E-4). The Overlap-Similarity test measures the degrees of age overlap and proportional similarity between age probability curves (with 1σ uncertainty). If ages perfectly overlap ($P = 1$), all grains could have been derived from same source. If overlap $P = 0$, there are no age matches. $P = 1$ for similarity indicates similar proportions of perfectly overlapping ages, and $P = 0$ reflects different proportions of ages that may not overlap (Gehrels, 2000). The “likeness” metric examines degrees of sameness among detrital zircon age populations (Satkoski et al., 2014). Values approaching 100% correspond to a higher degree of likeness. See Appendix E-6 for additional Likeness test output plots (likeness % vs. K-S P-values, and likeness as a function of age).

Appendix C: Detrital Zircon Ages (Raw Data)

Sample		Age (Ma)	
$^{206}\text{Pb}/^{238}\text{U}$	1σ	$^{206}\text{Pb}/^{207}\text{Pb}$	1σ
308.4	7.1	305.8	
308.1	4.4	302.2	
308.5	5.8	301.7	
308.9	2.8	298.7	
309.2	8.7	298.1	
309.3	9.4	297.7	
309.3	1.1	296.8	
309.4	8.1	296.2	
309.7	2.5	295.7	
309.9	1.1	295.2	
310.2	1.3	294.7	
310.3	1.3	294.2	
310.4	1.3	293.7	
310.5	1.3	293.2	
310.6	1.3	292.7	
310.7	1.3	292.2	
310.8	1.3	291.7	
310.9	1.3	291.2	
311.0	1.3	290.7	
311.1	1.3	290.2	
311.2	1.3	289.7	
311.3	1.3	289.2	
311.4	1.3	288.7	
311.5	1.3	288.2	
311.6	1.3	287.7	
311.7	1.3	287.2	
311.8	1.3	286.7	
311.9	1.3	286.2	
312.0	1.3	285.7	
312.1	1.3	285.2	
312.2	1.3	284.7	
312.3	1.3	284.2	
312.4	1.3	283.7	
312.5	1.3	283.2	
312.6	1.3	282.7	
312.7	1.3	282.2	
312.8	1.3	281.7	
312.9	1.3	281.2	
313.0	1.3	280.7	
313.1	1.3	280.2	
313.2	1.3	279.7	
313.3	1.3	279.2	
313.4	1.3	278.7	
313.5	1.3	278.2	
313.6	1.3	277.7	
313.7	1.3	277.2	
313.8	1.3	276.7	
313.9	1.3	276.2	
314.0	1.3	275.7	
314.1	1.3	275.2	
314.2	1.3	274.7	
314.3	1.3	274.2	
314.4	1.3	273.7	
314.5	1.3	273.2	
314.6	1.3	272.7	
314.7	1.3	272.2	
314.8	1.3	271.7	
314.9	1.3	271.2	
315.0	1.3	270.7	
315.1	1.3	270.2	
315.2	1.3	269.7	
315.3	1.3	269.2	
315.4	1.3	268.7	
315.5	1.3	268.2	
315.6	1.3	267.7	
315.7	1.3	267.2	
315.8	1.3	266.7	
315.9	1.3	266.2	
316.0	1.3	265.7	
316.1	1.3	265.2	
316.2	1.3	264.7	
316.3	1.3	264.2	
316.4	1.3	263.7	
316.5	1.3	263.2	
316.6	1.3	262.7	
316.7	1.3	262.2	
316.8	1.3	261.7	
316.9	1.3	261.2	
317.0	1.3	260.7	
317.1	1.3	260.2	
317.2	1.3	259.7	
317.3	1.3	259.2	
317.4	1.3	258.7	
317.5	1.3	258.2	
317.6	1.3	257.7	
317.7	1.3	257.2	
317.8	1.3	256.7	
317.9	1.3	256.2	
318.0	1.3	255.7	
318.1	1.3	255.2	
318.2	1.3	254.7	
318.3	1.3	254.2	
318.4	1.3	253.7	
318.5	1.3	253.2	
318.6	1.3	252.7	
318.7	1.3	252.2	
318.8	1.3	251.7	
318.9	1.3	251.2	
319.0	1.3	250.7	
319.1	1.3	250.2	
319.2	1.3	249.7	
319.3	1.3	249.2	
319.4	1.3	248.7	
319.5	1.3	248.2	
319.6	1.3	247.7	
319.7	1.3	247.2	
319.8	1.3	246.7	
319.9	1.3	246.2	
320.0	1.3	245.7	
320.1	1.3	245.2	
320.2	1.3	244.7	
320.3	1.3	244.2	
320.4	1.3	243.7	
320.5	1.3	243.2	
320.6	1.3	242.7	
320.7	1.3	242.2	
320.8	1.3	241.7	
320.9	1.3	241.2	
321.0	1.3	240.7	
321.1	1.3	240.2	
321.2	1.3	239.7	
321.3	1.3	239.2	
321.4	1.3	238.7	
321.5	1.3	238.2	
321.6	1.3	237.7	
321.7	1.3	237.2	
321.8	1.3	236.7	
321.9	1.3	236.2	
322.0	1.3	235.7	
322.1	1.3	235.2	
322.2	1.3	234.7	
322.3	1.3	234.2	
322.4	1.3	233.7	
322.5	1.3	233.2	
322.6	1.3	232.7	
322.7	1.3	232.2	
322.8	1.3	231.7	
322.9	1.3	231.2	
323.0	1.3	230.7	
323.1	1.3	230.2	
323.2	1.3	229.7	
323.3	1.3	229.2	
323.4	1.3	228.7	
323.5	1.3	228.2	
323.6	1.3	227.7	
323.7	1.3	227.2	
323.8	1.3	226.7	
323.9	1.3	226.2	
324.0	1.3	225.7	
324.1	1.3	225.2	
324.2	1.3	224.7	
324.3	1.3	224.2	
324.4	1.3	223.7	
324.5	1.3	223.2	
324.6	1.3	222.7	
324.7	1.3	222.2	
324.8	1.3	221.7	
324.9	1.3	221.2	
325.0	1.3	220.7	
325.1	1.3	220.2	
325.2	1.3	219.7	
325.3	1.3	219.2	
325.4	1.3	218.7	
325.5	1.3	218.2	
325.6	1.3	217.7	
325.7	1.3	217.2	
325.8	1.3	216.7	
325.9	1.3	216.2	
326.0	1.3	215.7	
326.1	1.3	215.2	
326.2	1.3	214.7	
326.3	1.3	214.2	
326.4	1.3	213.7	
326.5	1.3	213.2	
326.6	1.3	212.7	
326.7	1.3	212.2	
326.8	1.3	211.7	
326.9	1.3	211.2	
327.0	1.3	210.7	
327.1	1.3	210.2	
327.2	1.3	209.7	
327.3	1.3	209.2	
327.4	1.3	208.7	
327.5	1.3	208.2	
327.6	1.3	207.7	
327.7	1.3	207.2	
327.8	1.3	206.7	
327.9	1.3	206.2	
328.0	1.3	205.7	
328.1	1.3	205.2	
328.2	1.3	204.7	
328.3	1.3	204.2	
328.4	1.3	203.7	
328.5	1.3	203.2	
328.6	1.3	202.7	
328.7	1.3	202.2	
328.8	1.3	201.7	
328.9	1.3	201.2	
329.0	1.3	200.7	
329.1	1.3	200.2	
329.2	1.3	199.7	
329.3	1.3	199.2	
329.4	1.3	198.7	
329.5	1.3	198.2	
329.6	1.3	197.7	
329.7	1.3	197.2	
329.8	1.3	196.7	
329.9	1.3	196.2	
330.0	1.3	195.7	
330.1	1.3	195.2	
330.2	1.3	194.7	
330.3	1.3	194.2	
330.4	1.3	193.7	
330.5	1.3	193.2	
330.6	1.3	192.7	
330.7	1.3	192.2	
330.8	1.3	191.7	
330.9	1.3	191.2	
331.0	1.3	190.7	
331.1	1.3	190.2	
331.2	1.3	189.7	
331.3	1.3	189.2	
331.4	1.3	188.7	
331.5	1.3	188.2	
331.6	1.3	187.7	
331.7	1.3	187.2	
331.8	1.3	186.7	
331.9	1.3	186.2	
332.0	1.3	185.7	
332.1	1.3	185.2	
332.2	1.3	184.7	
332.3	1.3	184.2	
332.4	1.3	183.7	
332.5	1.3	183.2	
332.6	1.3	182.7	
332.7	1.3	182.2	
332.8	1.3	181.7	
332.9	1.3	181.2	
333.0	1.3	180.7	
333.1	1.3	180.2	
333.2	1.3	179.7	
333.3	1.3	179.2	
333.4	1.3	178.7	
333.5	1.3	178.2	
333.6	1.3	177.7	
333.7	1.3	177.2	
333.8	1.3	176.7	
333.9	1.3	176.2	
334.0	1.3	175.7	
334.1	1.3	175.2	
334.2	1.3	174.7	
334.3	1.3	174.2	
334.4	1.3	173.7	
334.5	1.3	173.2	
334.6	1.3	172.7	
334.7	1.3	172.2	
334.8	1.3	171.7	
334.9	1.3	171.2	
335.0	1.3	170.7	
335.1	1.3	170.2	
335.2	1.3	169.7	
335.3	1.3	169.2	
335.4	1.3	168.7	
335.5	1.3	168.2	
335.6	1.3	167.7	
335.7	1.3	167.2	
335.8	1.3	166.7	
335.9	1.3	166.2	
336.0	1.3	165.7	
336.1	1.3	165.2	
336.2	1.3	164.7	
336.3	1.3	164.2	
336.4	1.3	163.7	
336.5	1.3	163.2	
336.6	1.3	162.7	
336.7	1.3	162.2	
336.8	1.3	161.7	
336.9	1.3	161.2	
337.0	1.3	160.7	
337.1	1.3	160.2	
337.2	1.3	159.7	
337.3	1.3	159.2	
337.4	1.3	158.7	
337.5	1.3	158.2	
337.6	1.3	157.7	
337.7	1.3	157.2	
337.8	1.3	156.7	
337.9	1.3	156.2	
338.0	1.3	155.7	
338.1	1.3	155.2	
338.2	1.3	154.7	
338.3	1.3	154.2	
338.4	1.3	153.7	
338.5	1.3	153.2	
338.6	1.3	152.7	
338.7	1.3	152.2	
338.8	1.3	151.7	
338.9	1.3	151.2	
339.0	1.3	150.7	
339.1	1.3	150.2	
339.2	1.3	149.7	
339.3	1.3	149.2	
339.4	1.3	148.7	
339.5	1.3	148.2	
339.6	1.3	147.7	
339.7	1.3	147.2	
339.8	1.3	146.7	
339.9	1.3	146.2	
340.0	1.3	145.7	
340.1	1.3	145.2	
340.2	1.3	144.7	
340.3	1.3	144.2	
340.4	1.3	143.7	
340.5	1.3	143.2	
340.6	1.3	142.7	
340.7	1.3	142.2	
340.8	1.3	141.7	
340.9	1.3	141.2	
341.0	1.3	140.7	
341.1	1.3	140.2	
341.2	1.3	139.7	
341.3	1.3	139.2	
341.4	1.3	138.7	
341.5	1.3	138.2	
341.6	1.3	137.7	
341.7	1.3	137.2	
341.8	1.3	136.7	
341.9	1.3	136.2	
342.0	1.3	135.7	

Croix de Mounis (XDM) detrital zircon raw data.

		Apparent ages (Ma)						
206Pb*	±	207Pb*	±	206Pb*	±	Best age	±	Conc
238U*	(Ma)	235U	(Ma)	207Pb*	(Ma)	(Ma)	(Ma)	(%)
306.4	7.1	305.8	22.2	301.6	184.2	306.4	7.1	NA
309.1	4.4	302.0	30.1	247.0	264.0	309.1	4.4	NA
540.0	9.8	551.0	31.9	596.5	157.4	540.0	9.8	90.5
543.9	4.0	536.7	9.5	506.1	47.0	543.9	4.0	107.5
551.8	6.4	541.2	11.3	496.7	52.9	551.8	6.4	111.1
552.5	9.4	563.7	8.4	609.2	17.2	552.5	9.4	90.7
558.5	5.7	558.2	22.8	556.8	113.5	558.5	5.7	100.3
559.1	15.1	542.4	24.8	472.9	115.0	559.1	15.1	118.2
560.7	10.6	558.1	24.3	547.7	115.8	560.7	10.6	102.4
567.9	5.8	563.3	18.3	544.9	89.3	567.9	5.8	104.2
572.0	15.3	560.6	22.4	514.5	96.3	572.0	15.3	111.2
589.4	5.9	583.7	7.4	561.7	28.2	589.4	5.9	104.9
591.4	5.9	593.7	6.8	602.8	23.9	591.4	5.9	98.1
595.8	8.9	592.4	42.5	579.5	203.0	595.8	8.9	102.8
596.4	15.8	594.7	26.5	588.3	112.8	596.4	15.8	101.4
600.3	5.8	601.8	12.2	607.6	53.6	600.3	5.8	98.8
601.9	16.4	606.5	13.4	624.1	14.0	601.9	16.4	96.4
602.3	5.3	600.6	10.4	594.1	45.5	602.3	5.3	101.4
603.6	4.7	605.1	4.3	610.7	10.8	603.6	4.7	98.8
604.5	8.1	609.6	7.0	628.2	12.4	604.5	8.1	96.2
610.4	5.5	608.5	10.6	601.3	45.7	610.4	5.5	101.5
620.3	5.0	619.9	5.4	618.6	17.3	620.3	5.0	100.3
622.1	4.3	622.5	4.1	624.2	10.9	622.1	4.3	99.7
629.4	11.3	631.9	14.6	641.1	52.8	629.4	11.3	98.2
630.5	8.9	642.2	20.6	683.4	87.0	630.5	8.9	92.3
631.0	2.3	631.9	3.6	634.9	14.3	631.0	2.3	99.4
639.5	24.0	640.1	21.9	642.5	52.0	639.5	24.0	99.5
639.5	6.8	633.8	13.6	613.4	57.6	639.5	6.8	104.3
640.5	5.3	636.5	17.3	622.3	76.8	640.5	5.3	102.9
641.8	19.1	656.8	18.9	708.9	49.7	641.8	19.1	90.5
643.5	5.3	649.8	7.2	671.7	26.5	643.5	5.3	95.8
643.9	6.4	643.1	6.5	640.4	19.0	643.9	6.4	100.5
645.4	5.4	640.9	9.8	624.9	40.3	645.4	5.4	103.3
650.7	15.8	669.6	15.0	733.5	35.4	650.7	15.8	88.7
661.3	4.2	662.5	5.2	666.4	17.9	661.3	4.2	99.2
662.5	16.1	659.1	35.9	647.8	149.2	662.5	16.1	102.3
669.0	4.3	671.3	5.6	679.1	19.7	669.0	4.3	98.5
670.3	2.2	674.1	6.7	686.9	27.9	670.3	2.2	97.6
679.4	11.7	685.7	18.4	706.7	68.3	679.4	11.7	96.1
683.8	16.1	678.3	13.1	659.9	20.0	683.8	16.1	103.6
684.9	6.8	682.3	5.9	673.9	12.0	684.9	6.8	101.6
688.3	8.1	693.8	11.5	711.7	40.7	688.3	8.1	96.7

691.4	4.6	694.4	10.8	704.2	43.3	691.4	4.6	98.2
693.4	14.0	696.6	10.9	706.8	7.3	693.4	14.0	98.1
700.7	24.2	703.3	19.8	711.6	29.7	700.7	24.2	98.5
703.4	16.0	704.1	15.6	706.2	40.3	703.4	16.0	99.6
705.6	13.7	710.5	13.3	726.0	33.8	705.6	13.7	97.2
705.7	20.1	746.2	41.5	869.7	150.2	705.7	20.1	81.1
714.4	3.3	715.6	4.6	719.3	16.0	714.4	3.3	99.3
715.3	4.8	715.0	9.8	713.8	37.5	715.3	4.8	100.2
718.2	8.9	714.9	12.4	704.5	43.4	718.2	8.9	101.9
721.7	10.9	734.3	10.4	773.1	24.9	721.7	10.9	93.4
730.2	3.5	738.6	5.0	764.0	17.0	730.2	3.5	95.6
730.4	5.1	733.7	16.0	743.6	63.1	730.4	5.1	98.2
736.8	8.2	740.0	6.8	749.7	10.6	736.8	8.2	98.3
759.4	15.7	769.6	12.3	799.4	13.3	759.4	15.7	95.0
770.9	7.7	773.8	14.4	782.0	51.3	770.9	7.7	98.6
771.6	4.2	773.1	8.7	777.7	31.7	771.6	4.2	99.2
777.0	13.3	777.4	13.6	778.5	36.3	777.0	13.3	99.8
777.7	6.1	775.2	9.5	768.0	32.6	777.7	6.1	101.3
779.2	14.6	780.9	35.2	785.8	129.1	779.2	14.6	99.2
781.9	10.3	779.8	7.9	773.8	8.3	781.9	10.3	101.0
784.6	13.2	783.2	13.1	779.4	33.8	784.6	13.2	100.7
789.4	14.4	788.4	13.3	785.4	30.8	789.4	14.4	100.5
811.7	9.3	819.2	11.6	839.7	34.8	811.7	9.3	96.7
829.7	8.6	826.2	16.0	816.8	54.5	829.7	8.6	101.6
841.6	5.5	847.9	7.5	864.5	22.6	841.6	5.5	97.4
848.3	9.6	843.9	16.3	832.3	53.8	848.3	9.6	101.9
852.3	15.4	853.9	37.3	857.9	127.9	852.3	15.4	99.4
865.9	5.4	868.1	10.5	873.8	34.6	865.9	5.4	99.1
866.1	23.5	885.3	44.9	933.4	144.0	866.1	23.5	92.8
867.4	7.5	882.1	5.6	919.2	5.1	867.4	7.5	94.4
873.9	11.4	883.1	8.8	906.2	11.2	873.9	11.4	96.4
913.6	6.7	915.1	7.1	918.6	18.2	913.6	6.7	99.5
983.4	9.7	980.4	19.2	973.6	58.4	983.4	9.7	101.0
949.4	16.5	957.6	13.4	976.5	21.8	949.4	16.5	97.2
979.9	8.1	982.9	7.3	989.3	15.3	979.9	8.1	99.0
1019.7	9.8	1018.4	31.4	1015.5	96.8	1019.7	9.8	100.4
1256.7	12.6	1253.1	11.0	1246.9	20.7	1256.7	12.6	100.8
1607.1	12.0	1603.4	21.5	1598.5	47.3	1607.1	12.0	100.5
1668.6	31.5	1748.9	26.7	1846.3	42.9	1668.6	31.5	90.4
1954.7	26.6	1933.8	13.7	1911.4	3.8	1954.7	26.6	102.3
1916.1	26.8	1996.0	22.6	2079.7	35.5	1916.1	26.8	92.1
2124.9	13.7	2119.4	10.6	2114.1	16.1	2124.9	13.7	100.5
2184.4	20.5	2200.1	10.4	2214.8	5.5	2184.4	20.5	98.6
2219.6	99.8	2267.7	48.3	2311.4	6.2	2219.6	99.8	96.0
2390.1	51.4	2410.9	25.7	2428.6	18.2	2390.1	51.4	98.4
2396.3	14.4	2420.4	6.9	2440.7	3.5	2396.3	14.4	98.2
2467.0	14.3	2539.4	7.1	2597.8	4.9	2467.0	14.3	95.0
2671.2	21.0	2682.8	9.6	2691.6	5.4	2671.2	21.0	99.2

Houillère (HOU) detrital zircon raw data.

Apparent ages (Ma)								
206Pb*	±	207Pb*	±	206Pb*	±	Best age	±	Conc
238U*	(Ma)	235U	(Ma)	207Pb*	(Ma)	(Ma)	(Ma)	(%)
306.8	4.7	307.2	8.0	309.5	58.6	306.8	4.7	NA
308.1	5.5	308.3	11.2	309.6	85.9	308.1	5.5	NA
312.8	4.5	316.4	7.2	343.4	49.8	312.8	4.5	NA
313.3	22.6	315.3	21.6	330.7	67.5	313.3	22.6	NA
316.1	4.7	318.2	17.7	333.6	143.1	316.1	4.7	NA
322.8	5.0	330.9	8.3	388.0	55.4	322.8	5.0	NA
330.8	3.0	329.5	5.6	320.6	39.9	330.8	3.0	NA
332.6	5.4	328.6	21.7	300.3	172.3	332.6	5.4	NA
336.5	9.9	345.8	20.4	408.7	140.6	336.5	9.9	NA
336.5	2.1	337.2	12.6	341.7	98.2	336.5	2.1	NA
337.2	4.1	339.5	18.8	355.5	144.7	337.2	4.1	NA
338.2	10.2	331.1	25.6	281.7	195.4	338.2	10.2	NA
339.0	4.7	345.0	7.8	385.9	50.5	339.0	4.7	NA
340.4	2.7	344.9	5.1	375.3	35.0	340.4	2.7	NA
340.5	7.6	341.4	12.1	347.6	79.5	340.5	7.6	NA
341.5	3.7	340.6	5.3	334.1	33.0	341.5	3.7	NA
341.9	3.5	339.3	4.9	321.8	30.4	341.9	3.5	NA
342.6	2.0	341.7	6.9	335.8	52.5	342.6	2.0	NA
342.6	2.8	344.8	4.4	359.3	28.3	342.6	2.8	NA
344.7	7.4	348.9	15.0	376.9	103.4	344.7	7.4	NA
344.7	3.2	345.3	10.4	349.5	77.5	344.7	3.2	NA
345.8	7.6	348.5	7.5	366.2	26.6	345.8	7.6	NA
346.0	5.5	349.1	10.8	369.4	73.8	346.0	5.5	NA
346.4	4.8	348.8	12.4	364.6	89.5	346.4	4.8	NA
347.6	3.0	347.3	7.8	345.8	56.5	347.6	3.0	NA
349.0	4.2	348.6	8.0	346.1	54.6	349.0	4.2	NA
349.3	31.5	377.8	40.9	556.4	197.5	349.3	31.5	NA
349.6	3.7	351.1	5.6	360.6	34.9	349.6	3.7	NA
352.7	8.5	356.7	34.4	382.6	251.6	352.7	8.5	NA
354.0	4.5	331.7	19.4	177.8	157.3	354.0	4.5	NA
354.2	16.2	350.3	18.5	324.6	93.3	354.2	16.2	NA
356.4	4.3	353.0	15.0	330.8	110.8	356.4	4.3	NA
356.5	4.5	363.3	7.4	406.5	46.1	356.5	4.5	NA
357.0	3.8	357.9	11.2	363.6	80.4	357.0	3.8	NA
359.2	3.4	355.5	14.6	331.7	107.9	359.2	3.4	NA
360.3	3.8	354.1	10.4	313.9	75.2	360.3	3.8	NA
361.4	4.6	352.8	10.3	296.6	73.0	361.4	4.6	NA
362.2	5.3	336.6	35.2	163.9	286.0	362.2	5.3	NA
363.8	7.2	381.0	24.2	487.1	162.3	363.8	7.2	NA
364.7	8.4	370.4	12.9	406.3	76.6	364.7	8.4	NA
365.9	10.3	380.4	16.9	469.7	98.8	365.9	10.3	NA
368.6	9.3	411.4	28.2	659.4	170.2	368.6	9.3	NA
369.1	4.1	363.7	12.2	329.3	86.9	369.1	4.1	NA

369.7	5.8	356.5	40.8	271.7	310.1	369.7	5.8	NA
374.0	20.5	374.6	24.5	378.4	121.1	374.0	20.5	NA
378.6	6.5	371.8	27.2	329.7	194.4	378.6	6.5	NA
427.1	21.4	436.7	24.8	487.8	103.6	427.1	21.4	87.6
461.7	5.3	469.4	9.3	507.4	47.8	461.7	5.3	91.0
463.7	4.7	468.4	9.6	491.3	51.3	463.7	4.7	94.4
466.0	5.2	454.5	14.4	397.0	84.1	466.0	5.2	117.4
478.0	14.6	488.9	20.5	540.2	92.3	478.0	14.6	88.5
481.1	3.8	484.5	11.6	500.6	63.6	481.1	3.8	96.1
485.5	3.3	482.6	8.8	468.8	48.0	485.5	3.3	103.6
487.1	5.6	486.6	8.5	484.5	40.6	487.1	5.6	100.5
487.3	5.2	473.7	14.2	408.7	80.0	487.3	5.2	119.2
490.0	3.6	487.0	5.8	472.8	28.6	490.0	3.6	103.6
490.2	20.8	478.2	19.9	420.9	62.2	490.2	20.8	116.5
491.2	11.0	481.2	17.6	433.9	88.5	491.2	11.0	113.2
498.1	3.6	500.0	7.2	508.6	36.6	498.1	3.6	97.9
500.2	5.8	502.2	12.6	511.0	64.8	500.2	5.8	97.9
506.0	12.4	507.3	13.3	512.8	47.3	506.0	12.4	98.7
510.2	12.7	517.9	23.4	552.0	112.4	510.2	12.7	92.4
510.6	7.1	509.3	19.9	503.6	104.8	510.6	7.1	101.4
535.2	9.3	526.9	34.6	491.0	181.8	535.2	9.3	109.0
539.7	6.6	536.8	13.2	524.6	63.7	539.7	6.6	102.9
549.1	21.8	522.0	64.9	404.9	344.9	549.1	21.8	135.6
576.1	5.7	562.7	16.7	508.5	81.9	576.1	5.7	113.3
585.7	8.5	586.4	16.2	589.1	71.8	585.7	8.5	99.4
588.8	40.9	591.5	34.4	602.2	53.4	588.8	40.9	97.8
595.3	10.6	585.3	15.0	546.7	61.4	595.3	10.6	108.9
595.3	16.2	597.4	20.3	605.5	74.8	595.3	16.2	98.3
600.6	6.7	610.4	8.4	647.1	30.2	600.6	6.7	92.8
608.3	5.4	619.0	11.9	658.4	51.3	608.3	5.4	92.4
619.9	12.4	623.3	19.7	635.7	78.9	619.9	12.4	97.5
626.3	37.6	645.5	43.5	713.1	139.3	626.3	37.6	87.8
630.4	6.9	626.2	16.2	610.8	70.8	630.4	6.9	103.2
631.7	12.6	618.3	17.3	569.6	67.2	631.7	12.6	110.9
636.2	9.0	635.4	8.2	632.5	18.7	636.2	9.0	100.6
641.2	20.2	645.5	49.2	660.6	209.2	641.2	20.2	97.1
642.4	6.4	632.2	9.6	596.0	38.0	642.4	6.4	107.8
649.2	6.0	643.3	12.3	622.5	51.6	649.2	6.0	104.3
663.9	12.8	662.9	11.9	659.5	28.9	663.9	12.8	100.7
700.7	14.7	707.7	16.6	729.7	50.7	700.7	14.7	96.0
739.6	5.3	741.7	13.3	748.0	51.1	739.6	5.3	98.9
848.2	10.1	862.6	9.5	899.9	21.5	848.2	10.1	94.3
981.1	13.3	970.2	16.3	945.5	44.5	945.5	44.5	103.8
860.7	28.1	970.0	27.7	1226.4	53.4	1226.4	53.4	70.2
1760.3	20.5	1759.1	15.1	1757.6	22.4	1757.6	22.4	100.2
1815.8	17.5	1849.9	15.6	1888.5	26.3	1888.5	26.3	96.2
847.6	42.9	1232.8	40.0	1988.3	26.2	1988.3	26.2	42.6
1635.3	66.7	1801.3	39.3	1999.2	10.8	1999.2	10.8	81.8
2004.2	90.4	2013.4	47.8	2022.9	26.0	2022.9	26.0	99.1
2476.6	23.9	2481.9	11.9	2486.1	9.2	2486.1	9.2	99.6
2628.2	37.3	2575.3	22.4	2533.8	27.8	2533.8	27.8	103.7

Usclas (USCL) detrital zircon raw data.

Apparent ages (Ma)								
206Pb*	±	207Pb*	±	206Pb*	±	Best age	±	Conc
238U*	(Ma)	235U	(Ma)	207Pb*	(Ma)	(Ma)	(Ma)	(%)
281.3	9.2	298.6	15.8	435.9	113.6	281.3	9.2	NA
336.6	4.5	337.2	8.3	341.5	58.1	336.6	4.5	NA
343.4	2.1	341.3	6.2	326.9	46.1	343.4	2.1	NA
348.8	4.4	349.9	9.9	356.8	69.5	348.8	4.4	NA
368.3	31.1	368.2	28.4	367.6	67.8	368.3	31.1	NA
369.6	4.4	379.3	18.7	439.2	129.0	369.6	4.4	NA
372.7	2.6	373.8	13.9	380.3	98.8	372.7	2.6	NA
377.2	3.6	378.0	7.7	383.2	50.1	377.2	3.6	NA
394.1	9.1	413.0	13.3	520.2	68.4	394.1	9.1	NA
414.5	10.2	431.9	11.0	525.9	39.9	414.5	10.2	78.8
419.4	14.4	411.6	27.7	367.9	166.3	419.4	14.4	114.0
421.7	4.8	419.4	13.6	406.9	84.7	421.7	4.8	103.7
424.8	10.7	430.2	12.9	459.5	57.0	424.8	10.7	92.4
444.2	20.5	446.8	21.4	460.3	77.6	444.2	20.5	96.5
448.5	6.4	457.7	7.3	504.1	28.9	448.5	6.4	89.0
448.8	8.2	453.1	8.9	475.0	34.1	448.8	8.2	94.5
450.4	22.5	459.8	20.1	506.9	36.4	450.4	22.5	88.9
451.9	6.8	453.3	12.1	460.6	64.6	451.9	6.8	98.1
455.3	5.2	455.4	7.4	456.1	35.9	455.3	5.2	99.8
455.8	4.9	454.5	9.4	447.9	51.5	455.8	4.9	101.8
455.8	4.1	456.1	7.6	457.6	40.7	455.8	4.1	99.6
455.9	6.1	455.6	8.6	454.3	42.2	455.9	6.1	100.3
456.3	9.3	457.6	13.7	463.8	67.9	456.3	9.3	98.4
456.8	4.4	460.9	9.0	481.6	49.3	456.8	4.4	94.8
457.1	3.2	458.7	7.0	466.8	39.0	457.1	3.2	97.9
458.5	7.0	460.8	7.2	471.9	24.5	458.5	7.0	97.2
458.6	3.6	460.3	12.6	468.3	73.1	458.6	3.6	97.9
458.7	2.0	464.4	8.1	492.6	46.8	458.7	2.0	93.1
459.2	9.2	469.1	16.4	517.8	84.1	459.2	9.2	88.7
460.8	6.7	459.1	19.2	450.2	110.6	460.8	6.7	102.4
461.2	8.6	456.9	36.6	435.5	217.4	461.2	8.6	105.9
461.3	5.8	460.8	22.8	458.6	133.6	461.3	5.8	100.6
461.5	7.2	459.9	9.3	451.9	42.7	461.5	7.2	102.1
462.0	5.0	455.5	6.7	422.5	32.5	462.0	5.0	109.4
462.7	4.7	462.7	6.5	462.3	30.8	462.7	4.7	100.1
462.8	4.4	463.6	7.7	467.5	40.4	462.8	4.4	99.0
462.9	4.6	462.1	8.7	458.0	46.8	462.9	4.6	101.1
464.6	14.4	471.0	15.6	502.4	57.6	464.6	14.4	92.5
464.9	3.3	461.4	4.8	444.1	23.5	464.9	3.3	104.7
465.0	3.4	464.3	11.5	461.2	66.1	465.0	3.4	100.8
465.0	4.5	465.0	9.8	465.1	53.7	465.0	4.5	100.0
465.1	3.8	462.0	10.3	447.0	58.6	465.1	3.8	104.0
465.4	3.9	464.6	6.5	460.5	33.8	465.4	3.9	101.1

465.4	11.8	460.6	11.8	436.8	40.4	465.4	11.8	106.6
466.0	8.1	462.2	8.7	443.7	33.2	466.0	8.1	105.0
467.1	5.2	468.3	14.4	474.3	80.9	467.1	5.2	98.5
467.1	7.8	475.0	13.9	513.1	71.1	467.1	7.8	91.0
467.6	4.2	466.5	6.4	460.6	31.4	467.6	4.2	101.5
468.6	6.1	468.2	12.9	466.4	69.9	468.6	6.1	100.5
469.6	7.8	467.8	11.9	458.9	59.1	469.6	7.8	102.3
470.3	5.2	476.1	6.8	504.2	30.2	470.3	5.2	93.3
471.1	2.3	471.5	10.1	473.2	58.1	471.1	2.3	99.5
471.1	29.7	476.4	28.0	502.2	75.2	471.1	29.7	93.8
471.1	4.4	463.0	10.8	422.9	60.9	471.1	4.4	111.4
471.6	5.1	463.8	9.0	425.4	48.1	471.6	5.1	110.9
473.8	6.2	481.4	11.3	517.5	57.2	473.8	6.2	91.6
479.8	11.8	482.3	14.3	494.4	59.3	479.8	11.8	97.0
480.7	4.8	465.2	10.7	389.6	59.7	480.7	4.8	123.4
482.1	28.4	483.4	25.7	489.6	58.7	482.1	28.4	98.5
491.7	8.8	495.0	11.3	510.1	48.8	491.7	8.8	96.4
496.4	9.3	496.2	15.4	495.4	74.9	496.4	9.3	100.2
504.3	29.1	499.9	24.9	479.8	42.4	504.3	29.1	105.1
525.0	40.0	545.1	36.0	629.9	67.7	525.0	40.0	83.3
547.8	10.5	534.2	19.6	476.9	94.2	547.8	10.5	114.9
550.6	14.4	553.3	14.3	564.2	42.2	550.6	14.4	97.6
551.3	16.4	560.2	14.7	596.2	31.4	551.3	16.4	92.5
558.3	10.3	549.6	15.4	513.6	67.6	558.3	10.3	108.7
585.4	5.8	591.2	7.1	613.3	25.8	585.4	5.8	95.4
596.6	4.8	601.9	5.7	622.1	20.2	596.6	4.8	95.9
601.6	11.2	596.4	10.7	576.3	29.7	601.6	11.2	104.4
603.3	8.8	607.4	14.7	622.9	60.9	603.3	8.8	96.8
608.7	15.0	603.6	13.5	584.5	31.7	608.7	15.0	104.1
611.8	4.9	612.3	10.4	614.0	45.5	611.8	4.9	99.6
612.0	9.9	623.6	29.2	666.0	129.2	612.0	9.9	91.9
617.2	13.2	619.7	36.6	628.6	162.9	617.2	13.2	98.2
617.5	8.3	619.7	8.5	627.6	25.5	617.5	8.3	98.4
620.0	10.3	632.2	9.8	676.2	24.4	620.0	10.3	91.7
621.0	9.8	641.9	25.5	716.4	108.2	621.0	9.8	86.7
622.1	9.6	650.5	9.4	750.3	22.8	622.1	9.6	82.9
642.2	21.2	640.0	44.1	632.2	185.9	642.2	21.2	101.6
739.0	8.1	756.4	22.8	807.9	86.2	739.0	8.1	91.5
761.5	6.6	752.6	16.8	726.3	64.1	761.5	6.6	104.8
761.6	9.2	762.3	8.9	764.5	22.3	761.6	9.2	99.6
812.1	8.3	807.2	13.3	793.5	44.4	812.1	8.3	102.4
832.6	6.7	830.0	6.0	823.0	13.2	832.6	6.7	101.2
833.8	16.7	826.6	19.0	807.2	54.1	833.8	16.7	103.3
1554.1	56.4	1698.2	33.7	1880.9	3.2	1880.9	3.2	82.6
2123.2	89.0	2099.2	44.2	2075.8	13.3	2075.8	13.3	102.3
2706.4	23.0	2698.0	10.2	2691.6	4.6	2691.6	4.6	100.5
2811.1	24.9	2823.8	11.8	2832.9	9.4	2832.9	9.4	99.2

Loiras (LRS) detrital zircon raw data.

		Apparent ages (Ma)						
206Pb*	±	207Pb*	±	206Pb*	±	Best age	±	Conc
238U*	(Ma)	235U	(Ma)	207Pb*	(Ma)	(Ma)	(Ma)	(%)
297.5	7.7	321.4	32.0	499.0	249.4	297.5	7.7	NA
299.1	12.4	296.9	21.7	280.3	166.9	299.1	12.4	NA
300.9	4.3	285.7	21.1	163.1	195.1	300.9	4.3	NA
301.5	2.6	304.4	7.2	326.4	58.5	301.5	2.6	NA
302.0	5.2	308.3	12.2	356.2	95.5	302.0	5.2	NA
302.1	2.5	303.1	7.4	310.8	61.4	302.1	2.5	NA
303.2	4.8	302.0	23.8	292.5	205.0	303.2	4.8	NA
304.8	7.4	305.5	12.0	311.4	86.2	304.8	7.4	NA
306.4	4.9	316.0	14.2	387.0	111.7	306.4	4.9	NA
307.1	4.1	308.4	10.4	318.5	83.2	307.1	4.1	NA
313.4	6.2	320.0	26.7	368.2	215.0	313.4	6.2	NA
319.8	7.2	336.7	18.5	455.3	134.2	319.8	7.2	NA
324.5	5.8	316.6	11.2	259.0	84.7	324.5	5.8	NA
325.0	7.3	315.2	10.8	243.5	75.3	325.0	7.3	NA
334.2	8.1	341.1	11.1	388.4	65.7	334.2	8.1	NA
334.4	2.9	334.3	12.4	333.6	96.9	334.4	2.9	NA
339.0	5.1	337.9	14.1	331.0	105.7	339.0	5.1	NA
339.1	5.4	338.5	8.1	334.8	51.5	339.1	5.4	NA
356.1	7.6	388.0	28.6	582.4	186.9	356.1	7.6	NA
360.6	5.8	371.2	25.9	437.9	182.0	360.6	5.8	NA
360.7	7.6	365.3	17.8	394.4	120.7	360.7	7.6	NA
365.8	2.4	368.3	11.1	383.8	79.5	365.8	2.4	NA
375.7	10.9	380.1	20.8	407.3	130.5	375.7	10.9	NA
405.2	11.4	407.7	10.7	422.2	28.9	405.2	11.4	96.0
416.4	5.7	423.7	8.1	463.8	41.3	416.4	5.7	89.8
450.7	5.9	451.5	9.4	455.6	48.9	450.7	5.9	98.9
456.8	10.5	455.7	13.8	450.2	64.3	456.8	10.5	101.5
459.9	15.4	453.0	20.7	417.7	100.2	459.9	15.4	110.1
462.0	6.4	465.0	7.2	479.4	28.7	462.0	6.4	96.4
463.5	10.0	463.2	10.7	462.0	40.5	463.5	10.0	100.3
463.9	10.5	465.8	14.6	475.3	69.5	463.9	10.5	97.6
464.6	3.7	464.1	9.1	461.6	51.1	464.6	3.7	100.7
465.2	7.8	456.8	13.7	414.6	73.3	465.2	7.8	112.2
465.8	15.6	465.7	18.1	465.4	75.1	465.8	15.6	100.1
473.0	11.0	482.6	16.5	528.3	77.8	473.0	11.0	89.5
478.4	5.2	472.5	10.0	443.7	53.1	478.4	5.2	107.8
479.4	9.1	486.8	12.2	522.0	54.0	479.4	9.1	91.8
482.8	7.4	471.1	21.8	414.6	124.1	482.8	7.4	116.4
493.1	36.4	549.6	64.7	791.1	277.3	493.1	36.4	62.3
513.1	8.9	515.8	27.0	527.6	140.8	513.1	8.9	97.3
542.0	19.2	552.4	16.5	595.2	25.9	542.0	19.2	91.1

568.3	47.8	582.3	47.2	637.4	129.0	568.3	47.8	89.2
571.8	11.8	573.4	12.7	579.6	42.1	571.8	11.8	98.7
574.7	6.5	580.8	7.2	604.6	24.4	574.7	6.5	95.1
593.3	14.6	605.8	28.9	653.1	124.4	593.3	14.6	90.8
596.3	8.6	601.6	21.3	621.4	96.1	596.3	8.6	96.0
602.0	5.9	599.1	6.8	587.9	23.7	602.0	5.9	102.4
602.8	6.2	610.3	14.0	638.1	61.4	602.8	6.2	94.5
614.1	8.1	628.7	16.3	681.8	68.1	614.1	8.1	90.1
628.1	12.0	625.4	19.6	615.6	79.5	628.1	12.0	102.0
628.7	10.7	642.8	22.2	692.9	91.7	628.7	10.7	90.7
640.6	16.1	634.8	33.5	614.3	142.3	640.6	16.1	104.3
645.2	25.6	664.6	31.1	730.8	102.1	645.2	25.6	88.3
650.8	13.3	649.9	14.6	646.8	46.0	650.8	13.3	100.6
665.8	8.2	662.2	16.0	649.9	64.7	665.8	8.2	102.4
669.6	6.0	664.2	15.0	645.9	63.1	669.6	6.0	103.7
686.2	4.5	704.5	11.5	763.2	45.6	686.2	4.5	89.9
695.3	6.2	698.7	8.2	709.5	28.3	695.3	6.2	98.0
697.6	9.9	708.9	8.7	744.9	17.3	697.6	9.9	93.7
697.8	7.3	702.8	9.9	718.8	34.0	697.8	7.3	97.1
711.3	13.5	714.0	17.8	722.4	60.3	711.3	13.5	98.5
711.4	7.3	712.4	9.5	715.6	32.1	711.4	7.3	99.4
721.5	10.5	723.1	21.7	728.1	82.9	721.5	10.5	99.1
760.6	12.3	775.1	18.9	817.3	63.3	760.6	12.3	93.1
768.0	27.0	808.7	31.4	922.4	86.7	768.0	27.0	83.3
770.1	6.0	771.9	14.4	776.9	53.3	770.1	6.0	99.1
781.0	7.2	779.0	7.2	773.2	18.4	781.0	7.2	101.0
788.5	16.4	809.4	13.4	867.3	19.5	788.5	16.4	90.9
796.2	16.7	805.6	25.5	832.0	83.5	796.2	16.7	95.7
796.8	8.0	806.0	20.2	831.4	72.5	796.8	8.0	95.8
857.5	11.4	853.2	16.6	842.2	52.2	857.5	11.4	101.8
867.9	8.5	856.6	18.8	827.2	64.3	867.9	8.5	104.9
869.0	28.3	866.7	21.7	860.7	27.8	869.0	28.3	101.0
951.4	10.5	939.1	18.2	910.1	56.2	910.1	56.2	104.5
892.0	15.1	900.7	11.7	922.0	15.1	922.0	15.1	96.7
959.0	20.1	950.1	14.9	929.5	18.2	929.5	18.2	103.2
955.8	31.9	950.3	24.3	937.4	33.4	937.4	33.4	102.0
1037.7	18.0	1023.4	32.5	993.0	95.1	993.0	95.1	104.5
868.7	17.7	905.1	22.3	994.9	61.5	994.9	61.5	87.3
997.4	31.8	1006.0	23.7	1024.8	28.5	1024.8	28.5	97.3
1096.7	11.0	1094.8	9.2	1091.0	16.8	1091.0	16.8	100.5
1211.1	17.5	1210.7	12.4	1210.0	14.9	1210.0	14.9	100.1
1769.7	21.9	1768.4	12.7	1766.8	9.8	1766.8	9.8	100.2
1821.0	38.3	1802.7	21.7	1781.7	16.0	1781.7	16.0	102.2
1894.2	17.6	1883.9	11.6	1872.6	14.8	1872.6	14.8	101.2
1793.2	50.6	1874.1	28.4	1964.9	13.9	1964.9	13.9	91.3
1955.0	17.4	1962.6	10.2	1970.6	9.9	1970.6	9.9	99.2
2067.5	26.7	2070.2	13.8	2072.8	7.2	2072.8	7.2	99.7
2108.8	44.7	2106.8	22.4	2104.9	7.9	2104.9	7.9	100.2
2101.1	49.5	2139.0	26.8	2175.6	20.8	2175.6	20.8	96.6
2346.6	58.7	2482.5	27.8	2595.6	5.2	2595.6	5.2	90.4

2991.7	29.9	2984.9	12.3	2980.3	4.9	2980.3	4.9	100.4
--------	------	--------	------	--------	-----	--------	-----	-------

Rabejac (RAB) detrital zircon raw data.

		Apparent ages (Ma)						
206Pb*	±	207Pb*	±	206Pb*	±	Best age	±	Conc
238U*	(Ma)	235U	(Ma)	207Pb*	(Ma)	(Ma)	(Ma)	(%)
285.5	4.3	290.6	30.9	332.0	275.9	285.5	4.3	NA
286.1	3.3	285.3	10.1	279.0	88.6	286.1	3.3	NA
286.7	6.2	284.7	15.5	268.0	133.6	286.7	6.2	NA
286.9	4.1	293.4	31.5	345.5	278.3	286.9	4.1	NA
287.6	2.3	290.0	8.3	309.8	72.5	287.6	2.3	NA
289.3	1.7	285.4	9.1	253.0	83.4	289.3	1.7	NA
289.7	3.1	291.6	6.9	306.4	57.3	289.7	3.1	NA
289.7	3.6	288.8	9.0	281.2	76.9	289.7	3.6	NA
291.4	2.2	291.8	4.7	294.6	38.6	291.4	2.2	NA
291.5	1.8	291.7	4.0	293.2	32.8	291.5	1.8	NA
292.1	3.5	297.0	12.1	336.5	102.3	292.1	3.5	NA
292.6	2.9	294.3	9.6	307.3	82.2	292.6	2.9	NA
294.4	4.2	294.5	10.1	295.5	83.9	294.4	4.2	NA
294.6	6.1	283.2	21.9	190.6	200.3	294.6	6.1	NA
294.9	2.3	295.8	6.5	303.1	54.5	294.9	2.3	NA
295.1	8.3	286.2	19.4	214.2	167.4	295.1	8.3	NA
296.9	7.2	299.7	14.7	321.9	115.6	296.9	7.2	NA
296.9	2.6	292.2	8.2	254.8	71.3	296.9	2.6	NA
298.9	2.7	295.8	13.7	271.2	120.3	298.9	2.7	NA
300.8	2.5	295.7	11.1	255.4	97.3	300.8	2.5	NA
301.5	4.3	290.2	13.7	200.5	121.7	301.5	4.3	NA
301.9	2.4	302.5	4.2	307.0	31.8	301.9	2.4	NA
303.6	4.0	298.2	15.6	256.0	135.2	303.6	4.0	NA
303.6	2.8	302.5	6.9	294.6	56.2	303.6	2.8	NA
304.3	1.6	305.9	8.7	318.4	73.6	304.3	1.6	NA
304.9	3.3	328.7	29.0	500.8	226.5	304.9	3.3	NA
305.1	1.8	306.7	16.3	318.5	139.5	305.1	1.8	NA
305.2	2.2	306.9	7.2	320.0	59.0	305.2	2.2	NA
306.0	3.6	302.2	10.4	272.8	87.3	306.0	3.6	NA
306.9	2.0	309.2	9.7	326.0	81.5	306.9	2.0	NA
308.3	3.3	306.3	7.9	291.5	63.8	308.3	3.3	NA
308.7	4.0	310.9	18.9	327.7	157.7	308.7	4.0	NA
310.5	7.2	293.7	35.0	162.7	317.1	310.5	7.2	NA
310.6	2.9	312.7	13.4	328.5	111.2	310.6	2.9	NA
313.5	7.1	334.9	18.4	485.7	132.8	313.5	7.1	NA
314.2	3.5	310.7	11.6	284.8	95.9	314.2	3.5	NA
315.8	2.0	325.1	13.5	392.5	107.6	315.8	2.0	NA
317.0	2.0	318.4	4.3	328.4	32.6	317.0	2.0	NA
336.0	5.6	335.9	22.1	335.4	170.6	336.0	5.6	NA

353.9	6.8	352.6	9.0	343.7	52.1	353.9	6.8	NA
451.0	3.6	449.6	5.3	442.4	26.8	451.0	3.6	101.9
453.2	2.3	457.7	5.9	480.5	33.5	453.2	2.3	94.3
453.7	3.9	466.2	18.4	528.6	106.2	453.7	3.9	85.8
454.8	5.0	458.4	7.3	476.7	35.8	454.8	5.0	95.4
460.6	4.2	468.1	15.4	504.9	87.9	460.6	4.2	91.2
465.0	3.3	467.8	12.4	481.6	71.1	465.0	3.3	96.6
465.2	5.0	474.5	19.6	519.5	110.9	465.2	5.0	89.6
468.5	5.7	464.2	10.4	442.8	55.6	468.5	5.7	105.8
493.1	4.8	503.8	12.8	552.7	66.5	493.1	4.8	89.2
498.3	15.8	584.1	20.0	933.4	63.0	498.3	15.8	53.4
541.5	4.8	536.4	51.9	514.9	273.5	541.5	4.8	105.2
574.7	4.6	577.4	12.2	588.0	57.2	574.7	4.6	97.7
589.3	6.8	589.7	13.3	591.4	58.8	589.3	6.8	99.6
595.0	14.5	570.1	52.6	471.8	261.2	595.0	14.5	126.1
607.2	12.9	609.0	21.0	615.9	86.5	607.2	12.9	98.6
618.0	5.8	626.8	13.4	658.5	57.9	618.0	5.8	93.9
618.9	6.9	626.4	21.5	653.8	95.3	618.9	6.9	94.7
634.6	3.8	637.7	13.7	649.0	60.6	634.6	3.8	97.8
634.8	4.8	637.1	6.2	645.0	22.4	634.8	4.8	98.4
640.9	3.6	640.6	8.3	639.4	35.6	640.9	3.6	100.2
643.0	5.4	642.8	10.4	642.2	42.9	643.0	5.4	100.1
648.4	5.4	642.8	8.9	623.0	35.5	648.4	5.4	104.1
649.0	5.6	652.8	8.7	666.1	33.3	649.0	5.6	97.4
652.3	4.0	648.8	6.2	636.5	23.9	652.3	4.0	102.5
652.4	5.2	654.8	11.0	663.0	45.3	652.4	5.2	98.4
656.8	4.3	654.6	6.6	647.0	25.6	656.8	4.3	101.5
663.2	21.4	689.3	53.4	775.2	213.0	663.2	21.4	85.6
683.0	11.1	681.9	11.7	678.4	34.8	683.0	11.1	100.7
687.3	9.2	691.5	12.6	705.1	44.0	687.3	9.2	97.5
726.2	5.9	719.2	14.9	697.4	58.7	726.2	5.9	104.1
734.4	9.2	737.5	13.1	746.9	44.9	734.4	9.2	98.3
761.2	7.8	768.2	13.3	788.5	46.5	761.2	7.8	96.5
773.6	5.2	776.4	17.1	784.4	64.3	773.6	5.2	98.6
848.1	8.6	846.1	20.1	840.9	69.4	848.1	8.6	100.9
996.9	11.5	994.4	9.7	988.8	18.3	988.8	18.3	100.8
958.5	9.4	977.3	17.3	1019.8	51.5	1019.8	51.5	94.0
1036.6	7.7	1033.4	8.7	1026.6	21.7	1026.6	21.7	101.0
1054.6	4.5	1054.2	8.9	1053.2	25.7	1053.2	25.7	100.1
1054.8	7.0	1056.8	12.8	1061.0	36.6	1061.0	36.6	99.4
1025.4	14.9	1038.4	59.9	1065.8	182.5	1065.8	182.	96.2
999.6	14.2	1049.5	12.6	1155.0	23.1	1155.0	23.1	86.5
1210.4	8.1	1218.1	6.8	1231.8	11.9	1231.8	11.9	98.3
1790.9	33.5	1813.8	27.5	1840.2	44.3	1840.2	44.3	97.3
1896.9	13.2	1892.3	13.3	1887.3	23.9	1887.3	23.9	100.5
1767.3	23.2	1848.2	23.3	1940.4	40.8	1940.4	40.8	91.1
2002.0	8.1	2000.6	5.4	1999.1	7.0	1999.1	7.0	100.1
2041.6	17.8	2030.1	11.0	2018.4	12.9	2018.4	12.9	101.1
1975.8	16.2	2017.0	12.1	2059.4	17.7	2059.4	17.7	95.9
2084.6	9.4	2076.6	5.6	2068.6	6.3	2068.6	6.3	100.8

2162.7	15.4	2149.4	9.5	2136.7	11.6	2136.7	11.6	101.2
2238.3	42.3	2225.6	20.3	2214.0	5.0	2214.0	5.0	101.1
2441.5	15.9	2423.7	7.5	2408.7	3.5	2408.7	3.5	101.4
2760.6	33.0	2722.6	16.3	2694.5	14.9	2694.5	14.9	102.5
2579.6	26.9	2669.8	13.4	2738.8	10.7	2738.8	10.7	94.2
2890.3	18.3	2883.7	9.8	2879.1	10.7	2879.1	10.7	100.4
2502.5	57.7	2721.6	26.5	2888.5	4.5	2888.5	4.5	86.6
2972.7	37.0	2952.0	15.1	2938.0	3.7	2938.0	3.7	101.2

Lower Salagou (L_SAL) detrital zircon raw data.

Apparent ages (Ma)								
206Pb*	±	207Pb*	±	206Pb*	±	Best age	±	Conc
238U*	(Ma)	235U	(Ma)	207Pb*	(Ma)	(Ma)	(Ma)	(%)
220.1	16.0	243.9	20.4	479.3	127.8	220.1	16.0	NA
241.9	16.3	272.0	20.7	539.5	116.0	241.9	16.3	NA
272.5	17.2	279.7	16.8	340.5	52.2	272.5	17.2	NA
283.2	14.1	290.7	24.3	351.9	184.9	283.2	14.1	NA
285.0	3.4	271.9	11.1	160.7	105.5	285.0	3.4	NA
286.3	4.3	274.6	13.6	175.7	127.2	286.3	4.3	NA
290.5	2.7	292.9	6.6	312.1	54.5	290.5	2.7	NA
296.2	2.4	298.2	4.5	314.2	35.3	296.2	2.4	NA
301.8	9.5	309.4	13.6	367.4	89.5	301.8	9.5	NA
301.8	5.2	295.7	17.6	247.7	153.1	301.8	5.2	NA
303.0	3.5	293.1	25.0	215.0	225.9	303.0	3.5	NA
309.8	7.4	340.0	27.0	551.8	197.3	309.8	7.4	NA
312.5	5.5	307.1	20.0	266.5	168.1	312.5	5.5	NA
312.7	3.0	314.6	7.5	328.4	58.7	312.7	3.0	NA
313.3	3.2	318.7	7.4	357.9	56.4	313.3	3.2	NA
313.4	7.2	303.9	21.7	231.2	183.3	313.4	7.2	NA
425.7	18.7	447.2	18.4	559.3	49.8	425.7	18.7	76.1
448.1	28.5	458.4	27.2	510.5	73.5	448.1	28.5	87.8
452.5	7.0	453.1	9.8	455.8	47.6	452.5	7.0	99.3
454.8	3.2	452.8	12.4	442.7	73.8	454.8	3.2	102.7
457.6	5.3	451.1	10.6	418.2	59.3	457.6	5.3	109.4
459.3	6.2	449.3	13.4	398.1	76.6	459.3	6.2	115.4
459.4	4.9	448.2	14.2	390.8	84.1	459.4	4.9	117.5
459.5	3.2	454.5	8.6	429.5	49.7	459.5	3.2	107.0
460.1	4.6	460.3	9.7	461.5	53.4	460.1	4.6	99.7
461.3	5.0	452.5	17.3	407.9	102.7	461.3	5.0	113.1
461.6	14.4	463.7	16.9	474.0	70.6	461.6	14.4	97.4
462.2	7.4	451.4	31.3	397.1	189.0	462.2	7.4	116.4
462.3	12.2	451.7	16.7	398.4	82.3	462.3	12.2	116.0
462.3	5.1	466.6	10.1	488.1	53.7	462.3	5.1	94.7
463.3	24.0	455.0	32.7	413.2	159.2	463.3	24.0	112.1
463.4	6.5	476.2	10.5	538.5	51.4	463.4	6.5	86.1

463.5	4.5	459.7	10.3	440.8	57.6	463.5	4.5	105.2
464.2	8.3	469.3	19.2	494.3	105.2	464.2	8.3	93.9
464.9	6.0	467.0	10.0	477.2	51.1	464.9	6.0	97.4
465.0	9.7	473.1	35.6	512.2	201.8	465.0	9.7	90.8
465.1	6.2	451.2	25.5	381.2	154.6	465.1	6.2	122.0
465.2	7.5	468.5	12.9	484.8	66.4	465.2	7.5	95.9
465.4	4.1	465.1	8.4	464.0	45.5	465.4	4.1	100.3
465.6	3.9	456.6	14.2	411.4	84.1	465.6	3.9	113.2
468.7	7.8	468.2	8.8	465.9	34.8	468.7	7.8	100.6
471.1	5.7	474.3	9.7	489.9	48.9	471.1	5.7	96.2
472.0	6.9	475.9	10.0	494.9	47.7	472.0	6.9	95.4
479.2	6.8	471.6	12.2	434.7	63.9	479.2	6.8	110.2
487.6	36.1	473.1	36.3	403.6	128.8	487.6	36.1	120.8
530.4	10.7	569.5	35.5	728.9	166.9	530.4	10.7	72.8
533.0	20.5	553.6	18.5	639.1	35.2	533.0	20.5	83.4
544.1	13.8	541.6	17.9	531.2	73.3	544.1	13.8	102.4
550.9	3.5	555.7	6.5	575.3	29.3	550.9	3.5	95.8
555.3	18.9	557.3	28.0	565.9	119.5	555.3	18.9	98.1
556.0	18.1	557.6	23.7	564.1	94.5	556.0	18.1	98.6
556.2	8.7	558.9	30.2	569.8	149.0	556.2	8.7	97.6
564.2	23.7	563.8	20.2	562.5	35.1	564.2	23.7	100.3
578.2	10.9	564.9	24.4	511.7	116.2	578.2	10.9	113.0
582.6	10.4	588.4	40.7	610.7	193.3	582.6	10.4	95.4
591.0	13.7	613.2	52.1	696.2	235.8	591.0	13.7	84.9
594.1	13.2	603.3	17.4	637.9	65.7	594.1	13.2	93.1
594.9	11.1	594.1	16.8	591.0	69.4	594.9	11.1	100.6
601.3	7.2	598.9	24.2	589.8	112.6	601.3	7.2	101.9
616.7	6.3	611.7	17.4	593.5	78.5	616.7	6.3	103.9
618.7	52.9	628.1	51.1	662.2	132.8	618.7	52.9	93.4
643.2	6.4	642.3	34.6	638.8	154.7	643.2	6.4	100.7
678.4	7.0	671.2	12.0	647.2	47.1	678.4	7.0	104.8
690.4	8.5	683.3	22.6	660.0	93.5	690.4	8.5	104.6
692.3	28.4	715.9	23.4	790.6	29.8	692.3	28.4	87.6
773.2	39.1	820.3	51.2	950.4	150.1	773.2	39.1	81.3
776.9	7.9	773.9	7.6	765.1	18.9	776.9	7.9	101.5
852.8	22.4	848.1	21.0	835.8	48.5	852.8	22.4	102.0
878.2	58.3	877.6	41.8	876.1	11.3	878.2	58.3	100.2
975.1	12.3	964.8	14.6	941.5	39.3	941.5	39.3	103.6
976.7	7.3	966.3	14.6	942.8	45.0	942.8	45.0	103.6
1055.5	17.8	1044.5	40.7	1021.6	120.8	1021.6	120.8	103.3
1028.8	10.9	1027.6	14.4	1024.8	38.7	1024.8	38.7	100.4
1005.9	22.9	1023.0	23.5	1059.7	54.2	1059.7	54.2	94.9
1061.7	10.7	1063.4	10.9	1066.8	24.8	1066.8	24.8	99.5
1413.9	9.1	1403.6	12.9	1388.0	29.5	1388.0	29.5	101.9
1826.2	12.3	1836.7	14.2	1848.5	26.8	1848.5	26.8	98.8
1832.8	16.3	1845.3	9.0	1859.4	4.7	1859.4	4.7	98.6
1867.9	14.3	1874.5	13.3	1881.9	23.0	1881.9	23.0	99.3
1789.7	18.9	1833.4	13.3	1883.4	17.9	1883.4	17.9	95.0
1891.3	16.8	1887.7	9.1	1883.8	5.1	1883.8	5.1	100.4
1777.1	27.0	1852.5	15.3	1938.1	8.4	1938.1	8.4	91.7
1934.2	64.2	1964.3	34.2	1996.2	15.0	1996.2	15.0	96.9

1908.6	38.3	1967.8	21.9	2030.5	17.3	2030.5	17.3	94.0
2054.4	17.1	2061.4	16.1	2068.4	27.2	2068.4	27.2	99.3
1990.1	33.4	2043.6	19.1	2098.1	16.7	2098.1	16.7	94.9
2176.1	20.8	2170.6	10.4	2165.3	4.7	2165.3	4.7	100.5
2314.2	14.3	2369.7	6.8	2417.8	1.7	2417.8	1.7	95.7
2534.5	30.2	2527.1	15.9	2521.1	15.5	2521.1	15.5	100.5
2486.2	53.4	2559.0	24.9	2617.2	10.6	2617.2	10.6	95.0
2672.7	22.4	2697.5	10.9	2716.1	8.6	2716.1	8.6	98.4
2826.2	24.6	2862.0	11.2	2887.3	7.6	2887.3	7.6	97.9
2889.7	93.1	2893.6	43.4	2896.4	34.8	2896.4	34.8	99.8
3149.5	68.8	3208.8	26.9	3246.1	3.0	3246.1	3.0	97.0

Middle Salagou (M_SAL) detrital zircon raw data.

		Apparent ages (Ma)						
206Pb*	±	207Pb*	±	206Pb*	±	Best age	±	Conc
238U*	(Ma)	235U	(Ma)	207Pb*	(Ma)	(Ma)	(Ma)	(%)
283.1	3.4	288.6	8.0	333.4	66.7	283.1	3.4	NA
284.7	2.7	288.2	14.3	316.8	127.8	284.7	2.7	NA
286.4	1.9	286.1	4.5	283.5	38.4	286.4	1.9	NA
286.9	6.2	282.9	21.5	249.8	194.3	286.9	6.2	NA
287.2	2.3	282.0	9.2	239.1	84.3	287.2	2.3	NA
288.5	4.5	283.8	9.2	245.0	77.6	288.5	4.5	NA
290.2	3.5	285.4	14.8	245.9	134.2	290.2	3.5	NA
291.1	5.6	301.5	10.9	382.6	82.7	291.1	5.6	NA
291.8	5.0	293.3	12.2	305.3	101.5	291.8	5.0	NA
294.2	4.2	293.3	10.9	285.9	92.2	294.2	4.2	NA
294.4	2.2	296.9	4.7	316.5	37.4	294.4	2.2	NA
297.8	3.4	298.1	5.0	301.2	35.5	297.8	3.4	NA
301.0	12.5	334.8	34.7	576.9	248.2	301.0	12.5	NA
304.9	7.9	307.2	12.2	324.6	84.7	304.9	7.9	NA
305.0	14.8	304.1	19.5	297.5	126.4	305.0	14.8	NA
306.4	5.7	313.1	10.5	363.7	77.0	306.4	5.7	NA
310.5	5.5	320.5	19.1	393.4	150.7	310.5	5.5	NA
325.2	10.1	333.1	12.6	388.9	69.9	325.2	10.1	NA
337.8	3.9	335.3	8.9	318.1	65.4	337.8	3.9	NA
345.2	3.5	353.0	6.8	404.6	45.2	345.2	3.5	NA
430.4	7.5	442.7	9.5	507.6	42.2	430.4	7.5	84.8
444.6	5.0	444.7	7.7	445.3	39.9	444.6	5.0	99.8
457.2	6.0	457.6	9.0	459.3	45.1	457.2	6.0	99.6
457.5	10.1	458.9	10.9	466.0	41.6	457.5	10.1	98.2
457.6	5.0	459.6	7.4	469.5	36.3	457.6	5.0	97.5
457.6	4.1	455.0	9.9	441.4	56.4	457.6	4.1	103.7
458.3	3.0	461.8	15.3	479.3	89.7	458.3	3.0	95.6
461.1	5.8	464.9	11.1	483.7	59.2	461.1	5.8	95.3
461.6	6.5	460.1	10.0	452.7	50.7	461.6	6.5	102.0

462.0	3.1	457.8	9.0	436.8	51.9	462.0	3.1	105.8
463.3	5.2	461.7	9.7	453.8	52.3	463.3	5.2	102.1
463.7	9.5	464.9	24.9	471.0	140.2	463.7	9.5	98.4
463.9	11.1	468.0	11.1	488.0	35.7	463.9	11.1	95.1
466.1	7.3	492.8	20.0	619.0	104.7	466.1	7.3	75.3
467.5	8.8	467.7	18.2	468.5	98.7	467.5	8.8	99.8
468.2	5.9	472.5	9.9	493.2	50.3	468.2	5.9	94.9
468.4	6.6	468.7	10.6	470.0	53.6	468.4	6.6	99.7
469.7	12.1	471.3	15.9	479.1	71.8	469.7	12.1	98.0
469.8	7.6	470.2	18.9	472.5	104.6	469.8	7.6	99.4
477.9	8.3	485.3	7.8	520.4	19.7	477.9	8.3	91.8
478.4	4.7	482.5	9.5	502.2	49.7	478.4	4.7	95.2
496.9	5.6	525.2	35.7	650.1	185.2	496.9	5.6	76.4
507.1	26.2	515.6	24.7	553.3	63.3	507.1	26.2	91.7
516.8	11.7	498.1	20.9	413.1	106.2	516.8	11.7	125.1
562.8	11.8	555.7	15.2	527.2	61.2	562.8	11.8	106.8
564.4	7.4	567.5	20.9	579.5	100.3	564.4	7.4	97.4
566.0	16.4	572.9	14.3	600.4	27.4	566.0	16.4	94.3
576.8	3.7	579.6	12.7	590.3	60.4	576.8	3.7	97.7
583.8	8.2	566.8	24.4	499.3	119.4	583.8	8.2	116.9
596.2	8.1	612.3	23.3	672.5	104.1	596.2	8.1	88.7
597.1	8.5	594.2	21.3	582.9	97.5	597.1	8.5	102.4
602.7	5.5	608.9	24.5	632.0	113.3	602.7	5.5	95.4
605.3	4.9	608.3	7.4	619.6	29.6	605.3	4.9	97.7
610.3	8.8	611.6	13.1	616.6	52.1	610.3	8.8	99.0
611.6	9.0	614.2	9.2	623.7	27.6	611.6	9.0	98.1
623.4	7.2	626.9	12.1	639.3	49.0	623.4	7.2	97.5
625.6	16.7	638.3	15.6	683.8	37.3	625.6	16.7	91.5
628.5	7.2	633.9	7.8	652.8	24.7	628.5	7.2	96.3
631.5	6.7	626.9	15.0	610.4	64.7	631.5	6.7	103.5
631.7	5.3	624.2	13.0	597.2	57.3	631.7	5.3	105.8
635.6	9.4	633.0	21.0	623.8	90.2	635.6	9.4	101.9
639.3	9.7	642.3	9.2	652.8	23.5	639.3	9.7	97.9
651.8	4.7	648.2	11.0	635.8	46.4	651.8	4.7	102.5
663.4	18.7	688.5	45.5	771.3	181.2	663.4	18.7	86.0
665.1	10.4	668.6	25.3	680.4	104.8	665.1	10.4	97.8
667.4	13.9	662.2	13.2	644.5	34.3	667.4	13.9	103.5
671.8	2.9	673.1	5.0	677.4	19.4	671.8	2.9	99.2
673.2	7.5	671.4	13.6	665.7	53.8	673.2	7.5	101.1
673.6	8.4	669.0	9.9	653.6	32.7	673.6	8.4	103.1
675.6	9.7	672.1	24.8	660.7	103.4	675.6	9.7	102.3
684.2	56.4	679.0	43.9	661.6	36.4	684.2	56.4	103.4
692.3	3.3	689.8	5.5	681.8	21.1	692.3	3.3	101.5
692.9	4.1	693.9	6.6	697.2	24.7	692.9	4.1	99.4
698.0	6.0	690.2	9.0	664.9	33.5	698.0	6.0	105.0
699.1	8.6	698.6	7.8	697.2	18.2	699.1	8.6	100.3
705.0	7.8	716.8	19.7	754.1	77.2	705.0	7.8	93.5
708.4	12.1	742.7	18.1	847.6	60.7	708.4	12.1	83.6
720.1	10.1	717.7	40.5	710.1	164.5	720.1	10.1	101.4
856.3	12.1	870.9	13.8	908.5	37.5	856.3	12.1	94.3
900.2	33.2	889.8	24.9	863.9	30.0	900.2	33.2	104.2

890.3	9.7	904.7	43.4	940.0	146.7	940.0	146.7	94.7
926.4	31.7	937.9	26.0	964.9	43.7	964.9	43.7	96.0
1021.9	8.9	1014.2	22.6	997.6	68.8	997.6	68.8	102.4
1025.8	12.7	1022.5	9.7	1015.4	14.0	1015.4	14.0	101.0
986.9	16.1	998.7	16.3	1024.6	37.8	1024.6	37.8	96.3
1054.5	9.5	1045.1	11.3	1025.6	29.2	1025.6	29.2	102.8
1036.3	15.7	1033.8	16.6	1028.6	39.8	1028.6	39.8	100.7
1072.7	10.8	1064.6	7.9	1048.1	10.3	1048.1	10.3	102.3
911.5	11.2	958.7	32.8	1068.4	103.1	1068.4	103.1	85.3
1050.8	9.3	1057.7	9.4	1072.0	21.3	1072.0	21.3	98.0
1098.8	23.9	1090.8	33.9	1074.9	90.1	1074.9	90.1	102.2
1042.7	14.2	1070.9	24.9	1128.7	68.9	1128.7	68.9	92.4
1880.0	12.9	1868.2	7.6	1855.0	7.5	1855.0	7.5	101.3
1802.0	36.5	1842.0	21.7	1887.4	19.0	1887.4	19.0	95.5
1938.4	22.4	1949.2	12.7	1960.7	10.3	1960.7	10.3	98.9
1961.0	21.8	1968.8	13.5	1977.1	15.5	1977.1	15.5	99.2
1940.3	47.0	1960.5	24.7	1981.9	8.6	1981.9	8.6	97.9
1835.4	35.6	1922.4	21.1	2017.5	17.8	2017.5	17.8	91.0
2133.7	47.6	2138.1	23.7	2142.3	8.2	2142.3	8.2	99.6
1893.7	40.5	2213.9	23.4	2525.1	14.0	2525.1	14.0	75.0
2474.1	32.2	2518.2	15.4	2554.0	8.9	2554.0	8.9	96.9
2195.4	18.0	2414.1	11.6	2604.1	13.4	2604.1	13.4	84.3

Upper Salagou (U_SAL) detrital zircon raw data.

Apparent ages (Ma)								
206Pb*	±	207Pb*	±	206Pb*	±	Best age	±	Conc
238U*	(Ma)	235U	(Ma)	207Pb*	(Ma)	(Ma)	(Ma)	(%)
287.0	10.6	297.7	19.8	381.8	150.5	287.0	10.6	NA
292.6	8.6	298.8	16.0	348.1	122.0	292.6	8.6	NA
293.0	4.0	287.9	11.9	246.9	104.7	293.0	4.0	NA
294.3	3.1	295.1	5.4	302.2	41.2	294.3	3.1	NA
298.2	4.6	296.6	13.8	283.5	117.2	298.2	4.6	NA
303.6	6.1	303.4	9.0	302.0	62.4	303.6	6.1	NA
308.0	6.0	288.6	20.0	134.9	181.3	308.0	6.0	NA
310.6	4.8	313.8	6.5	338.2	41.2	310.6	4.8	NA
316.5	8.4	314.4	10.9	298.2	68.1	316.5	8.4	NA
316.8	14.1	317.6	18.9	323.1	118.6	316.8	14.1	NA
330.2	6.6	331.4	11.3	340.2	77.5	330.2	6.6	NA
408.8	36.1	460.8	35.1	729.3	56.2	408.8	36.1	56.0
422.0	22.8	437.4	23.6	519.7	78.8	422.0	22.8	81.2
434.0	5.2	441.7	9.3	481.9	50.4	434.0	5.2	90.1
438.8	6.4	438.8	13.7	439.0	78.5	438.8	6.4	100.0
446.6	10.3	455.2	11.1	498.5	40.8	446.6	10.3	89.6
456.6	4.9	438.7	29.3	345.8	184.9	456.6	4.9	132.0
460.9	4.7	465.7	11.8	489.3	65.6	460.9	4.7	94.2

462.1	3.4	463.8	5.9	472.6	30.9	462.1	3.4	97.8
466.5	6.3	462.5	12.4	442.8	67.7	466.5	6.3	105.4
466.6	6.4	461.8	18.2	438.0	104.7	466.6	6.4	106.5
469.0	20.8	471.6	19.3	484.1	50.3	469.0	20.8	96.9
470.0	4.4	470.3	22.6	472.1	131.4	470.0	4.4	99.5
475.5	15.1	473.8	17.9	465.8	75.4	475.5	15.1	102.1
481.2	3.5	480.4	7.8	476.8	41.9	481.2	3.5	100.9
481.3	7.5	477.9	13.3	461.4	68.5	481.3	7.5	104.3
481.3	4.8	482.9	19.4	490.2	109.2	481.3	4.8	98.2
490.4	9.3	494.0	12.1	510.6	52.2	490.4	9.3	96.0
505.0	5.5	518.6	8.9	579.1	40.9	505.0	5.5	87.2
506.5	13.2	496.5	15.0	450.4	59.6	506.5	13.2	112.5
517.7	26.3	527.2	25.1	568.9	66.6	517.7	26.3	91.0
549.0	9.0	556.3	16.6	586.4	75.3	549.0	9.0	93.6
566.9	15.8	563.6	20.7	550.3	83.2	566.9	15.8	103.0
587.3	4.6	586.1	5.9	581.4	22.6	587.3	4.6	101.0
593.0	10.0	588.6	16.6	571.9	71.5	593.0	10.0	103.7
601.7	5.6	598.6	5.4	587.0	15.3	601.7	5.6	102.5
604.0	8.7	608.9	17.2	627.0	74.1	604.0	8.7	96.3
606.3	4.4	602.3	14.1	587.1	65.5	606.3	4.4	103.3
609.3	22.9	613.9	24.4	630.7	75.8	609.3	22.9	96.6
610.8	4.4	607.9	7.0	597.0	28.9	610.8	4.4	102.3
612.9	29.4	610.5	25.5	601.8	50.7	612.9	29.4	101.8
624.2	9.2	622.4	13.0	615.9	49.9	624.2	9.2	101.4
624.8	6.4	630.9	6.6	653.1	19.8	624.8	6.4	95.7
626.0	7.5	621.0	22.5	602.6	101.4	626.0	7.5	103.9
629.1	4.9	632.5	12.1	644.8	52.3	629.1	4.9	97.6
633.1	9.1	635.8	19.3	645.2	81.4	633.1	9.1	98.1
634.7	5.8	626.4	11.8	596.9	50.7	634.7	5.8	106.3
635.0	9.6	639.4	19.4	655.0	80.7	635.0	9.6	97.0
636.3	12.0	634.4	19.3	627.6	77.0	636.3	12.0	101.4
642.2	6.1	645.3	8.2	656.1	30.1	642.2	6.1	97.9
643.4	15.7	640.7	24.1	631.0	94.6	643.4	15.7	102.0
647.3	39.6	626.3	45.7	551.0	160.9	647.3	39.6	117.5
654.2	7.9	659.4	10.2	677.1	36.1	654.2	7.9	96.6
656.5	8.9	654.4	8.9	647.4	25.3	656.5	8.9	101.4
656.6	4.7	647.6	7.8	615.9	31.4	656.6	4.7	106.6
658.9	6.2	656.7	11.7	649.3	47.5	658.9	6.2	101.5
660.0	20.2	676.7	41.0	732.7	162.0	660.0	20.2	90.1
668.4	21.6	663.1	18.7	645.3	38.7	668.4	21.6	103.6
671.6	4.9	665.3	14.3	644.0	60.7	671.6	4.9	104.3
674.8	55.2	676.1	44.0	680.5	49.1	674.8	55.2	99.2
675.2	6.7	698.8	22.1	775.7	89.6	675.2	6.7	87.0
688.4	6.2	682.0	10.4	660.8	39.9	688.4	6.2	104.2
693.1	9.3	698.0	36.0	713.8	148.5	693.1	9.3	97.1
701.8	7.1	704.9	11.7	714.8	43.3	701.8	7.1	98.2
723.5	54.9	739.4	43.2	787.9	38.3	723.5	54.9	91.8
740.3	13.3	744.1	15.4	755.6	46.5	740.3	13.3	98.0
757.6	9.1	746.3	20.4	712.3	77.6	757.6	9.1	106.4
777.1	27.6	815.0	27.4	920.2	63.8	777.1	27.6	84.4
778.6	45.2	793.3	34.3	834.6	19.3	778.6	45.2	93.3

782.2	12.0	779.5	11.5	771.6	28.7	782.2	12.0	101.4
792.6	11.7	795.0	11.3	801.7	27.5	792.6	11.7	98.9
804.2	17.7	804.0	44.9	803.3	162.1	804.2	17.7	100.1
832.2	24.2	836.2	21.6	846.8	45.3	832.2	24.2	98.3
850.0	12.9	845.7	11.7	834.6	26.1	850.0	12.9	101.8
897.7	57.8	901.9	42.8	912.0	39.5	912.0	39.5	98.4
955.0	9.2	945.7	8.4	924.1	18.1	924.1	18.1	103.3
959.9	11.9	951.7	22.1	932.8	68.1	932.8	68.1	102.9
902.2	24.1	913.2	18.5	940.0	23.2	940.0	23.2	96.0
920.9	16.8	932.9	24.5	961.5	71.5	961.5	71.5	95.8
967.2	29.3	975.3	24.3	993.6	42.5	993.6	42.5	97.3
1003.3	9.2	1002.9	14.8	1001.9	42.5	1001.9	42.5	100.1
976.6	19.0	985.4	15.3	1005.0	24.8	1005.0	24.8	97.2
993.9	25.4	1001.6	20.8	1018.3	35.2	1018.3	35.2	97.6
1075.6	9.8	1066.7	8.5	1048.5	16.8	1048.5	16.8	102.6
1056.8	14.6	1054.3	13.5	1049.2	28.7	1049.2	28.7	100.7
1036.8	9.9	1041.9	20.2	1052.5	58.7	1052.5	58.7	98.5
1342.0	23.1	1440.3	15.5	1588.5	12.0	1588.5	12.0	84.5
1627.1	37.3	1663.9	21.5	1710.8	7.0	1710.8	7.0	95.1
1304.9	29.0	1493.3	20.3	1772.1	15.4	1772.1	15.4	73.6
1769.8	45.6	1822.5	26.1	1883.2	16.2	1883.2	16.2	94.0
1937.3	20.0	1914.5	11.0	1889.8	8.2	1889.8	8.2	102.5
1901.1	16.3	1933.3	9.2	1968.0	7.0	1968.0	7.0	96.6
1976.5	63.8	2003.1	33.7	2030.6	16.1	2030.6	16.1	97.3
2074.8	18.5	2075.5	9.5	2076.1	4.2	2076.1	4.2	99.9
2086.1	20.2	2095.7	12.1	2105.0	13.2	2105.0	13.2	99.1
2107.7	15.1	2112.7	9.5	2117.5	11.5	2117.5	11.5	99.5
2604.2	31.2	2618.8	14.0	2630.2	5.3	2630.2	5.3	99.0
2573.6	58.2	2698.0	32.1	2792.4	33.0	2792.4	33.0	92.2
2964.2	31.1	2935.2	12.7	2915.4	2.6	2915.4	2.6	101.7
2989.8	20.6	3018.1	8.5	3037.1	3.1	3037.1	3.1	98.4

Table D.— Detrital modes of detrital zircon samples from Lodève Basin sandstones.

<i>Formation</i>	XDM N=3	PAB N=3	HOU N=2	USCL N=4	RAB N=2	L_SAL N=4	U_SAL N=3
<i>Grains</i>							
Qm	216	442	377	606	340	414	460
Km	1	0	220	341	47	10	2
Pm	19	164	73	435	158	603	335
Lm	517	278	28	14	117	262	165
Qr	85	25	0	7	3	30	53
Pr	4	9	0	1	1	49	25
Kr	0	0	0	17	11	10	2
M	69	46	41	14	17	32	8
O	30	9	1	5	11	24	11
Chl	111	11	0	0	0	1	0
Qp (2-3)	36	14	6	49	21	38	24
Qp (>3)	112	194	60	111	70	126	113
chert	0	8	0	0	4	1	2

Notes: Modes based on point counts of 400 QFL framework grains per sample (*N* is the number of samples in each formation group). *Monocrystalline grains:* Qm=Quartz, Km=Potassium Feldspar, Pm=Plagioclase, *Polycrystalline grains:* Qp=Quartz (2-3 grains or >3 grains). Lm=metamorphic lithics. Qr, Pr, and Kr are quartz, plagioclase, and potassium feldspar within a lithic fragment (respectively). *Special grains:* M=mica, O=opaques, Chl=chlorite, and chert. Minerals are identified following the Gazzi-Dickinson method (Ingersoll et al. 1984) with a 63 μm cutoff. Counts were conducted by the same operator on thin sections stained for potassium feldspar. Quartz grain undulosity was recorded, and lithic fragments (Qr, Pr, Kr) were classified as metamorphic or plutonic. See “Methods” section for details.

Table D.— *Feldspar trends and Monocrystalline Quartz (Qm) Undulosity.*

Formation	Feldspar		Qm Undulosity	
	% K-spar	% Plag	% undulose	% non-und
XDM	0	0	67%	33%
XDM	17%	83%	78%	22%
XDM	22%	78%	61%	39%
Avg. XDM	19%	81%	69%	31%
PAB	7%	93%	86%	14%
PAB	10%	90%	79%	21%
PAB	0%	100%	69%	31%
Avg. PAB	6%	94%	78%	22%
HOU	69%	31%	82%	18%
HOU	82%	18%	77%	23%
Avg. HOU	75%	25%	79%	21%
USCL	58%	42%	70%	30%
USCL	56%	44%	89%	11%
USCL	51%	49%	78%	22%
USCL	56%	44%	98%	2%
Avg. USCL	55%	45%	84%	16%
RAB	56%	44%	89%	11%
RAB	2%	98%	69%	31%
Avg. RAB	29%	71%	80%	20%
L_SAL	7%	93%	83%	17%
L_SAL	18%	82%	68%	32%
L_SAL	8%	92%	70%	30%
L_SAL	3%	97%	79%	21%
Avg. L_SAL	9%	91%	76%	24%
U_SAL	19%	81%	90%	10%
U_SAL	11%	89%	77%	23%
U_SAL	0%	100%	69%	31%
Avg. U_SAL	10%	90%	77%	23%

Appendix E: Supplementary Figures and Tables

Sample Number	Population	Genetic Diversity	Mean Size
T3A,B,C	Tritons	0.001 (0.000 - 0.002) (0.000)	10000
R23-A	G. salpax	0.001 (0.000 - 0.002) (0.000)	10000
R23-B	E. salpax	0.001 (0.000 - 0.002) (0.000)	10000
PF	M. salpax	0.001 (0.000 - 0.002) (0.000)	10000
R23-C	D. salpax	0.001 (0.000 - 0.002) (0.000)	10000
R23-D	M. salpax	0.001 (0.000 - 0.002) (0.000)	10000
R23-E	F. salpax	0.001 (0.000 - 0.002) (0.000)	10000
R23-F	G. salpax	0.001 (0.000 - 0.002) (0.000)	10000
R23-G	H. salpax	0.001 (0.000 - 0.002) (0.000)	10000
R23-H	I. salpax	0.001 (0.000 - 0.002) (0.000)	10000
R23-I	J. salpax	0.001 (0.000 - 0.002) (0.000)	10000
R23-J	K. salpax	0.001 (0.000 - 0.002) (0.000)	10000
R23-K	L. salpax	0.001 (0.000 - 0.002) (0.000)	10000
R23-L	M. salpax	0.001 (0.000 - 0.002) (0.000)	10000
R23-M	N. salpax	0.001 (0.000 - 0.002) (0.000)	10000
R23-N	O. salpax	0.001 (0.000 - 0.002) (0.000)	10000
R23-O	P. salpax	0.001 (0.000 - 0.002) (0.000)	10000
R23-P	Q. salpax	0.001 (0.000 - 0.002) (0.000)	10000
R23-Q	R. salpax	0.001 (0.000 - 0.002) (0.000)	10000
R23-R	S. salpax	0.001 (0.000 - 0.002) (0.000)	10000
R23-S	T. salpax	0.001 (0.000 - 0.002) (0.000)	10000
R23-T	U. salpax	0.001 (0.000 - 0.002) (0.000)	10000
R23-U	V. salpax	0.001 (0.000 - 0.002) (0.000)	10000
R23-V	W. salpax	0.001 (0.000 - 0.002) (0.000)	10000
R23-W	X. salpax	0.001 (0.000 - 0.002) (0.000)	10000
R23-X	Y. salpax	0.001 (0.000 - 0.002) (0.000)	10000
R23-Y	Z. salpax	0.001 (0.000 - 0.002) (0.000)	10000

Appendix E-1.— *GPS coordinates of samples included in this study.*

Sample Number	Formation	GPS Coordinates	Grain Size
T3-A,B,C	Triassic	N 43° 39.672', E 003° 13.918'	vf. sand
R23-A	U. Salagou	N 43° 39.386', E 003° 8.794'	cglm
R2B-B	U. Salagou	N 43° 38.689', E 003° 14.108'	c. sand
PT	M. Salagou	N 43° 40.48', E 003° 11.067'	mud
R2B-G	Octon Mbr.	N 43° 38.661', E 003° 17.341'	mud
R2B-E	M. Salagou	N 43° 40.064', E 003° 24.516'	mud
R2B-D	L. Salagou	N 43° 40.068', E 003° 24.593'	f. sand
R2B-C	L. Salagou	N 43° 39.461', E 003° 24.434'	mud
R2B-F	Base Salagou	N 43° 41.331', E 003° 24.660'	silt/f. sand
R1G/R1F-A	Rabejac	N 43° 41.277', E 003° 20.302'	cglm/sand
R2-A	Rabejac	N 43° 40.906', E 003° 9.753'	mud
R1F-A	Loiras/Viala	N 43° 42.193', E 003° 20.288'	silt/mud
R1-A	Usclas	N 43° 40.837', E 003° 9.064'	m. sand
R1B-C	Usclas	N 43° 43.931', E 003° 24.833'	m. sand
R1B-B	Usclas	N 43° 42.979', E 003° 23.8'	f. sand
H5B2-A	Houillière	N 43° 40.707', E 003° 6.099'	c. sand
H5B2P-A	Pabau	N 43° 40.679', E 002° 58.618'	sand
H5B1-A	Croix de Mounis	N 43° 40.965', E 002° 8.97'	cglm

Notes: Samples in bold were analyzed for detrital zircon. See Fig. 7 for sample collection localities.

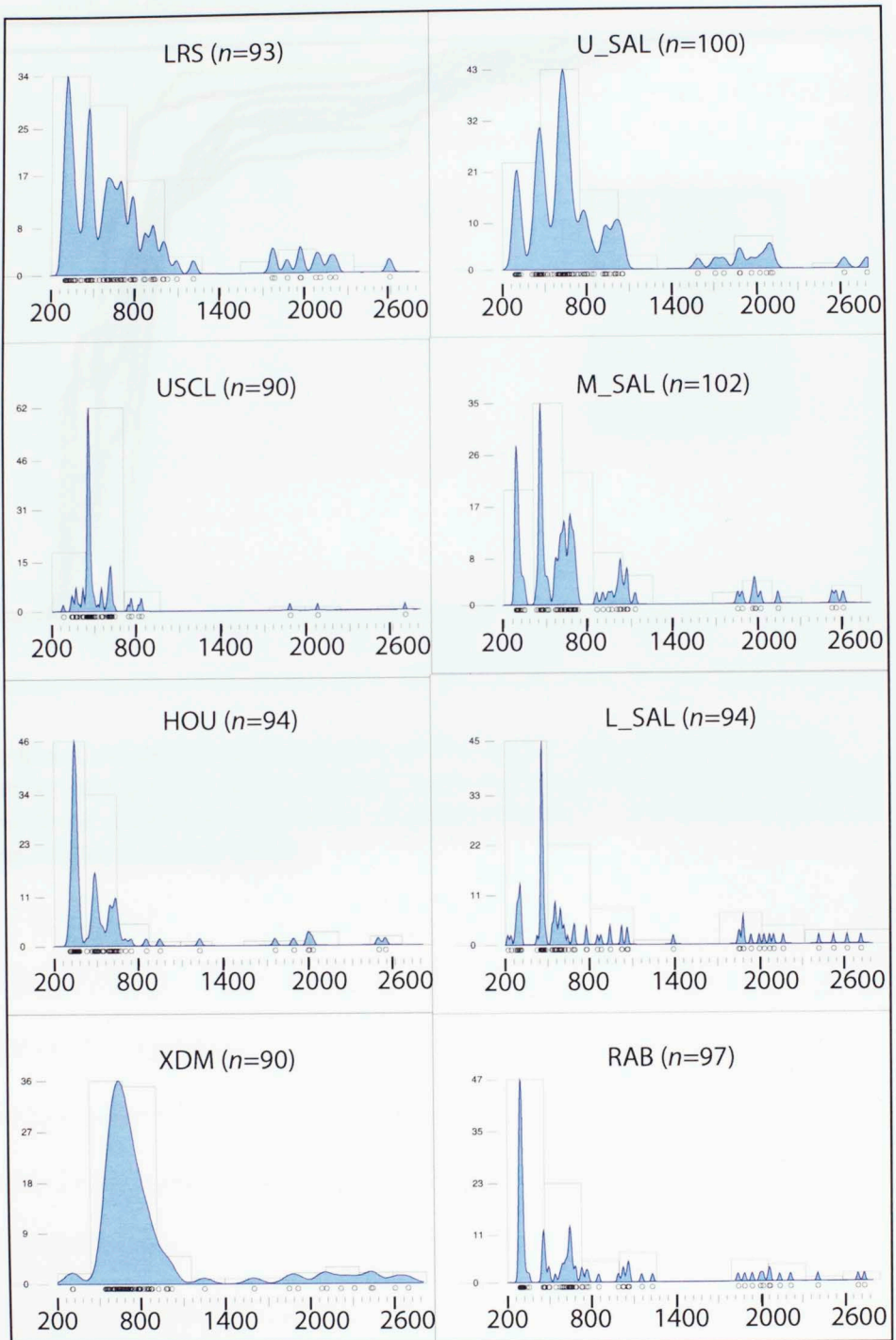
Appendix E-2.— Generalized zircon grain observations from BSE images (Fig. 8) for comparison between samples.

	Color	Shape	Size	Features
U_SAL Upp Salagou Fm (R2B-B)	Colorless	Well to moderately rounded, rare euhedral grains.	Variable, 20-100 μm ; Most 30 μm	Broken, fractures and inclusions are common. Concentric zoning in euhedral grains. Core/rim zones in ~10% grains.
M_SAL Mid Salagou Fm (R2B-G)	Colorless	Well to moderately rounded, rare euhedral grains.	Small ($\leq 100 \mu\text{m}$), but variable. Most 50-60 μm	Concentric zoning apparent in ~20% grains. Few cracks, grains with core/rims very rare.
L_SAL Low Salagou Fm (R2B-F)	Colorless	Well to moderately rounded, ~10% euhedral.	Variable; most 50-70 μm , length euhedral 140 μm	Euhedral grains have concentric zoning. Core/rims are rare. Very few cracks.
RAB Rabejec Fm (R1G/R1F-A)	Colorless	Moderately rounded to commonly euhedral.	Variable, 50-120 μm ; Most 80 μm	Most grains exhibit distinct zoning, and ~50% show core/rim zones. Cracks rare, especially compared to other units.
LRS Loiras Fm (R1F-A)	Colorless	Well to moderately rounded.	Small ($\leq 100 \mu\text{m}$); Most 25-30 μm	Cracks common. Core/rim zones present, but rare. Abundance of HREE contaminants.
USCL Usclas Fm (R1B-C)	Colorless	Moderately to poorly rounded. Some euhedral.	Small ($\leq 100 \mu\text{m}$), but variable. Most 50-60 μm	Many have cracks and inclusions. Concentric zoning or core/rim zones are apparent in ~10% grains.
HOU Houillière Fm (H5B2-A)	Colorless	Well to moderately rounded.	Small ($\leq 100 \mu\text{m}$); Most $\leq 25 \mu\text{m}$	Concentric zoning apparent in some. Grains are broken and cracked. ~30% grains have core/rims.
XDM Croix de Mounis (H5B1-A)	Colorless	Well to moderately rounded. Rare, euhedral grains.	Small ($\leq 100 \mu\text{m}$); Most 25-50 μm	Concentric zoning apparent in euhedral grains. Cracks and inclusions common. ~10% grains have core/rims.

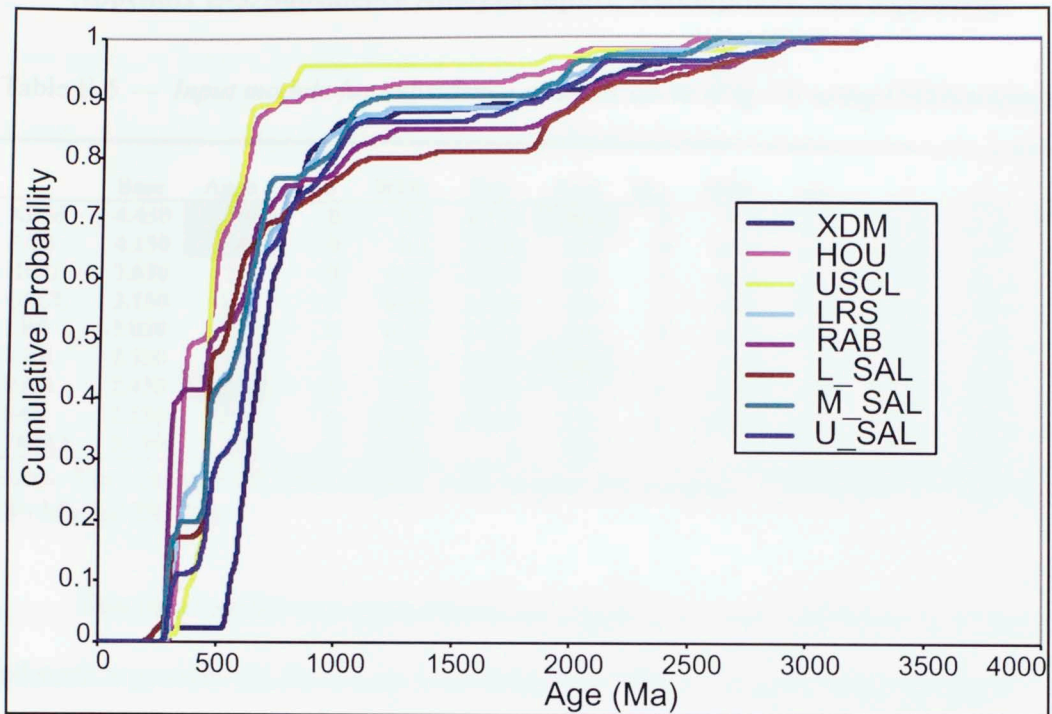
Zircon morphologies as a function of age, determined from CL images. *Note: no significant correlation.

Young < 330 Ma	Colorless	10% are moderately rounded	Small	Concentric zoning apparent in majority. Do not have metamorphic rims.
Old > 1000 Ma	Colorless	Moderately rounded	Small	Concentric zoning and cracks common. Some grains have core/rims.

Notes: No significant correlation of zircon morphologies as a function of age.



Appendix E-3. Kernel Density Estimate (KDE) plots for each detrital zircon sample (Vermeesch (2012)). Age distributions are plotted similar to PDPs but with increased uncertainty on each age.



Appendix E-4. Cumulative age probability plots show the summed probability of finding zircons of a specific age in a given sample, and are plotted with increasing age. These plots allow qualitative observation of general similarities and differences in a set of age distributions (Gehrels, 2008).

Appendix E-5. Subsidence Analysis Inputs, Assumptions, and Equations

Table E-5.— *Input module for subsidence analysis curve (Fig. 13) using OSXBackStrip.*

	Base	Ageb	SLb	WDb	Top	Aget	SLt	WDt	ρc	c	Ω_o	T
XDM	4.430	300	0	0.2	4.130	300	0	0.1	2.61	0.168	27.5	1
PAB	4.130	300	0	0.1	3.630	295	0	0.09	2.65	0.329	37.0	1
HOU	3.630	295	0	0.09	3.130	295	0	0.08	2.67	0.441	42.4	1
USCL	3.130	295	0	0.08	3.030	289	0	0.07	2.66	0.392	38.1	1
LRS	3.030	289	0	0.07	2.730	288	0	0.06	2.69	0.458	47.4	1
VLA	2.730	288	0	0.06	2.430	286	0	0.04	2.7	0.520	51.0	1
RAB	2.430	286	0	0.04	2.130	279	0	0.009	2.67	0.462	39.0	1
SAL	2.130	279	0	0.009	0.130	258	0	0.006	2.71	0.641	50.0	1
TRIAS	0.130	258	0	0.006	0	252	0	0	2.66	0.431	37.2	1

Notes: For younger rift basin model, cells in gray are swapped: 300 Ma for 295 Ma, and 286 Ma for 281 Ma.

This input model uses grain density (ρc ; kg/m^3), porosity coefficient (c ; $1/\text{km}$), and surface porosity (Ω_o %) values from Hegarty (1988) to calculate modified, more accurate values for each stratigraphic unit based on relative percentages of shale, silt, sand, and conglomerate. Depths to formation (Top, Base), sea level (SLb, SLt), and water levels at deposition (WDb, WDt) are in km. All units are continental deposits, so sea level of 0 is entered. Water depths at time of deposition for the paleolake were taken from Pochat and Van Den Driessche (2011). Basin type (T) is continental (value of 1). Age control is the most likely source of inaccuracy owing to a lack of fossils (for relative dating at consistent increments) in the entirely continental Permo-Carboniferous section. Ages (Ageb, Aget) are from Bruguier et al. (2003), Schneider et al. (2006), Poilvet et al. (2011), and Pitra et al. (2012) (Table below). Light gray cells (Table E-5, above) highlight inputs that are changed to calculate youngest possible subsidence (Poilvet et al., 2011; Pitra et al., 2012). Significant hiatuses in sedimentation are also a common cause error in backstripping analysis (Xie and Heller, 2009). There are no confirmed unconformities in this section, but erosional contacts occur that represent

gaps and are included in upper bounding units (because OSXBackStrip does not run with unconformities), so age divisions between some stratigraphic units were extrapolated. See Figure 13 for resulting tectonic subsidence curves.

SOURCE	bXDM	tXDM	tHOU	bUSCL	tUSCL	bVL	bRAB	bSAL
Bruguier 2003		300	295±5					
Schneider 2006	300	297.5	295	291	289	288	281	279
Poilvet 2011	294±1**							
Pitra 2012	295±5*							

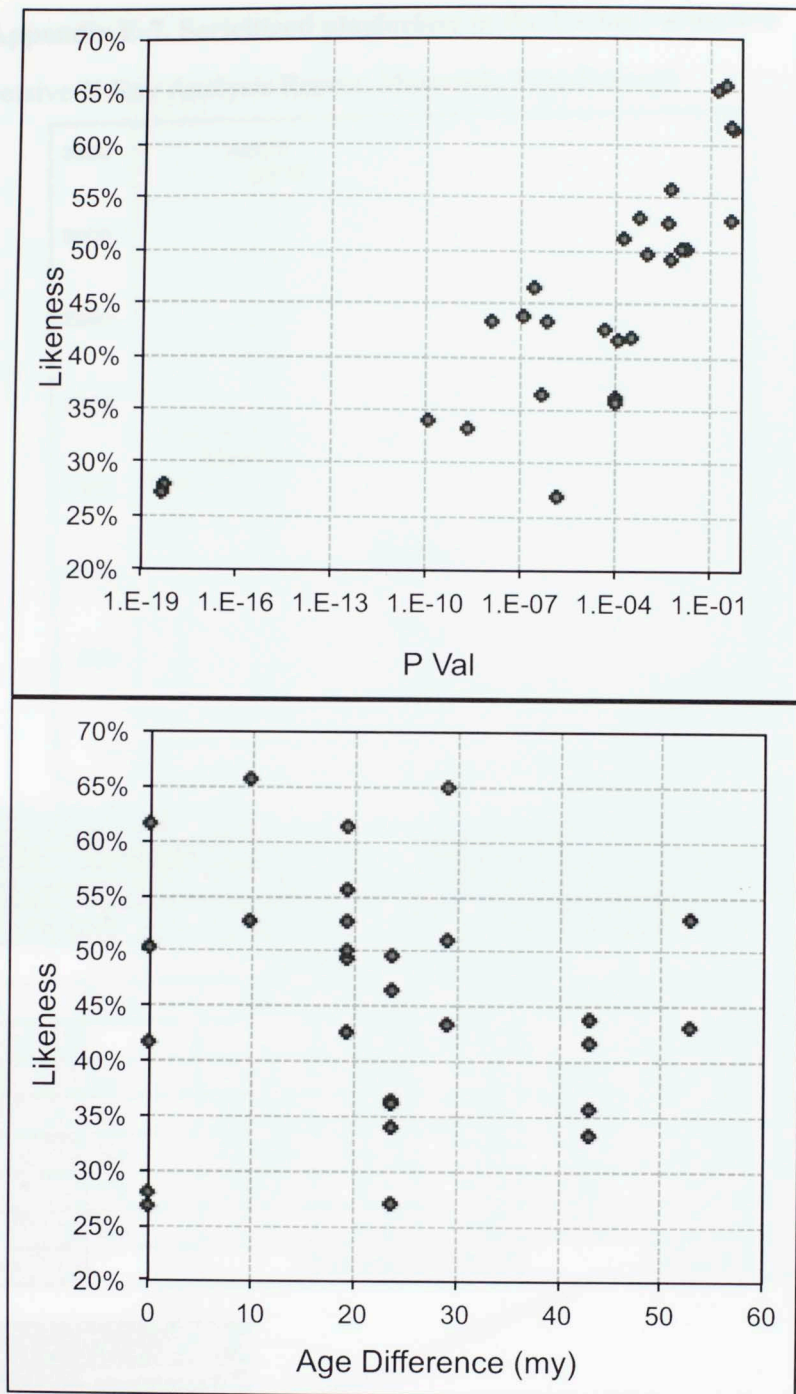
Notes: Gray: U-Pb zircon age from bentonite layer. *U-Pb monazite shearing along Espinouse Detachment. ** $^{206}\text{Pb}/^{238}\text{U}$ zircon emplacement age of Montalet granite.

OSXBackstrip v. 3.2 (Cardozo, 2013) uses 1D Airy Backstripping that involves exponential reduction of sediment porosity with depth, and assumes that water and sediment loads are subject to the strength of the underlying mantle. While this is usually true, sediment loads are not always evenly supported by the underlying mantle in any given location, sediment porosity does not always decrease with depth exponentially, and there are anomalies to assumptions about sediment or water loading and the nature of lithology-dependent compaction during burial (Cardozo, 2013). The model assumes no removed overburden since the Permian, but there was once approximately ~1.5-2.5 km of Mesozoic sediments (pers. commun. Van Den Driessche, 2014).

The backstripping procedure decompacts each time unit with the appropriate porosity values to reach a total decompacted thickness, or total subsidence, and then the total amount of sediment and water isostatic compensation is subtracted from the total subsidence to generate the tectonic subsidence curve. Water density (1000 kg/m^3) and mantle density (3300 kg/m^3) remain constant. The formulas and algorithms used in this

process in the OSXBackStrip program are from Allen and Allen (1990) and Watts (2001):

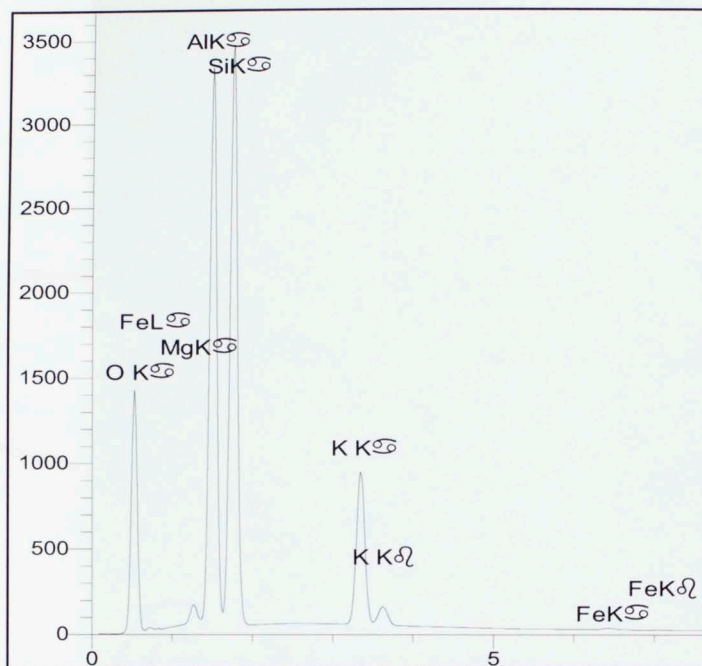
1. Exponential decrease of porosity with depth: $\Phi = \Phi_0 e^{-cy}$ Where c is the porosity coefficient Φ_0 is surface porosity, and Φ is the porosity at depth y .
2. General decompaction equation: $y'_2 - y'_1 = y_2 - y_1 - (\Phi_0/c) \{ \exp(-cy_1) - \exp(-cy_2) \} + (\Phi_0/c) \{ \exp(-cy'_1) - \exp(-cy'_2) \}$ Where y'_1 and y'_2 are the base and top of a stratigraphic unit before compaction, and y_1 and y_2 are the present base and top of the unit after compaction.
3. Sediment loading correction for continental basin: $Y = S \{ (\rho_m - \rho_s) / (\rho_m) \}$ Where Y is the depth to the basement corrected for sediment load, S is the total thickness of the column corrected for compaction, and ρ_m , ρ_s , and ρ_w are mantle, mean sediment column and water densities, respectively.
4. Water loading correction for continental basin: $Y_t = Y - \Delta_{SL}$ Where Δ_{SL} is the paleoelevation of the top of the basin with respect to the present sea level.



Appendix E-6. Likeness metric output plots (Satoski et al., 2014). See Table 3 for summary of Likeness (%) results from statistical comparison of age distributions from all detrital zircon samples. *Top:* K-S test (P-values) vs. Likeness (%). Note the positive correlation between Likeness and K-S test results. *Bottom:* Likeness as a function of geologic age. Note the lack of relationship; likeness is not a function of age.

Appendix E-7. Sericitized plagioclase in the Usclas Formation

Energy Dispersive X-Ray Analysis Report: Muscovite Pseudomorph



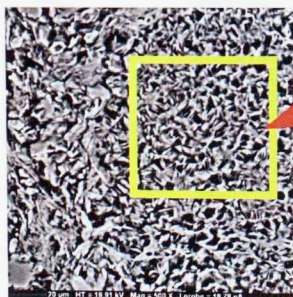
Acquisition Parameters

Analysis

Accelerating voltage (kV)	19.9	Correction Method	PAP
Beam current (nA)	19.780	Analysis Type	StdLess
Magnification	1000	Number of Oxygens	11

Measures & Results

Elt	Line	Int	W%	A%	Formula	Ox%	Cat#
O			47.09	61.64		0.00	0.00
Mg	Ka	38.1	0.82	0.71	MgO	1.36	0.13
Al	Ka	1142.7	20.02	15.54	Al ₂ O ₃	37.82	2.77
Si	Ka	1186.0	23.71	17.68	SiO ₂	50.73	3.16
K	Ka	366.1	8.11	4.34	K ₂ O	9.77	0.78
Fe	Ka	5.1	0.25	0.09	FeO	0.32	0.02
			100.00	100.00		100.00	6.85

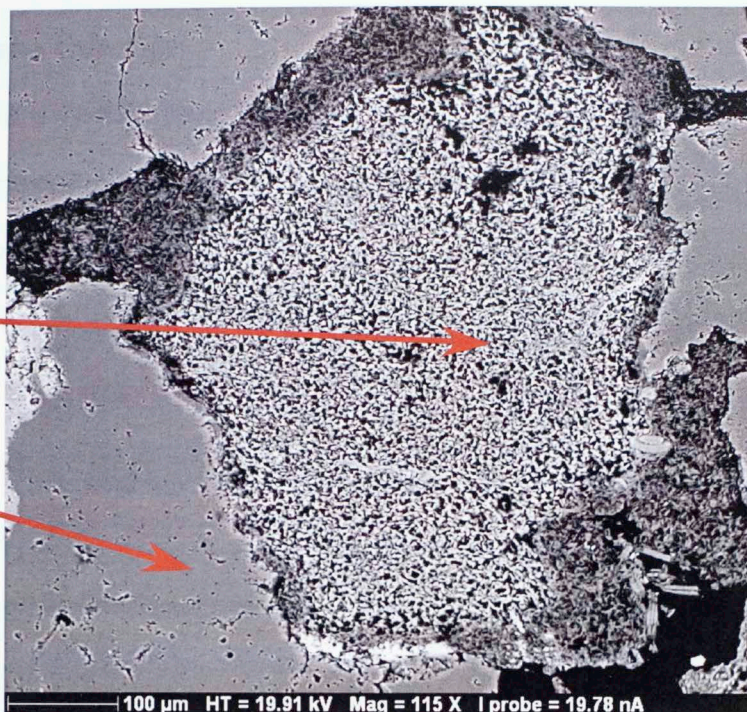


158 x 158 μm BSE Image (more on next page).

Appendix E-7. BSE Images from the Electron Microprobe

Muscovite

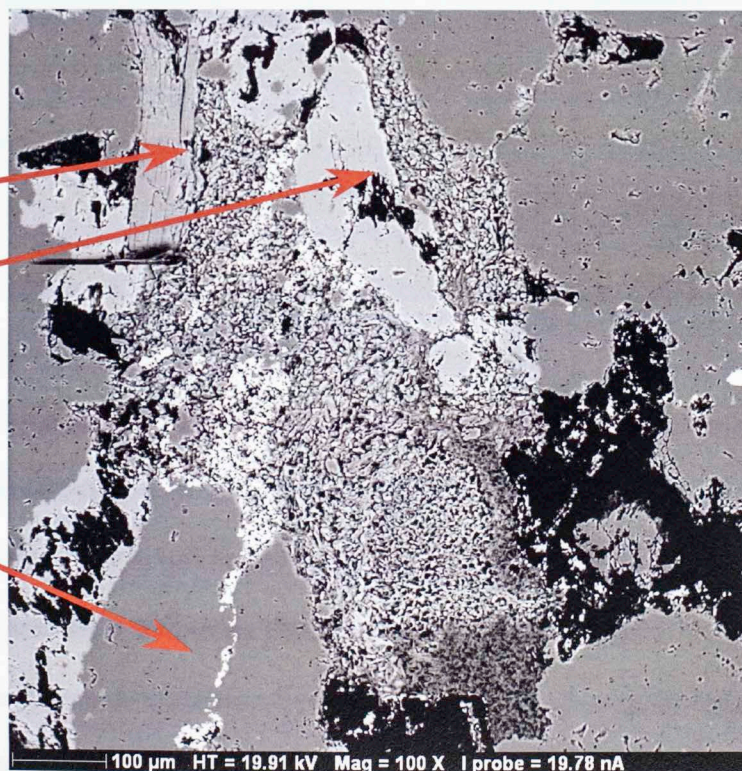
Quartz



Muscovite

Potassium
Feldspar

Quartz



Appendix E-8. Rationales for Methods Employed

Detrital zircon U-Pb geochronology

Zircon (ZrSiO_4) is used for geochronological analysis because of its near-universal presence in crustal rocks, negligible concentration of lead, and resistance to alteration of the U-Th-Pb isotopic system through chemical weathering, metamorphism, and diagenesis (Gehrels et al., 2008). Weathered and transported zircon minerals are present in most sedimentary rocks, and are therefore a useful tool in provenance studies, representing the ages of crystalline basement from which they were derived.

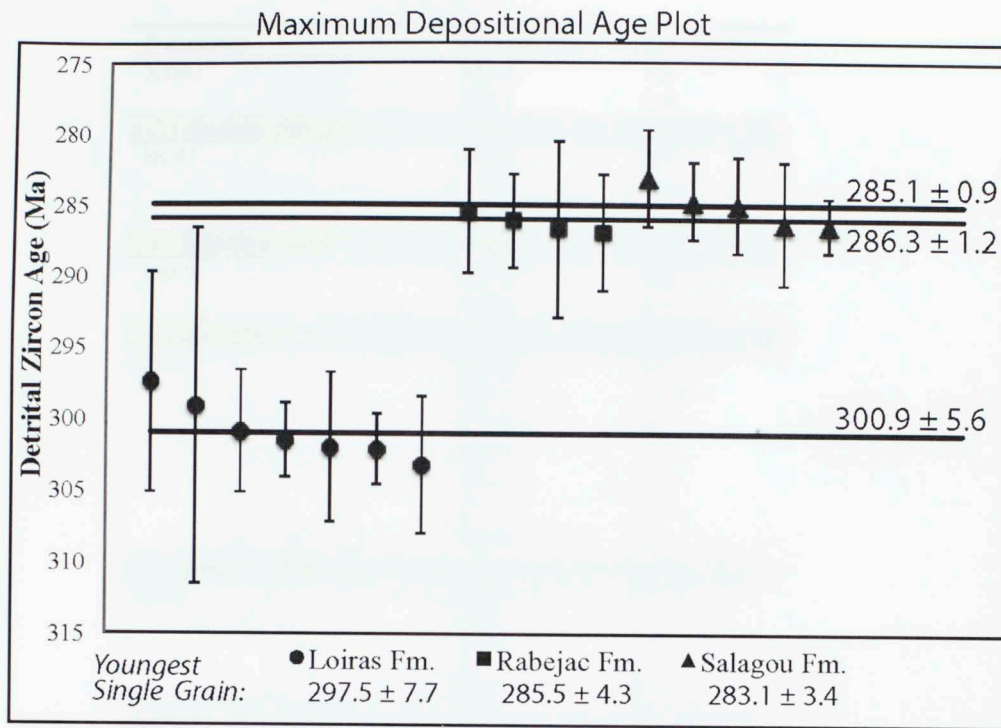
Sandstone petrography

Framework mineralogy of unaltered sandstone yields unique information about detrital modes, and thus provenance, that cannot be gained with other techniques. Modal compositions also shed light on tectonic settings (Ingersoll et al., 1984).

Subsidence analysis

Backstripping enables assessment of basin subsidence patterns and clarifies information about the tectonic setting and evolution of the basin (Xie and Heller, 2009). Sediments in rift basins contain a complete record of depositional environments, structural and thermal histories, and subsidence of developing basins, and thus are a crucial tool in the creation and evaluation of any given basin evolution model (Hegarty et al., 1988). Backstripping analysis (Allen and Allen, 1990; Watts, 2001) isolates tectonic subsidence by iteratively removing the isostatic load of sediment and water overlying each stratigraphic layer. Resulting plots are “graphic representations of the vertical movement of stratigraphic horizons, showing local subsidence or uplift since the horizon was deposited” (Van Hinte, 1978).

Appendix E-9. Maximum depositional age calculations



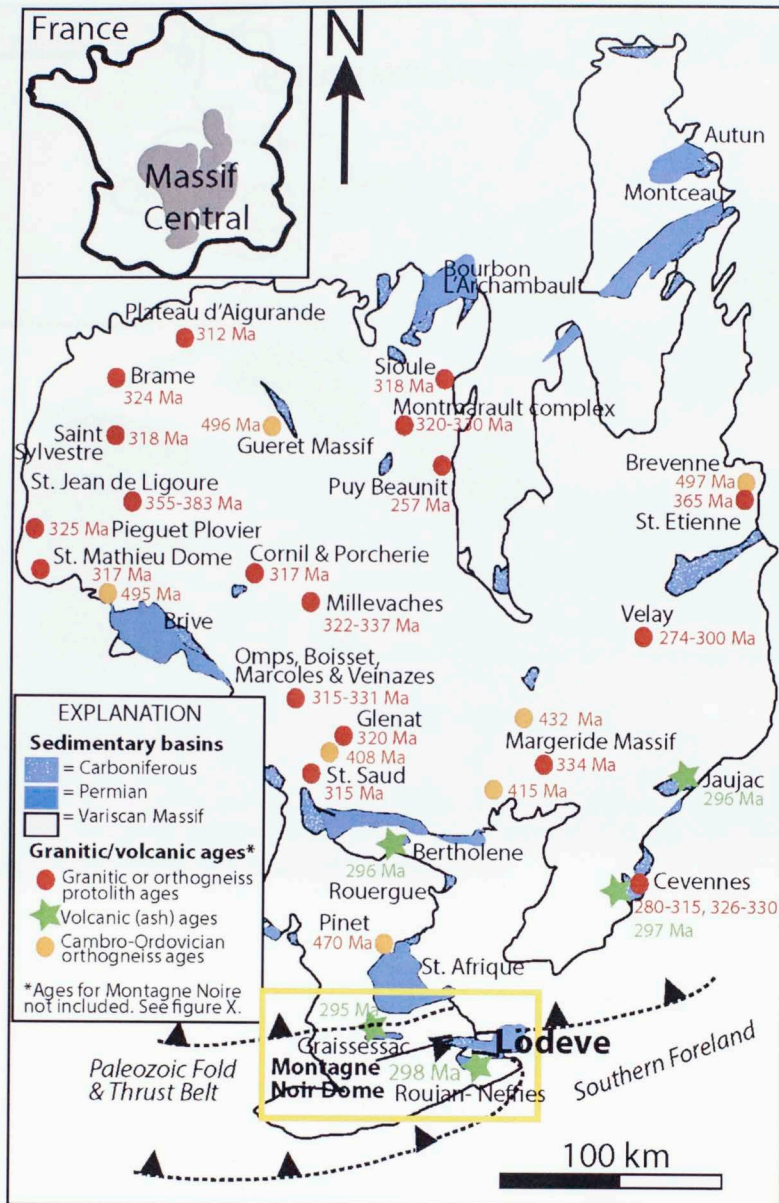
Appendix E-9. Maximum depositional age plot for youngest age populations in the Loiras, Rabejac, and Salagou formations (Upper Permian strata in the Lodève Basin). Trend lines show average, maximum depositional age with standard error. Individual ages and calculation methods are reported on the following page.

Appendix E-9. Maximum depositional age calculations

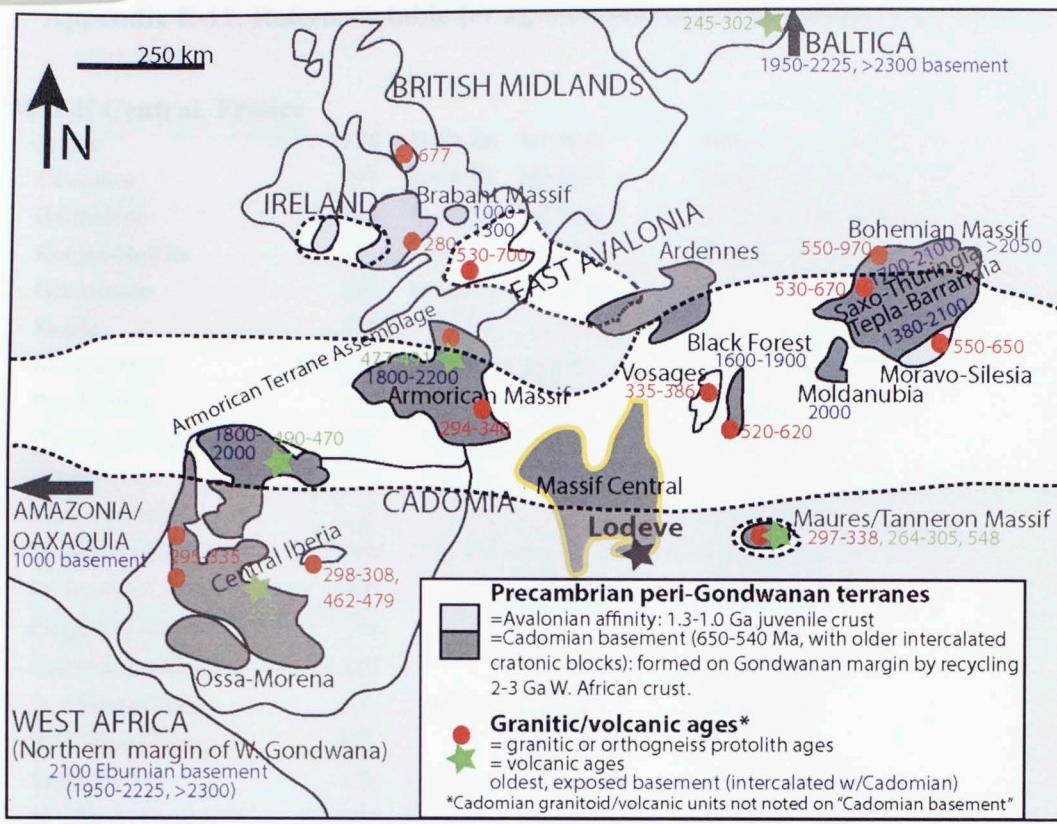
Table E-9.— *Detrital zircon ages used to calculate maximum depositional ages.*

Formation	Zr Age (Ma)	Std. Error
XDM	306.4	7.1
	309.1	4.4
	<i>Average (n=2)</i>	<i>307.8</i>
HOU	306.8	4.7
	308.1	5.5
	312.8	4.5
<i>Average (n=3)</i>	<i>309.2</i>	<i>0.5</i>
USCL	281.3	9.2
	336.6	4.5
	<i>Average (n=2)</i>	<i>309.0</i>
LRS	297.5	7.7
	299.1	12.4
	300.9	4.3
	301.5	2.6
	302.0	5.2
	302.1	2.5
	303.2	4.8
<i>Average (n=7)</i>	<i>300.9</i>	<i>5.6</i>
RAB	285.5	4.3
	286.5	3.3
	286.7	6.2
	286.9	4.1
<i>Average (n=4)</i>	<i>286.3</i>	<i>1.2</i>
SAL	283.1	3.4
	284.7	2.7
	285.0	3.4
	286.3	4.3
	286.4	1.9
<i>Average (n=5)</i>	<i>285.1</i>	<i>0.9</i>

Notes: Maximum depositional age calculations. The mean age of the youngest cluster ($n \geq 3$) of grain ages that overlap within 2σ uncertainty (*gray*) provides the most conservative measure of youngest age, but often results in depositional ages >10 Ma older than actual depositional age (Dickinson and Gehrels, 2009). According to Dickinson and Gehrels (2009), the youngest individual grain age in a zircon sample (**bold**) is the most representative of depositional age (within ± 5 Ma of the actual depositional age; 1σ uncertainty). Both youngest age measures were applied to best evaluate the youngest detrital zircon age population in our samples. Youngest Permian formations (Loiras, Rabejac, Salagou) are plotted in Appendix E-9 (previous page) to show the maximum (Permian) age of deposition in the Lodève-Graissessac Basin.



Appendix E-10. Supplementary provenance map: Original version of Fig. 17. Modified from Ledru et al. (1989) Femenias et al. (2003) and Bruguier et al. (2003), and ages are from Faure et al. (2010) and Melleton et al. (2010).



Appendix E-10. Supplementary provenance map: Original version of Fig. 18 showing individual ages from numerous sources (App. E-11).

Appendix E-11. Reference table for ages on source terrane maps (Fig 16-17).

Massif Central, France

Jaujac	296	U-Pb Zr	ash beds	Bruguier et al., 2003
Cevennes	297	U-Pb Zr	ash beds	Bruguier et al., 2003
Bertholene	296	U-Pb Zr	ash beds	Bruguier et al., 2003
Roujan-Neffies	298	U-Pb Zr	ash beds	Bruguier et al., 2003
Graissessac	295	U-Pb Zr	ash beds	Bruguier et al., 2003
Sioule	318	Ar/Ar	gneiss	Faure et al., 2010
Montmarault	330-320	U-Pb Zr	granite	Faure, 1995
Puy Beaunit	257	U-Pb Zr	mafic	Femenias et al., 2003
Plateau d'Aigurande	312	Rb/Sr	granites	Faure, 1995
Brame	324	U-Pb Zr	granite	Faure, 1995
Saint Sylvestre	318	N/A	plutons	Faure, 1995
St. Jean de Ligoure	355	U-Pb Zr	diorite	BRGM, 2007
St. Jean de Ligoure	383		migmatite	BRGM, 2007
Pieguet Plovier	325		granodiorite	Faure, 1995
Cornil & Porcherie	317		granitoid	Faure, 1995
St. Mathieu Dome	317	Rb/Sr	granite	Faure, 1995
St. Mathieu Dome	495		orthogneiss	
Tulle (LGU)	470	U-Pb Zr	orthogneiss	Melleton, 2010
Moulin du Chambon	529	U-Pb Zr	orthogneiss	Melleton, 2010
Millevaches	337-322	U-Pb Zr	granite	Faure et al., 2010
Millevaches	408	U-Pb Zr	orthogneiss	BRGM, 2007
Glenat	320	UTh-Pb	granite	Aurore et al., 2009
Omps	331	UTh-Pb	granite	Aurore et al., 2009
Boisset	318	UTh-Pb	granite	Aurore et al., 2009
Marcoles	315	Rb/Sr	granite	Faure, 1995
Veinazes	320	Rb/Sr	granite	Faure, 1995
St. Saud	315	Rb/Sr	granodiorite	Faure, 1995
Orthogneiss	408	U-Pb Zr	orthogneiss	Melleton, 2010
Pinet	469	U-Pb Zr	orthogneiss	Melleton, 2010
Margeride Massif	320-315	U-Pb Zr	granite	BRGM, 2007
Margeride Massif	334	Rb/Sr	granitoids	Faure et al., 2010
Margeride Massif	415		UGU	BRGM, 2007
Rocles	320	U-Pb Zr	granite	BRGM, 2007
N. Cevennes	330-326	U-Pb Zr	granite	Faure et al., 2010
N. Cevennes	315-280	Rb/Sr	gneiss	Faure et al., 2010
Velay	335-315		granite	Ledru et al., 1994
Velay	274-295	Rb/Sr	granitoid	Faure et al., 2010
Velay	300 Ma	U-Pb Zr	migmatite	Faure et al., 2010
Brevenne	365	U-Pb Zr	ophiolite	BRGM, 2007

Brevenne	497	U-Pb Zr	orthogneiss	BRGM, 2007
Morvan-Lyon	330		volcanic	BRGM, 2007

Montagne Noire Gneiss Dome

Sidobre	300	U-Pb Zr	granite	BRGM, 2007
Les Martys	320	U-Pb Zr	granite	BRGM, 2007
Le Lampy	320	U-Pb Zr	granite	BRGM, 2007
Le Salvetat	300-306	UPb Mz	migmatite	Poujol et al., review
Laouzas	319	U-Pb Zr	granite	Poujol et al., review
Folat	300	N/A	granite	BRGM, 2007
Georges d'Heric	451	U-Pb Zr	orthogneiss	Roger et al., 2004
Pont du Larn	456	U-Pb Zr	orthogneiss	Roger et al., 2004
Sommail	471	U-Pb Zr	orthogneiss	Cocherie et al., 2005
St. Eutrope	455 ± 2	U-Pb Zr	orthogneiss	Pitra et al., 2012
Schistes X	550-545	U-Pb Zr	Series tuffs	Lescuyer Cocherie 1992
Axial Zone	316 Ma	Rb/Sr	gneiss	Faure et al., 2010
Axial Zone	450-471 Ma	U-Pb Zr	granite	Faure et al., 2010
Montagne Noire	455-294	U-Pb Zr	gneiss	Pitra et al., 2012
Montagne Noire	316 Ma	Ar/Ar	orthogneiss	Faure, 1995
Espinouse Det.	297	Ar/Ar-	orthogneiss	Maluski et al., 1991
Vialais	320 Ma	U-Pb Zr	granite	Faure et al., 2010
Vialais	327 Ma	U-Pb Zr	granite	Matte et al., 1998
Soulie	318 Ma	U-Pb Zr	granite	Faure et al., 2010
Angles	325 Ma	U-Pb Zr	granite	Faure et al., 2010
Montalet	294	U-Pb Zr	leucogranite	Poilvet et al., 2011
Montalet	326-333 Ma	U-Pb Zr	granite	Faure et al., 2010

Appendix E-12. Unabridged Tectonic Background of the French Massif Central

Tectonic Units of the French Massif Central

The structure of the Massif Central consists of imbricated nappes (Burg and Matte, 1978; Ledru et al. 1994), with several generations of migmatite, granitoids, and orthogneiss that record a complex and long-lived history of metamorphism, deformation, and magmatism associated with the termination of Cadomian (Pan African) tectonics, and the Devonian through Permian evolution of the Variscan belt (Fig. 17): (1) The Southern Paleozoic fold and thrust belt, a continental margin platform series recording Early Cambrian-Devonian sedimentation, (2) a para-autochthonous Neoproterozoic-Ordovician micaschist with quartzite and volcanic units, that overthrusts unit 1, (3) the Lower Gneiss Unit (LGU), is analogous to unit 2 but also includes widespread Ordovician alkaline granitoids (now orthogneiss), and (4) the Upper Gneiss Unit (UGU) which includes mafic and felsic sediments and granitoids (480 Ma) that experienced high-pressure metamorphism ca. 380-360 Ma (Pin and Lancelot, 1982), as well as several migmatite, metagabbro, and ultramafic rocks. (5) Cambrian metagreywacke, rhyolite, and quartzite units are intruded by Ordovician granite form a separate tectonic unit (near Limousin) that experienced low-pressure metamorphism, and (6) the Brevenne unit (near Lyon) consists of mafic-ultramafic pillow basalt, gabbro, pyroclastics and ca. 366 Ma volcanic rocks. These units are referenced (by number) in the following discussion.

Deformation and Magmatism in the French Massif Central

Two separate hypotheses have been proposed to explain the geodynamic evolution of Western Europe. The first involves long-lived convergence of Gondwana

and Laurasia from the Silurian through the Early Carboniferous (Matte, 1986; Lardeaux et al., 2001), while others (Pin, 1990; Faure et al., 1997) emphasize a poly-phase tectonic evolution involving (1) Cambrian-Early Devonian opening and closing of ocean basins, and Armorican Massif accretion onto Gondwana, and (2) Middle Devonian-Carboniferous closure of the Rheic Ocean, followed by convergence of Gondwana and Laurasia. Both reconstructions include the stages discussed in the following section.

1. In the Late Neoproterozoic (600-542), the Massif Central belongs to northern Gondwana, an active margin defined by continental arc magmatism, and volcano-detrital deposits in the back arc basin (Cocherie, 2005). This evolved to a passive margin in the latest Neoproterozoic (BRGM, 2007).
2. Early Cambrian, post-Cadomian (pan-African tectonics) extension along the northern Gondwanan margin caused rifting, magmatism, and volcanism in the Massif Central through the Early Ordovician (units 2 and 3; Soula et al., 2001; Reille, 1978; Bard, 1978; Roger et al., 2004; Pin and Marini, 1993). The generation of 480-460 Ma granitoids is documented throughout the Massif Central (Diez Fernandez et al., 2012; Arenas et al., 2014) and characterizes the granitic protolith ages of ubiquitous orthogneiss units (Pin and Lancelot, 1982; Roger et al., 2004; Cocherie, 2005; Pitra et al., 2012). This plutonism has been compared to Colorado Plateau volcanism, pervading thick continental crust distal from subduction margins (Cocherie, 2005). Poly-phase tectonic reconstructions include Early Ordovician continental drift of the Armorican microcontinent (including rifting from, and subsequent re-welding onto the northern Gondwanan margin) (Arenas, 2014; BRGM, 2007). The Massif Central sedimentary

record reflects continental deposition in the Cambro-Ordovician, followed by carbonate platform deposition in the Devonian (unit 1).

3. In the Late Silurian-Middle Devonian, northward subduction of the Gondwanan margin led to a significant deformation event 395-385 Ma (Floc'h, 1983; Quenardel and Rolin, 1984; Costa, 1992; Duthou et al., 1994; Roig and Faure, 2000; Arenas, 2014).

The upper gneiss unit (unit 4, in NE Massif Central) contains several Cambro-Ordovician migmatite (partially melted quartzo-feldspathic) rocks that record high pressure, intermediate temperature metamorphism during subduction (Lardeaux et al., 2001). Middle Devonian calc-alkaline volcanic rocks and accreted ophiolites in the NE Massif Central (e.g. unit 6), and granodiorite plutons (NW Massif Central, Limousin) suggest evidence for subduction (deepest in NW Massif Central), associated with a Middle Devonian magmatic arc-back-arc complex during the opening of the Rheic Ocean (Pin and Paquette, 1998; Roger et al., 2004; Didier and Lameyre, 1971; Pin et al., 1982). Ophiolites are composed of oceanic crust that was originally generated during Early Ordovician separation of Armorica from northern Gondwana (Matte, 1991).

4. Closure of the Rheic Ocean ca. 380 Ma ultimately led to collision of Laurentia, Baltica and Avalonia, with Gondwana and the Armorican microcontinent (Arenas, 2014; Matte, 2001). Convergence related to this second collision extended through the Carboniferous, causing extensive intracontinental deformation in the Variscan Belt (Arenas, 2014). Several locations in the northern (units 4 and 6) and central Massif Central record widespread, intermediate temperature and pressure metamorphism 360-350 Ma. Shearing and recumbent folding in the southern Massif Central (Montagne

Noire) occurred 345-325 Ma (BRGM, 2007; Matte, 2001). Early Carboniferous magmatism and deformation is not well understood in a plate tectonic context, but may represent the early stages of orogenic collapse (Faure, 1995). It is associated with “syn-orogenic extensional tectonics” because it is unclear whether the regional tectonic setting is extensional or compressional; workers have interpreted structural evidence of compression during this time within the Montagne Noire and Ardennes, the southern and northern perimeters, respectively, of the Variscan belt (Ledru et al. 1989, 1994; Matte, 1986; Burg et al. 1987).

5. The Middle to Late Carboniferous (330-300 Ma) records the main period of plutonism in the Massif Central, largely constrained to the south. The tectonic stress regime (extensional vs. compressional) continues to be debated (see App. E-13 for discussion). Basin geometries that formed during this time are either half-grabens bounded by normal faults, or pull-apart basins along wrench faults (Arthaud and Matte, 1975; Blès et al., 1989; Becq-Giraudon and Van Den Driessche, 1990; Burg et al, 1990, 1994). In the southern Massif Central, plutonism and migmatization occurred 319-300 Ma in the Montagne Noire (Faure et al., 2010; Poilvet et al., 2011; Poujol et al., in review) and similarly, ca. 300 granite emplacement also occurs in the Velay Dome (Mougeot et al., 1997). Coupled with interbedded 298-295 Ma ash layers in Permian-Carboniferous sedimentary basins, the youngest Paleozoic magmatism recorded in the Massif Central (300-294 Ma) is interpreted to be related to post-orogenic, northeast-southwest crustal extension, and collapse of the entire Variscan belt (Ménard and Molnar, 1989; Burg et al., 1994).

Appendix E-13. Unabridged Tectonic Background of the Montagne Noire region

Geology of the Montagne Noire Dome

The NE-SW trending Montagne Noire (Fig. 16) is situated at the southernmost perimeter of the Variscan Belt in the Massif Central. Montagne Noire crust originally belonged to the Iberian-Catalan-Aquitaine block (Ebroia), before it was incorporated with the Iberian-Armorican arc (Matte, 1986) and was previously misinterpreted as granitic Precambrian basement (Demange, 1975). It is primarily composed of migmatized orthogneiss and micaschist, intruded by Late Variscan granodiorite, and is overlain Cambro-Ordovician schist and marble (Gèze, 1949; Bogdanoff et al., 1984). It is commonly divided into the Northern Side (lower Paleozoic metasedimentary units), ENE-WSW-trending Axial Zone dome, and Southern Side (Geze, 1949; Arthaud, 1970). Low-grade Paleozoic metasedimentary rocks on the Southern Side represent Cambrian-Middle Carboniferous deposition in the Variscan belt foreland basin (Engel et al., 1980), and exhibit km-scale recumbent folds (Southern Nappes), commonly interpreted to record compressional stresses associated with south-directed Variscan thrusting ca. 330-300 Ma (Arthaud, 1970; Burg and Matte, 1978; Matte, 1986; Burg et al., 1987).

The Axial Zone is composed of Ordovician migmatized granitic orthogneiss, surrounded by a biotite-granite-staurolite micaschist, "Schistes X" (Arthaud, 1970; Bogdanoff et al., 1984; Soula et al., 2001; Lescuyer and Cocherie, 1992). The upper Schistes X metasedimentary sections are dated around 545 Ma, from zircon in calc-alkaline metadacite-metarhyolite interbeds (Series tuffs). Post-Cadomian (560-500 Ma) Rb-Sr ages from orthogneiss and migmatite in the southern Massif Central (e.g. Gorges

d'Héric, Sommail, Nore, Plaisance, Le Salvetat, Mazamet, Mendic, Velay Dome) were originally interpreted as the crystallization ages of the granite protolith (Ducrot et al., 1979; Allegre et al., 1980; Faure et al., 2010). Rb-Sr ages are now out of date, as U-Pb zircon geochronology of the same orthogneiss units (e.g. Gorges d'Héric, St. Eutrope, Pinet) show an early Ordovician (ca. 480-450 Ma) age of granite emplacement (Roger et al., 2004; Pitra et al., 2012; Melleton et al., 2010), which corresponds to the timing of rifting of Armorica from Gondwana. These Ordovician granite intrusions (prevalent in the lower Montagne Noire metasedimentary series, "Schistes X") were subsequently deformed into orthogneiss during Variscan compression and deformation (Debat, 1974; Bard, 1978; Lescuyer and Cocherie, 1992; Cocherie et al., 2005). A second generation of granitic plutons intruded the Axial Dome between 319-294 Ma (Poilvet et al., 2011; Poujol et al., in review).

Migmatization of the Montagne Noire Dome

Migmatization of the dome occurred in two events: (A) 319 ± 2 Ma: first migmatization of the dome, and emplacement granite (La Salvetat-Laouzas) in the Axial Zone, and (B) a second crustal melting event 298-295 Ma, coeval with emplacement of the Montalet granite ca. 294 ± 3 Ma (Poilvet et al., 2011; Poujol et al., in review). Thus, two types of ca. 320 Ma migmatites exist in the Axial Zone (e.g. Le Salvetat/Laouzas), which are derived from early Paleozoic sediments, and granitic orthogneiss (mentioned above; Demange, 1975). One orthogneiss type is composed of 40% quartz, 40% plagioclase feldspar and 10% potassium feldspar, and the other 35% quartz, 25% plagioclase feldspar, and 28% potassium feldspar (Demange, 1975; Soula et al., 2001).

The tectonic interpretation of the Montagne Noire Gneiss Dome remains controversial (Van Den Driessche and Brun, 1992; Soula et al., 2001). Several ideas have been proposed, including: ductile wrenching and diapirism (Nicolas et al., 1977; Beaud, 1985), compressive anticlines (Arthaud, 1970; Demange, 1975; Mattauer et al., 1996; Matte et al., 1998), diapiric uplift and regional shortening (Faure and Cotterau, 1988), and metamorphic core complex (Van den Driessche and Brun, 1992; Echtler and Malavieille, 1990). Regional post-Variscan extensional tectonics, and local evidence of extensional strain, high-temperature, low-pressure metamorphism, and detachment zones in the eastern Montagne Noire during the Late Paleozoic favors the core complex model as proposed by Van den Driessche and Brun (1992). This involves isostatic uplift and deformation of the lower crust in an asymmetric extensional system that generated folding of the footwall (Southern Nappes), and basin development in the hangingwall (Lodève, Graissessac, St. Affrique, Fig. 19). Peak metamorphic conditions are assumed to be 700°C at 5 Kb in the gneissic core (Fig. 4; Soula et al., 2001; Demange 1985). The timing and nature of Montagne Noire exhumation is not known. The core was rising continuously ca. 340-316 Ma, during metamorphism and deformation (Soula et al., 2001; Costa and Maluski, 1988; Maluski et al., 1991; Matte et al., 1998). Muscovite-biotite $^{40}\text{Ar}/^{39}\text{Ar}$ ages document younger deformation 315-297 Ma, progressively younging from the axial core to the southern nappes (Maluski et al., 1991). These ages coincide with the ca. 300 Ma formation of the Lodève, Graissessac, and St. Affrique basins (Soula et al., 2001), and are interpreted to reflect the timing of a later thermal pulse (Maluski et al., 1991). With a thermal gradient of 40°C/km

(Thompson and Bard, 1982), Ar-Ar ages reflect a minimum depth of the core ≥ 17 km at 298 ± 2 Ma, during its most recent migmatization (Maluski et al., 1991; Pujol et al., in review).